THE UNIVERSITY *of* EDINBURGH

Development of an Automated Dual Piston Pressure Swing Adsorption System

Wenli Dang

For the Degree of Doctor of Philosophy

School of Engineering

University of Edinburgh

May 2014

Lay summary

The content of CO_2 in the atmosphere is increasing and this is assumed to be the major reason for global warming. Since fossil fuels will remain the main energy source for a number of decades, capture of CO_2 from flue gases will be necessary to reduce emissions. Pressure swing adsorption (PSA) is a main option as a separation process for carbon capture and storage. To be a competitive option fast cycles are needed in order to reduce the size of units. In this study, a Dual-Piston PSA system (DP-PSA) is developed, which is used to test the performance of adsorbents at fast cycles and to determine the CO_2 separation efficiency under process-like conditions.

The DP-PSA is a robust and flexible system that can test novel adsorbents rapidly under different experimental conditions. It is a closed system which requires only a small amount of gas and a few grams of the adsorbent. The whole system is controlled by a real time computer, which largely increases the accuracy of the control and the resulting data. The whole system is automated so that it can run a series of experiments without supervision and the user only needs to set the experimental conditions in a simple interface, in advance.

In this thesis, the system is validated by testing the well-known adsorbent zeolite 13X. The results agree well with literature values. In addition, the DP-PSA experiments also provided much useful information about adsorption kinetics.

Abstract

Thousands of different adsorbate materials are developed every day. However, current instruments are not able keep up with testing the materials and faster methods needed. This thesis described the development and automation of a, a novel DP-PSA (Dual Piston-Pressure Swing Adsorption) setup. It is a unique system suited to test novel materials for the efficient separation of binary mixtures in a single adsorption column. The DP-PSA is a closed system where pistons moving in cylinders at each end of the adsorbent column induce the cycling of fluid flows and pressure variations in the fixed bed. The equipment can be assimilated to a distillation column with total reflux and allows the measurement of the maximum separation achievable with the material. Pressure transducers to measure absolute pressure variations and pressure drops are placed at the top and at the bottom of the column, respectively. Four thermocouples inside the column are placed in two pairs at different positions along the column. In each pair one thermocouple is inserted into a zeolite pellet while the other is exposed to the gas phase. The apparatus is automated by LabVIEW code and controlled by a real time computer, Compact RIO. Thus, the automated DP-PSA is able to run a series of experiment without direct supervision.

The development of the DP-PSA includes experiment design, measurement of leak rates, dead volumes for packed and unpacked column, friction, pressure drop across the adsorbing column and temperature gradient along the column. The system with thermocouples can be run in two modes: single pellet experiments and full packed column runs. Single pellet experiments, where only the pellets connected to the thermocouples are inside the system, were carried out to study the heat transfer between the zeolite pellets and gases (He, N_2, CO_2, and mixtures of N_2 and CO_2). The other mode is that the adsorbing column is packed fully with zeolite pellets. Experiments with pure gases and mixtures of N_2 and CO_2 were run with different configurations of the system: cycle time; phase angle; stroke length ratio and initial temperature. The system was tested using commercial 13X pellets. The measured signals were compared based on the amplitude and time shifts and numerical simulations were used to compare the predictions of a dynamic model of the system with the experimental results. The DP-PSA has been shown to generate a very large set of experimental results, with varying conditions which

allows to determine physical parameters of dynamic models. This is achieved without consuming gases given that several experiments are automatically carried out in a closed system.

Acknowledgements

First and foremost, I would like to express my great gratitude to my advisor, Professor Stefano Brandani, for encouraging, inspiring and positively challenging me throughout the course of my PhD. It has been an honor to be his PhD student. His tenacity, enthusiasm and depth of knowledge have left a deep impression on me. This thesis would have been impossible without the support and mentoring of my advisor.

Secondly, I would like to give my thanks to the members of the carbon capture group in the University of Edinburgh. Especially, Dr Daniel Friedrich provided the model for this work and has always given me valuable suggestions. The isotherms were measured by Dr Enzo Mangano and Dr Xiayi Hu. I really appreciate their contributions. I am also thankful to the technicians from the University of Edinburgh, ABB and National Instrument. Their technical support and suggestions have been important to the progress of this study.

Financial support from the Engineering and Physical Sciences Research Council, grants EP/F034520/1 and EP/G062129/1, is gratefully acknowledged.

Lastly, but not least, I would like to thank my whole family, for their immeasurable help, support and belief.

Thesis declaration

I certify:

(a) that the thesis has been composed by me, and

(b) either that the work is my own, or, where I have been a member of a research group, that I have made a substantial contribution to the work, such contribution being clearly indicated, and

(c) that the work has not been submitted for any other degree or professional qualification except as specified.

Signature:	

Wenli Dang

Table of contents

List of figures

List of tables

1.Introduction

1.1 Greenhouse effect

Gases that trap heat in the atmosphere are called greenhouse gases. Solar radiation at the frequencies of visible light largely passes through the atmosphere to warm the planetary surface, which then emits this energy at the lower frequencies of infrared thermal radiation. Infrared radiation is absorbed by greenhouse gases, which in turn re-radiate much of the energy to the surface and lower atmosphere (Wikipedia 2014). It can be easily understood that a high amount of greenhouse gases would break the balance of incoming and outgoing energy of the earth (Jacobson 2001). In this way, greenhouse gases act as a blanket, making the earth warmer (Parmesan and Yohe, 2003). This phenomenon is well known as the "greenhouse effect" ("IPCC AR4 SYR appendix glossary" 2008a). It affects this planet in various areas directly and indirectly. Because of the temperature increase, ice and snow in high-altitude and high-latitude will melt which will result in a rise in sea level and much land being submerged. Ecosystems have to adapt to this climate change, such as creatures' growing season, leaf and bloom dates, wintering range, etc. Furthermore, several species are threatened with extinction (Harvell et al. 2002).

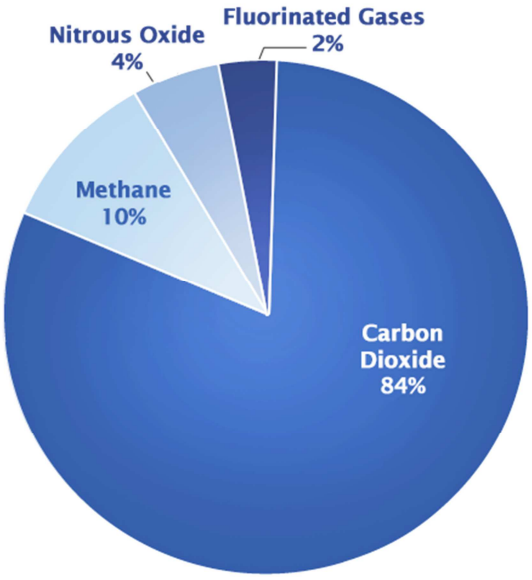

Figure 1.1 Greenhouse Gas Emissions in 2010 (NRC 2010)

According to the Inventory of U.S. Greenhouse Gas Emissions and Sinks of 2010 (Figure 1.1), CO_2 represents 84% of these emissions. The total emissions of greenhouse gases in 2010 is equivalent to 6822 million metric tons of CO_2. It enters the atmosphere through burning fossil fuels (coal, oil and natural gas), wood products, solid waste and chemical reactions (Zachos 2013). The emissions by human activities are responsible for the increase of CO_2 that has occurred in the atmosphere since the industrial revolution began around the year 1750 (NRC 2010). Various industrial processes accounted for about 14% of total U.S. CO_2 emissions and 20% of total U.S. greenhouse gas emissions in 2010 (Figure 1.2). Part of the CO_2 emitted from industry is due to fossil fuel combustion or chemical reactions while most of the rest is the result of electricity usage, which is primarily from the combustion of fossil fuels (NRC 2010). In December 1997, the Kyoto protocol has given a target to cut greenhouse gas emissions by 12.5% below 1990 levels by 2008-2012 (Chazournes 1998). The UK 2008 Climate Change Act requires to cut emissions of greenhouse gas emissions by 80% below 1990 levels by 2050 (2008b).

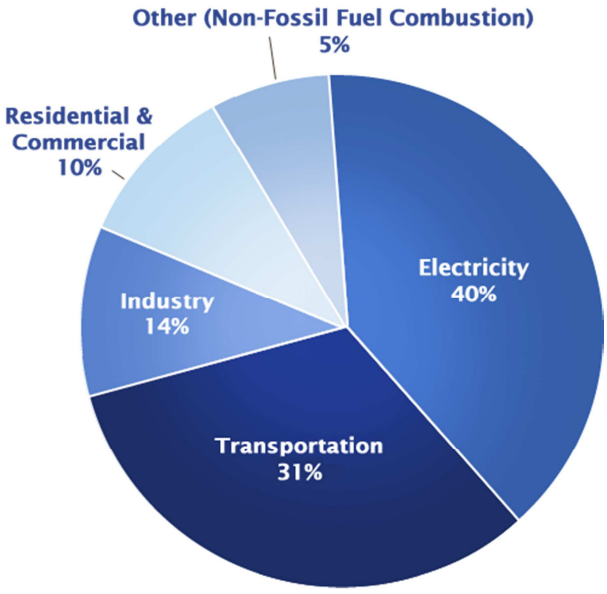

Figure 1.2 Carbon Dioxide Emission by source, U.S. ("Inventory of U.S. Greenhouse Gas Emissions and Sinks: 1990-2011" 2013)

As seen from Figure 1.2, the power and industrial sectors contribute so much to the greenhouse gas emission, thus, reducing CO_2 emission from these sectors could be effective to mitigate the greenhouse effect.

1.2 CO_2 capture and storage

There are several options to reduce CO_2 emissions, such as using renewable energy (Martinot 2011), increasing energy efficiency (Diesendorf 2007) and reducing energy consumption. However, in the near to mid term, the use of fossil fuels will remain prominent. Carbon dioxide Capture and Storage (CCS), from stationary sources (Wall 2007) is considered a reasonable way to reduce CO_2 emissions.

A carbon storage study in the UK ("Opportunities for CO_2 Storage around Scotland" 2009) shows that Scotland has an extremely large CO_2 storage resource. It is overwhelmingly in offshore saline aquifers, together with a few specific depleted hydrocarbon fields. Such storage resource can easily accommodate the industrial CO_2 emissions from Scotland for the next 200 years. It is likely to be sufficient to allow import of CO_2 from NE England, if so, it equates to over 25% of future UK large industry and power CO_2 output. That study also indicates many other storage resources. The storage capacity of offshore Norway is comparable with that of offshore Scotland. Other storage resources in the Netherlands, Denmark and Germany, also provide great capacity.

In the east of the world, CCS is particularly important for China. Although China is reducing its reliance on coal by expanding capacities in hydro, solar, wind and nuclear power, around 70% of its energy demand is still from coal. Even under the most aggressive policy scenario, coal demand can only be reduced to nearly half of China's energy consumption through 2030 and a significant portion for the foreseeable future. (Jiang et al., 2008) Fortunately, China is well-suited for widespread adoption of CCS. Firstly, lower fuel, material and labor costs than Western countries are beneficial. Moreover, China's geology and the location of large CO_2 point sources relative to potential geologic sinks mostly match well. In the report by Li and Wei, of the Chinese Institute of Rock and Soil Mechanics (IRSM) with the Pacific Northwest National Laboratory (PNNL), it is suggested that theoretically China has sufficient deep

saline formations to store up to 3066Gt CO_2, which is more than 450 times China's total CO_2 emissions in 2005. There are more than 1600 large point sources (each emitting more than 100,000t CO_2 per year) in China. More than half of these large point sources are located directly above a potential geologic sink and more than 80 percent are within 80 kilometers from such a site. (Dahowski et al. 2009)

In North America, based on the feasibility study of CO_2 storage by the U.S. Department of Energy, large storage capacity of CO_2 in exhausted oil fields and saline formations offers a great potential for CCS to achieve greenhouse gas emission reductions (The U.S. Department of Energy's National Energy Technology Laboratory 2008). It is proven that CCS applied to a modern conventional power plant could reduce CO_2 emissions to the atmosphere by approximately 80-90% compared to a plant without CCS (Metz et al., 2005). However, the CCS technology varies much on their cost and efficiency. Thus, there is a need of research for improved CCS processes.

Generally, there are three different of technologies for CCS from power plant: Pre-combustion, Post-combustion and oxy-fuel combustion.

1.2.1 Pre-combustion capture

Pre-combustion capture is a process of separating carbons in the fuel before the combustion (Linga et al., 2007). It is widely used in chemical, gaseous fuel and power production (U.S. department of Energy 2010). The fuel is first gasified with oxygen or steam to produce a synthesis gas composed principally of CO and hydrogen. This gas is then chemically converted into carbon dioxide and hydrogen in the so-called water gas shift reaction ($CO+H_2O \leftrightarrow CO_2+H_2$) (Kanniche et al. 2010). The CO_2 is then separated and the hydrogen is used as fuel or in a hydrogen fuel cell. This can reduce up to 95% of CO_2 emissions, however, it can only be applied to new fossil fuel power plants because the capture process requires high integration with the combustion, resulting in a chemical plant in front of the gas turbine, which in turn requires higher investment compared to a conventional plant. Other limitations, such as high NO_x emissions and low efficiency of H_2 burning, should also be considered (Starr 2009).

1.2.2 Oxy-fuel combustion capture

In the process of oxy-fuel combustion, the fuel is burned in pure oxygen, instead of air. The result of combustion is an almost pure carbon dioxide stream (typically 90%) that can be easily separated from steam by cooling and directly stored. Therefore, a power plant with this technology is referred to be "zero emission". Because it avoids the dilution of exhaust gases with nitrogen in air, it increases very significantly the partial pressure of CO_2 in the exhaust gases from combustion, thus, the CO_2 can be easily separated (Kanniche et al. 2010). Since the nitrogen component of air is not heated, fuel consumption is reduced, and higher flame temperatures are possible. However, an air separation unit is necessary to provide almost pure oxygen to the boiler. Thus, the high cost of energy needed to produce pure oxygen is a challenge (Sweet 2008).

1.2.3 Post-combustion capture

Post-combustion capture is the process of separating CO_2 from the flue gases after the combustion process. This technology can be applied to most existing fossil fuel burning power plants or factories. There are three typical technologies of interest in development.

- Absorption – It usually contains chemical absorption or physical absorption. In chemical absorption processes, reversible chemical reactions of CO_2 with aqueous solvents, typically amines, monoethanolamine (MEA)-based solvents, are used to remove CO_2. The process involves the passage of an aqueous amine solution down an absorption tower, while a gaseous stream of flue gas containing CO_2 is introduced at the bottom. A blower is required to pump the gas through the absorber (D'Alessandro et al. 2010). It can reduce the CO_2 concentration in the flue gas to 0.5%, however, the drawback of this process is its high energy cost for the solvent regeneration (Yeh et al., 2004). Besides, the fixed stoichiometry of the chemical reaction limits the flexibility compared to other separation processes. In comparison, in physical absorption it is easier to strip the solvent and absorbers also have wider options, such as tributylphosphate, polycarbonate, methylcyanoacetate and n-formyl morpholine (Newman 1985), but this is only effective in CO_2-rich gas streams (Keskes et al., 2009). Absorption using amines has some other

drawbacks such as high equipment corrosion rate, degradation and a large absorber volume required.

- Membrane separation – Based on the difference of permeabilities of gases through the membrane, gases including CO_2 can be separated on each side of the membrane. Membranes are also traditionally used to separate hydrogen gas from various other gases. Inorganic, metallic, polymeric and solid-liquid are all forms of membranes used today (Aaron and Tsouris, 2005). Membrane separations are classified by pore size and by the separation driving force which may depend on the pressure, partial pressure and electrical potential. Thus, the limitation is the high partial pressure of CO_2 required. Flue gas contaminants may lead to a deterioration of the membrane.

- Adsorption –High surface area solid materials that have significant adsorption capacity for CO_2 are attracting more and more attention (Yu 2012). The rate-limiting step for physical adsorption is the diffusion of CO_2 from flue gas to pores of a mesoporous adsorbent and this is about 3 orders of magnitude faster than the reaction rates in aqueous amines (Khatri et al. 2005). For CO_2-rich gas streams, adsorption processes usually contain frequent regeneration of the solid bed. To achieve repeated adsorption and desorption, pressure swing adsorption (PSA) or temperature swing adsorption (TSA) are widely applied. By changing the pressure or temperature large differences in the CO_2 capacities of the adsorbent lead to separation and regeneration.

1.3 Thesis objectives

In this study a novel apparatus which aims to test adsorbent materials in fast cycles (a few seconds) was developed. Fast cycles are essential in carbon capture applications due to the scale of the typical flow rates in a power plant. A 1 GW coal fired power plant emits approximately 900 tonnes of CO_2 in one hour (Lackner et al., 1997), therefore only PSA/VSA cycles of the order of few seconds can lead to system sizes that are competitive with other separation technologies. The current project addresses the need for an experiment capable of testing materials under variable pressure and temperature conditions with fast cyclic adsorption and desorption.

Two pistons are used to cycle the pressure on both sides of an adsorption column. This system allows to run experiments with many different configurations, i.e. cycling frequency, stroke length ratio, phase angle between pistons, temperature and pressure. It is a closed system so only small amounts of gas and adsorbent are needed to perform the full series of experiments. The system has been automated to run different experiments in a sequence without supervision. These features make it an efficient system with high reliability and flexibility. The pistons are controlled by a real time computer, which allows controlling the pistons accurately even in very fast speed, meanwhile, data is logged including absolute pressure, pressure drop across the column and solid and gas phase temperature at different positions in the column. Therefore, there are two main objectives of the thesis.

1. **Design of the dual piston Pressure Swing Adsorption system** (DP-PSA) **and automation of the experiments in LabVIEW:** The first task was to develop the DP-PSA system, including the automation. The devices involved in this equipment come from different companies, which will be detailed in Chapter 3. Their interface protocols are not uniform. Communications between them is the first step and their parameter setups are the second. Once each individual component works properly, the control of the pistons movement had to be designed. Then the system automation is carried out to enable running a series of experiment using a LabVIEW interface. A project of LabVIEW code is developed with sub code sorted in different categories. It includes the logics of the simultaneous operation of each device and the configuration of the real time computer and FPGA.

2. **Run experiments with the automated DP-PSA system for a test adsorbent and explore the characterisation of the experimental results:** Different experiments should be run to confirm the feasibility of the new system. They are aimed at the characterisation of the DP-PSA system and to show the capabilities for testing of adsorbents. The experimental results will be compared to simulation results. From the initial experiments performed using commercial pellets of zeolite 13X, it is clear that they provide fundamental information on the adsorption and separation properties of the material.

1.4 Thesis Overview

Chapter 2 - Adsorbents

This chapter introduces some background information on typical adsorbents, especially focusing on zeolite 13X which was used as the test adsorbent in this study. The structure and some properties of zeolites from literature are presented.

Chapter 3 - Theory of the pressure swing adsorption technique

This chapter includes a summary of the basic theory of PSA. In the history of PSA development, typical milestones were introduced, including its characteristics and applications.

Chapter 4 – Mathematical model of the DP-PSA

To predict the adsorption process over a wide range of experimental conditions, a simulation tool is needed. A suitable model for the simulation of the DP-PSA system is presented. The key parameters of the model are presented.

Chapter 5 - Semi-automated DP-PSA system

A complete description of the DP-PSA system is presented. The operation of a compression and expansion cycle is flexible since both pistons are independent so they can move with any stroke length and with arbitrary phase angle and speed. It offers great capability for the experiments but a challenge for piston control and data logging. Operation of the system to run experiments is described.

Chapter 6 – DP-PSA automation

The interfacing and automation of the rig, including the control hardware and software code program is described. A real time computer controls the movement of the pistons and acquisition of the information. FPGA is used to increase the efficiency of this computer's work. The configuration and the sequential control code are completed by LabVIEW and integrated into a whole project.

Chapter 7 – DP-PSA characterisation

Some preliminary experiments were run to characterise the system, including leak rates, dead volumes for packed and empty column, friction, pressure drop across the adsorbing column and temperature gradient along the column. These preliminary measurements are essential in the data analysis.

Chapter 8 - Zeolite 13X Packed Experiments by DP-PSA

It shows the experiment of fully packed column with zeolite 13X. Firstly, pure gas experiments were run. By changing the individual configuration of the system, the influence to the pressure and temperature are studied. Then, experiments with mixtures of N_2 and CO_2 were run to study the gas separation. With different configurations of the system, separation efficiency varies significantly.

Chapter 9 - Single Pellet Experiments by DP-PSA

This chapter studies heat and mass transfer by single pellet experiments. The column is not packed and only two pellets of zeolite 13X are inside the column. Experiments were run with different gases, different initial temperatures and different cycle times.

2. Adsorbents

2.1 Introduction

The starting point for any advancement in adsorption technology is the availability of an effective adsorbent material. Adsorbents usually operate via physical adsorption or chemical interactions. Strong interactions, characteristic of covalent bonding, lead to chemical adsorption; weak interactions, characteristic of weak van der Waals forces, lead to physical adsorption (Rouquerol et al.1999). Physical adsorption is favoured in PSA due to the ease of regeneration. Therefore, the central advantage of physical adsorption methods is the possibility of low energy requirement to regenerate the adsorbent material and the quick regeneration time associated with changing pressure. Since adsorption is a surface phenomenon, a successful adsorbent will have a high surface area to its bulk volume ratio. In addition, to assess an adsorbent's quality, numerous factors need to be considered, such as its adsorption and desorption kinetics, adsorbate capacity, regenerability and stability.In reality, all practical adsorbents have trade-offs. Their advantages and disadvantages should be considered in different priority depending on their real applications and on the process conditions.

Most adsorbents fall into four classes:

- Carbon-based compounds

  They are hydrophobic and non-polar. So it is not difficult to release the compounds of interest during the desorption process and allow a broader spectrum of components to be collected (Vergunst et al. 2001). Due to the limited number of strong adsorption sites, these materials are less suitable for post-combustion carbon capture and have not been used in this study.

- Polymer-based compounds

  These are porous polymer matrix materials which may have functional groups incorporated. They are classified as four types: polymeric porous adsorbents; their chemically modified derivatives, polymer-coated inorganic hybrid adsorbents, and polymeric chelating adsorbents (Pan et al. 2008). Several variants of Polymers of Intrinsic Microporosity have

been investigated as part of the IGSCC project at the University of Edinburgh and found to be suitable in carbon capture applications for either high pressure conditions or for membrane processes (Mangano et al. 2013).

- Metal Organic Framework Adsorbents (MOF)

  MOFs are a new class of adsorbent materials with strong potential for CO_2 adsorption. They generally consist of two building elements: inorganic coupling units and organic linkers. They are highly porous with large surface area (Choi et al., 2009) and can be functionalised. These materials have also been studied extensively in the IGSCC project (Mangano et al. 2013) and have shown a higher adsorption capacity than commercial zeolites. For the dual piston PSA unit gram quantities of pelletised adsorbents are required, therefore these materials were not suitable for the development and evaluation of this new technique.

- Zeolites

  The zeolites are crystalline aluminosilicates with an extensive three dimensional network of oxygen atoms. They are characterised by open crystal lattices containing pores with molecular dimensions which allow molecules to penetrate. Zeolites can be classified based on their morphological characteristics, crystal structure, chemical composition, effective pore diameter and natural occurrence (Barrer, 1982; Breck, 1974; Meier and Olson, 1987; Bragg, 1937). Separation of CO_2 by zeolites generally depends on their structure and composition of the framework, cationic form and zeolite purity (Harlick and Tezel, 2004; Hernandez-Huesca; Daz; Aguilar-Armenta, 1999). Zeolite 13X and Y show the best carbon capture performance amongst the commercially available materials (Xiao et al. 2008) and given the availability of large batches in our laboratory, 13X was selected as the adsorbent to be used in this study.

2.2 Zeolites

Zeolites are the most widely reported physical adsorbents for CO_2 capture in the patent and journal literature (Choi et al. 2009). The term zeolite was originally coined by a Swedish mineralologist, Axel Fredrik Cronstedt in the 18^{th} century (Gusenius 1969). Then they were used in many different fields. Major uses consist of petrochemical cracking, detergents,

ion-exchange (water softening and purification), and in separation processes for gases and solvents, due to their porous properties (Ackley 2003).

2.2.1 Framework Structure

Zeolites are molecular sieves that contain different percentages of alumina and silica, which result in different adsorption capabilities (Virta 1998). Based on molecular size, molecular sieves have a distinct property for selective separation of molecules, due to the unique and regular pore structure of each molecular sieve. The pore size and shape of the zeolite determines the maximum size of the molecule that can enter a pore. The size, distribution and charge density of the exchangeable cations (Na^+, Li^+, Ca^{2+}, K^+, NH_4^+) affects the adsorption properties of zeolites (Zhao et al. 1998). Orientation of the molecule in the pore cavity may affect the diffusion rate in the structure and the selectivity of a zeolite, as well.

Like most silicates - zeolites are based on TO_4 tetrahedra, where T is an aluminium or silicon atom (phosphorus in aluminophosphates). The basic structure of zeolites is made up of 4-connected networks of atoms. Atom T is in the middle and oxygen atoms are at the corners of the tetrahedra. In the top left of Figure 2.1, atom T is represented as a silica atom. Large numbers of such tetrahedra can link together to form a cage structure.

The tetrahedral units are connected in order to build the cage structure in Figure 2.1. The finite tetrahedral units form the basic building blocks which are shown in Figure 2.2. The T atom of the tetrahedron is located at each of the corners, represented as the black point. All oxygen atoms are not shown in the figure but located towards the middle of the lines joining T atoms. When considering zeolite structures, the primary building unit is the TO_4 tetrahedra, and the units listed in Figure 2.2 are called the secondary building units (SBUs).

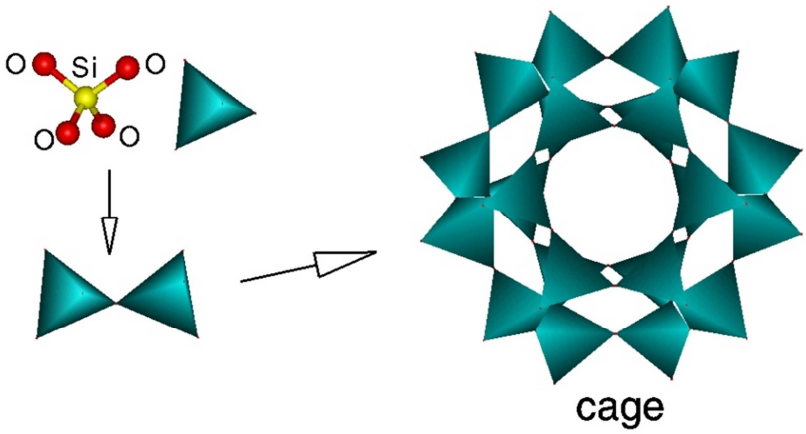

Figure 2.1 Framework structure of zeolite (Bell 2001)

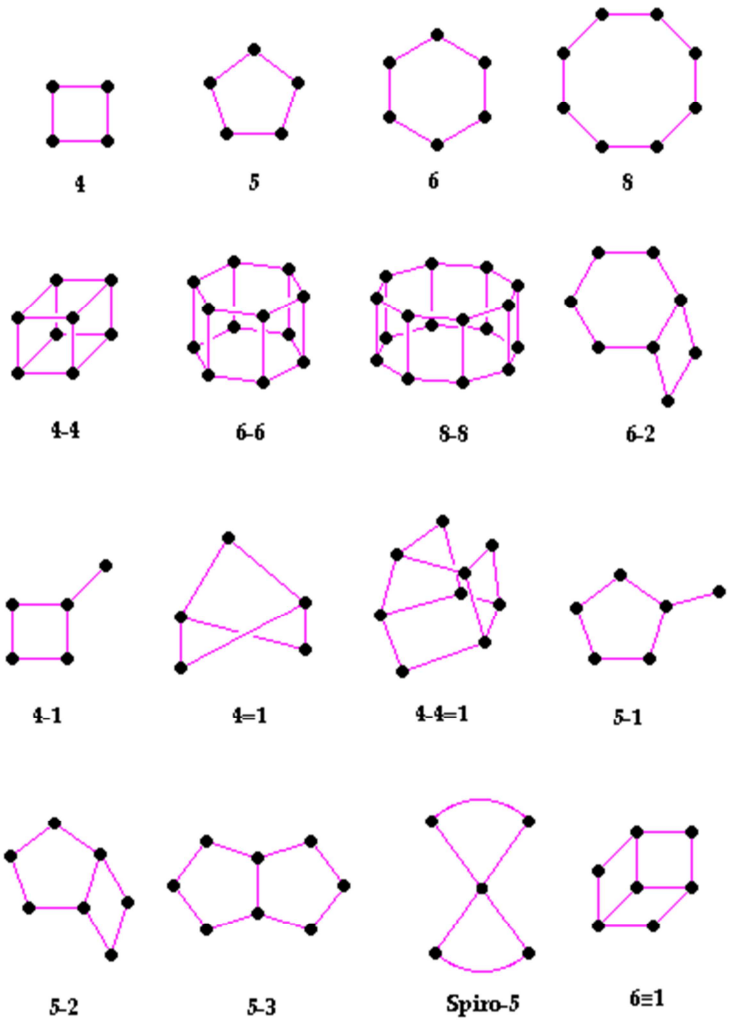

Figure 2.2 Typical SBUs in zeolites. The corner of the polyhedral represents tetrahedral atom T. (Atlas Database 2014)

In addition to having silicon or aluminium as the tetrahedral atom, other compositions have also been synthesised. With finite or infinite component units, there are more than 190 different framework structures with pore size in the range of 4-14 Å (Smith 1998). Each zeolite framework is defined by a three letter code by the Structure Commission of the International Zeolite Association (Ng and Mintova, 2008). Figure 2.3 shows the main zeolite frameworks.

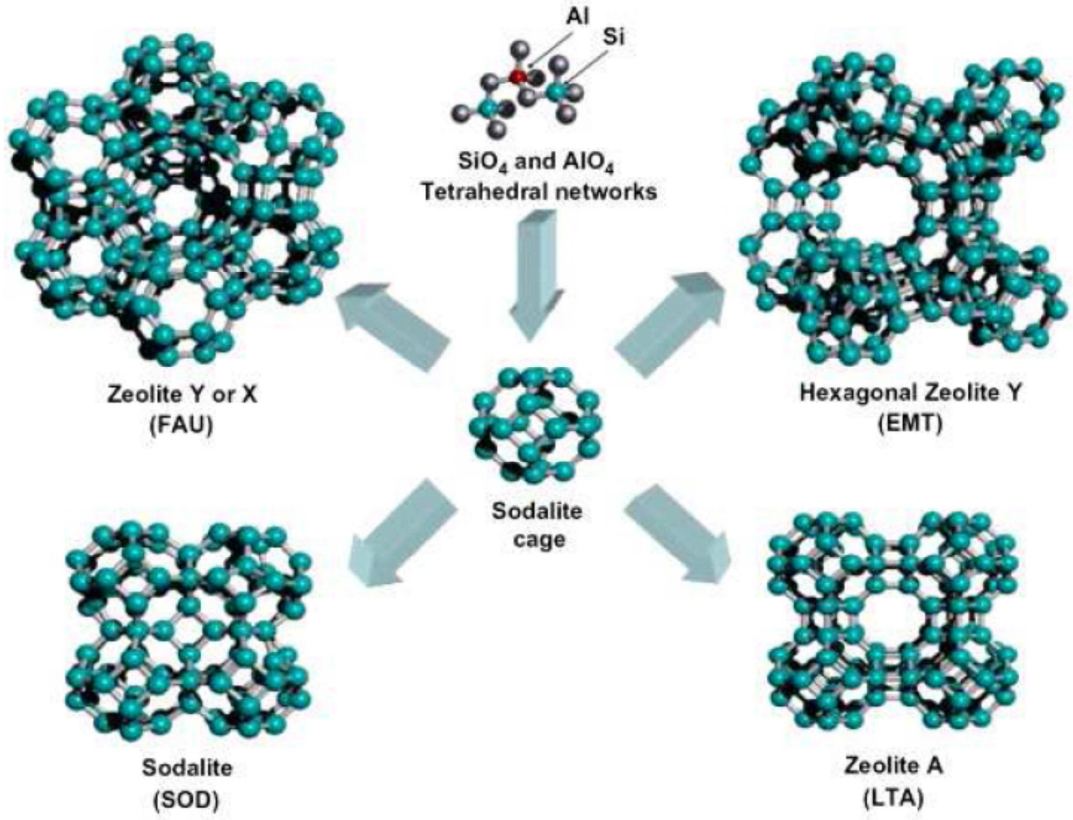

Figure 2.3 Molecular structures of the main types of zeolites (Ng and Mintova 2008)

The faujasite framework, FAU, is the most widely used zeolite in industry. It consists of an array of sod-cages connected by double six-ring (d6R) units, as shown in Figure 2.4 (Stephanopoulos 1984). The cages connected to each other through 12-membered oxygen channels(Atlas Database 2014). It is highly porous and the pore diameter is about 8Å. Ten sodalite cages build up the cavity which has a diameter of 12Å. The unit cell is cubic with Fd-3m symmetry. Zeolites X and Y fall in this framework type and they differ just by the Si/Al ratio in the structure, which is between 1 and 1.5 for zeolite X and between 1.5 and 5.6 for zeolite Y. For the case of CO_2 adsorption in post-combustion capture, low Si/Al ratio is usually needed since more Al means more cations available to bind CO_2 (Pawlesa et al., 2007). The exchangeable cations within the cavities of zeolites affect the electric field present in

zeolite. The polarity of molecules can change their interaction with the electric field. The very large quadrupole moment of CO_2 molecules results in a strong interaction between the electric field of zeolites and CO_2 (Bonenfant et al. 2008). Thus, zeolites X and Y have been widely investigated. Among X and Y classes, it is found 13X is one of the best adsorbents for post combustion applications (Xiao et al. 2008).

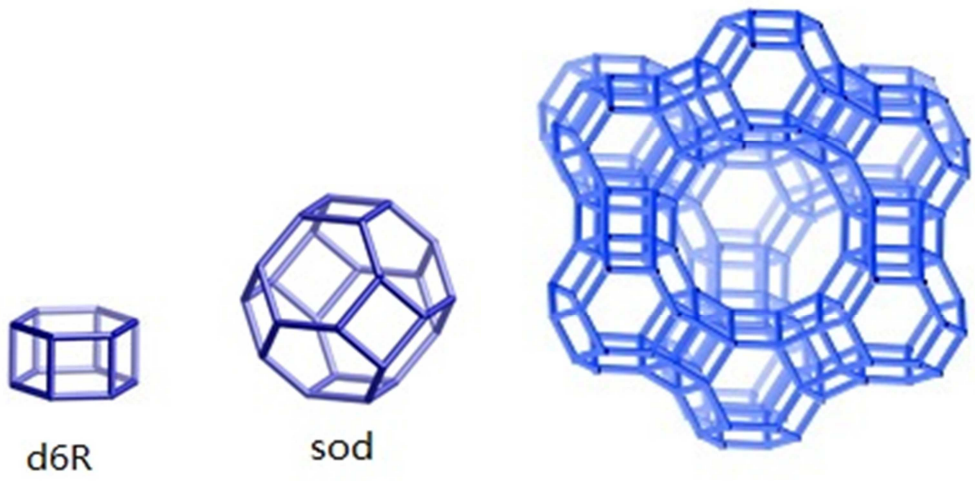

Figure 2.4 Framework structure (right) of FAU type zeolite with sod and d6R unit (Atlas Database 2014)

2.2.2 Adsorption on zeolites

As microporous materials, zeolites have high adsorption capability to capture molecules in their cages. Thus, the micropore volume is very important for their overall saturation capacity and the ability to include strong adsorption sites. For the ring structure of SBU's, the micropore volume is characterised by the diameter of its opening. For example, LTA, the SBU of which is an 8-member ring and its opening is 4.2Å (Atlas Database 2014). This opening is largely dependent on the cations. Since each cation has a specific spatial requirement, the size of the cation and the number of cations present in the channels and cavities will contribute to the final size of the opening. To maintain a neutral structure, the lower the framework charge, with the concomitant decrease in the number of cations occupying space in the pores and cavities, the closer the pore diameter will approach the pure framework diameter. Thus, if the cation is replaced with a larger or smaller one, the zeolite pore will be decreased or enlarged correspondingly. (Szostak 1997) Zeolites 3A, 4A and 5A

for belong to the LTA family but differ for the cations in the structure. 3A contains the large K^+ cations balancing the framework charge. The cations in 4A are Na^+. In 5A, the larger effective pore size is due to the presence of the divalent cation Ca^{2+}. With different size of cations, the pore is partially blocked to different degrees. When sodium is exchanged with the large potassium ion, the pore diameter is contracted and only left very small space for adsorbate molecules. For divalent cation cases, i.e. Ca^+, only half the number of cations are necessary to balance the framework charge, thus less space is occupied.

In many cases, zeolites may act as molecular sieves. The molecules which have access in the zeolite only depend on the size and shape of pores as mentioned in the previous section (Tsuru et al., 2001). Molecules with larger dimension than the zeolite pores are unable to enter the structure. For small pore zeolites selectivity for CO_2 may be increased due to kinetic effects (Lozinska et al 2012). In the present study large pore zeolites are considered, therefore the selectivity is equilibrium driven, but it would be of interest to test in the future the applicability of the dual piston PSA technique also to kinetic separations.

There are a lot of factors that affect the selectivity of adsorption of a gas in a zeolite. Generally speaking, the most important parameters for the separation of gas mixtures by zeolites are the size and the steric hindrance of the compounds as well as the thermodynamic and kinetic selectivity of the compounds towards the zeolite surface (Rezaei 2011).

Generally, the presence of water in the adsorption environment should be avoided, because it decreases significantly the adsorption capacity of cationic zeolites by decreasing strength and heterogeneity of the electric field and by favoring the formation of bicarbonates on the zeolites, which require higher temperature for desorption (Bonenfant et al. 2008).

2.3 Adsorbent applied in this study

Zeolite 13X was chosen as the adsorbent in this study to characterise our novel apparatus. Similar to many other adsorbents, during the adsorption process, pressure, temperature and humidity are very important parameters. Therefore, the adsorption capacity of a zeolite is best represented in the form of adsorption isotherms. Due to its preferably high potential for CO_2

capture, isotherms of CO_2 on different types of zeolite at various temperatures have been reported.

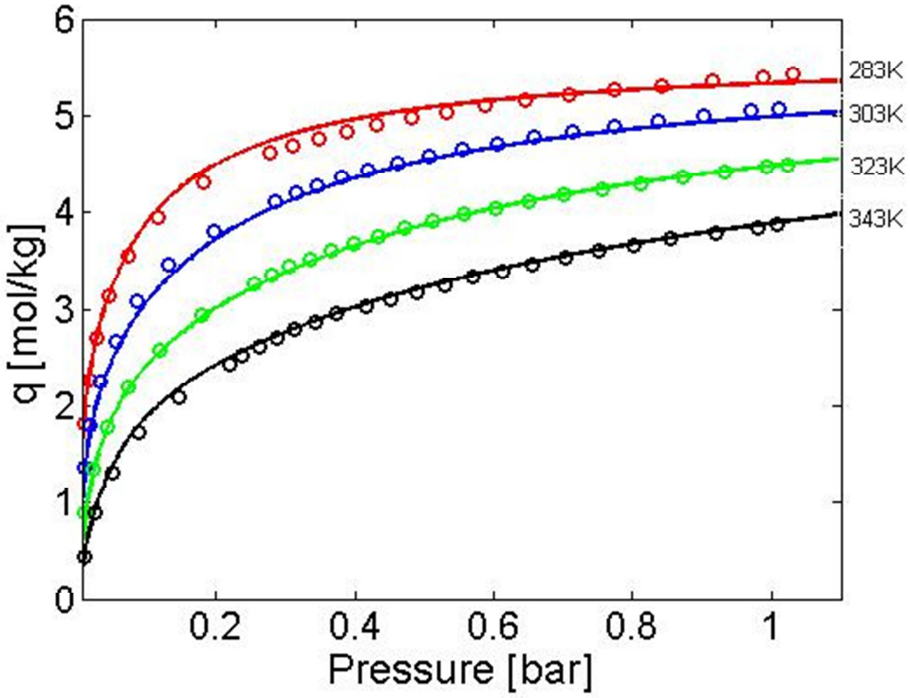

Figure 2.5 CO_2 adsorption isotherms on zeolite 13X at different temperatures. Circular points: experimental data; solid lines: dual-site Langmuir isotherm.

Figure 2.5 shows the experimental results and the fit of the data using a dual-site Langmuir isotherm. The equations are given below.

$$q_i^* = \frac{q_{i,s}^1 b_i^1 P x_i}{1+\sum_{j=1}^{N_c} b_j^1 P x_j} + \frac{q_{i,s}^2 b_i^2 P x_i}{1+\sum_{j=1}^{N_c} b_j^2 P x_j} \qquad \text{Eq.2.1}$$

$$b_i^l = b_{i,0}^l \exp\left(\frac{-\Delta\tilde{H}_i^l}{RT}\right) \qquad \text{Eq.2.2}$$

To provide reliable isotherm information of the adsorbent for this study, experimental data (Figure 2.5) from a Quantachrome Autosorb IQ system and a ZLC (Zero Length Column) system (measured on Autosorb for up to 1 bar partial pressure of CO_2 while the ZLC was for pressures below 0.1bar partial pressure with a helium carrier gas) were obtained from Dr Mangano. Dr Hu and Dr Mangano have applied the Autosorb IQ and ZLC to study the

diffusion mechanism of CO_2 in the same sample of zeolite 13X and concluded that the mass transfer kinetics is governed by macropore diffusion (Hu et al., 2013). The calculation of the effective macropore diffusivity will be given in Chapter 8.

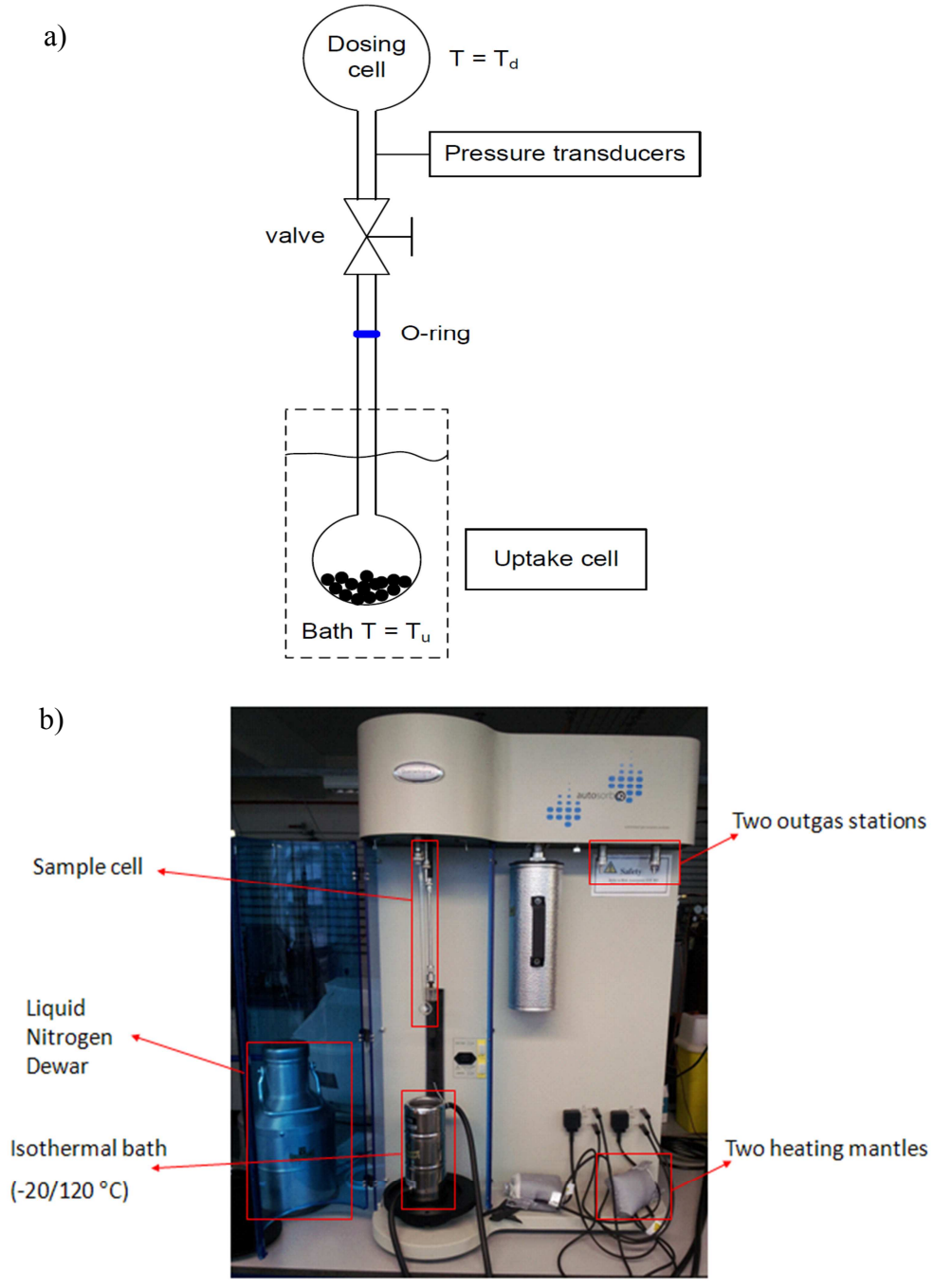

Figure 2.6 (a) Schematic representation of the volumetric system (b) The volumetric system

The Autosorb IQ apparatus is a volumetric system which works by injecting a known volume of adsorbate in a closed cell in which the adsorbent sample is contained. Once the experiment

starts, the system monitors the pressure as the adsorption proceeds. When equilibrium between the adsorbed phase and the gas phase is reached, the system injects a new volume of adsorbate. By successive injections the system collects the equilibrium points (i.e. adsorbed amount and equilibrium pressure) at a fixed temperature. The experiments were carried out on 2.0481 gram of 13X (APG MOLSIV^{TM} from UOP, a Honeywell company) pellets which were regenerated at 548K before each experiment.

Experiments were repeated using N_2, which shows a much lower adsorption capacity and the results are shown in Figure 2.7. Compared to Figure 2.5, the capacity of N_2 is very low in the whole range from vacuum to 1bar.

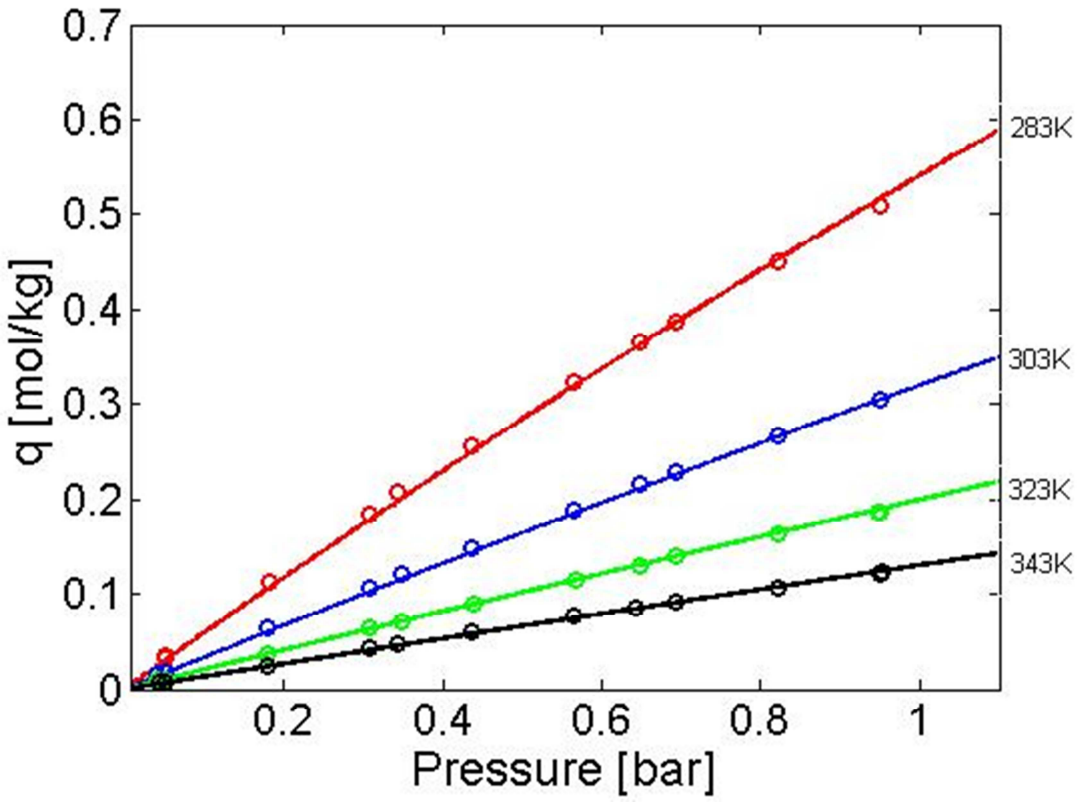

Figure 2.7 N_2 adsorption isotherms on zeolite 13X at different temperatures. Circular points: experimental data; solid lines: dual-site Langmuir isotherm (same saturation capacities as CO_2).

The dual-site Langmuir isotherm parameters are listed in Table 2.1.

Table 2.1 Parameters of the dual-site Langmuir isotherm

Equilibrium CO_2 capacity, q^*_{A1}, [mol/kg]	3.0992
Equilibrium CO_2 capacity, q^*_{B1}, [mol/kg]	1.9819
Equilibrium N_2 capacity, q^*_{B2}, [mol/kg]	3.0992
Equilibrium N_2 capacity, q^*_{B2}, [mol /kg]	1.9819
Langmuir Equilibrium constant of the first site for CO_2, b_{A1}, [bar^{-1}]	2.9328×10^{-5}
Langmuir Equilibrium constant of the second site for CO_2, b_{A2}, [bar^{-1}]	3.8307×10^{-5}
Langmuir Equilibrium constant of the first site for N_2, b_{B1}, [bar^{-1}]	1.9921×10^{-5}
Langmuir Equilibrium constant of the second site for N_2, b_{B2}, [bar^{-1}]	1.9921×10^{-5}
Heat of adsorption of the first site for CO_2, ΔH_{A1}, [J mol^{-1}]	–30031
Heat of adsorption of the second site for CO_2, ΔH_{A2}, [J mol^{-1}]	–31006
Heat of adsorption of the first site for N_2, ΔH_{B1}, [J mol^{-1}]	–37449
Heat of adsorption of the second site for N_2, ΔH_{B2}, [J mol^{-1}]	–20205

The additional physical properties of the adsorbent are listed in Table 2.2. In our experiments 12.98 gm were packed in a stainless steel column.

Table 2.2 Characterisation of adsorbent bed used in this study

Adsorbent	zeolite 13X
Shape of adsorbent	Spherical
Average adsorbent diameter [mm]	4±1
Bulk density, ρ, [kg m^{-3}]	471.2
Skeletal density, ρ_{skel}, [kg m^{-3}]	1403
Bed void fraction, ε, [–]	0.43
Pellet void fraction, ε_p, [–]	0.27
Crystal void fraction, ε_{cry}, [–]	0.5
Column length [m]	0.13
Column radius [m]	0.0078

The pellet void fraction was measured by mercury porosimetry. The crystal void fraction was calculated from the zeolite 13X framework and the bed void fraction was calculated from the helium experiments carried out on the dual piston system in Chapter 7. The details of the dual piston system and the experimental procedure will be detailed in Chapter 5. The bulk density is from UOP (UOP 2003).

2.4 Conclusions

In this chapter, four main classes of adsorbents for carbon capture were introduced. Zeolites are the most widely reported physical adsorbents for CO_2 capture. Its framework and adsorption process were presented very briefly. To separate CO_2 from the other gases, the selectivity of adsorption of a gas in a zeolite depends on man factors. The most important parameters for the separation of gas mixtures by zeolites are the size and the steric hindrance of the compounds as well as the thermodynamic and kinetic selectivity of the compounds towards the zeolite surface. In this thesis, zeolite 13X was chosen as the adsorbent to characterise our novel apparatus. Its isotherm property of CO_2 was acquired from a Quantachrome Autosorb IQ system and a ZLC system. The adsorbent bed used in this study was characterised and is given here. These parameters will provide the basic information for the experimental data analysis.

3. The Need for a Novel Adsorption Dynamic Technique

3.1 Introduction

Pressure swing adsorption (PSA) processes are receiving considerable interest as a separation process for Carbon Capture and Storage (CCS) (Kikkinides et al., 1993; Takamura et al., 2001; Silva and Rodrigues, 2001; Ahn, 2002), for H_2 recovery from coal gas (Hayashi, 1996) and for portable oxygen generators (Dechene 1985; Dong 1999). An excellent overview of PSA is presented in the monograph by Ruthven et al. (1993). The key advantages of PSA are a lower energy penalty and lower capital costs compared to other separation processes. Further enhancements in carbon capture applications can be achieved if the cycle time is reduced given the scale of the challenge, i.e. a 1 GW coal fired power plant emits approximately 900 tonnes of CO_2 per hour (Lackner et al. , 1997).

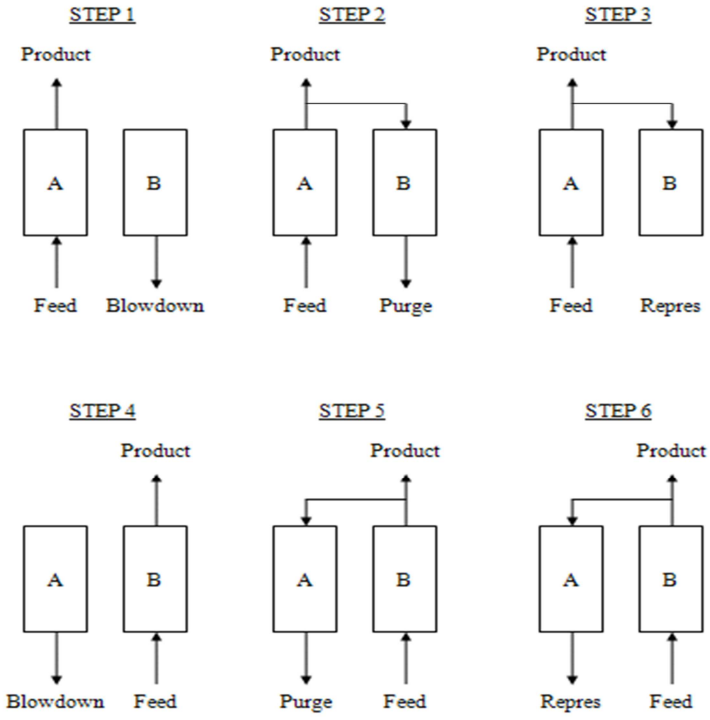

Figure 3.1 A 2-bed 6-step Skarstrom cycle

Since the invention of the PSA process, several variants have been developed. The early PSA cycles developed by Skarstrom (Skarstrom 1960) and Air Liquide (Daniel and De 1958) utilised a strategy with two-beds cycled through six steps. This cycle has been in use since then as a prototype of PSA. This typical Skarstrom PSA cycle is shown in Figure 3.1.

The sequence of the steps is operated in such a way as to give a continuous product stream.

1 Feed at high pressure P enters column A while the weakly-adsorbing compound flow exits the column. Column B depressurises by exhausting waste gas (strong-adsorbing compound enriched).
2 Feed and product flows continue as in step 1, but a portion of the product flows counter-currently down column B. This portion of the product flow which passes through column B counter currently will be referred to as low pressure purge flow.
3 Feed and product flows still continue as in step 1 but the output valve of column B is closed to allow repressurisation with a portion of the product flow from column A.

In the next three steps, column A and B reverse roles:

4 Feed at high pressure enters column B while product leaves the column. Column A depressurises.
5 Feed and product flows continue as in step 4 but part of the product goes to column A for purging.
6 Feed and product flow continue in column B. Column A begins to repressurise with a portion of the low pressure purge flow from column B. After this step, one cycle of PSA operation is completed and the bed is ready to start the cycle again.

To improve the purity and recovery of light or heavy products or both, as well as to design PSA processes for multi-component feed mixtures, several modified configurations have been proposed based on Skarstrom's strategy with a wide range of distinct operating steps such as light product or heavy product pressurisation, desorption with heavy product as purge gas, co-current depressurisation, pressure equalisation etc (Cen and Chen, 1985; Doong and Yang, 1987; Malek and Farooq, 1997; Taficzyk, 1997; Xiao et al., 2009; Zhou et al., 2002).
It is not practical to carry out extensive experimental tests directly on a PSA cycle for several reasons:

1) Multiple columns, typically requiring 50 grams of material each, are needed.

2) Gas lines and connections may limit the fastest cycle time possible on a given experimental system, especially when desorbing under vacuum conditions.
3) Multiple experiments with varying gas flow rates and cycle configurations are time consuming and expensive to run.

To address points 1-2 the first option is to consider single column rapid PSA processes.
Rapid PSA usually only uses one column and reduces the cycle time to a few seconds which can lead to a very high productivity of the separation process (Kowler and Kadlec, 1972). Rapid PSA (RPSA) processes represent the extreme limit in which the cycle time is dramatically reduced in an effort to shrink the size of the equipment for a given production rate (Sircar and Hanley, 1995). There are two basic variants of RPSA:

a) A normal adsorption column is pressurised and evacuated in a two-step cycle. This is suitable when large quantities of relatively low purity gas such as oxygen-enriched air are required to improve oxidation processes (Todd and Webley, 2006).
b) A column packed with small particle size materials has one end where the pressure is cycled and continuous withdrawal of the light component is achieved at the other end of the column. This process is limited by the high energy penalty (Alpay et al., 1994).

The first type of RPSA process has both steps usually of similar duration, in the range 1-5 seconds (Kikkinides and Georgiadis, 2009). So the total cycle time is normally of the order 2-10 seconds, which is much faster than a traditional PSA system with cycle times in the order of minutes (Ruthven et al., 1993). To enhance gas-solid adsorption and heat transfer kinetics, RPSA usually is applied with small size particles, ranging from 200 to 700 μm in diameter (Chai et al. 2011). Because of these features, the pressure gradients in the bed are steep and vary periodically, which lead to an effective self-purging of the bed. For large scale operations, the pressure drop and energy consumption are usually major issues. Therefore, RPSA technology is only economically viable for small or medium scale operations unless monolithic type structures are used (Ruthven, 2011).

A further development from RPSA processes are piston driven PSA processes. The use of a single piston in PSA for gas separation dates back to 1979 when Eriksson published his

fractionating apparatus shown in Figure 3.2 (Eriksson, 1979). Mixed gases were fed in through the inlet 17. Piston 11 is acting as a compressor to control the system volume. Similar to traditional PSA, the more strongly-adsorbed compound is retained while the light component exits through 26. When the bed volume is expanded, a purge flow of the product gas comes in through inlet 38 and desorption occurs.

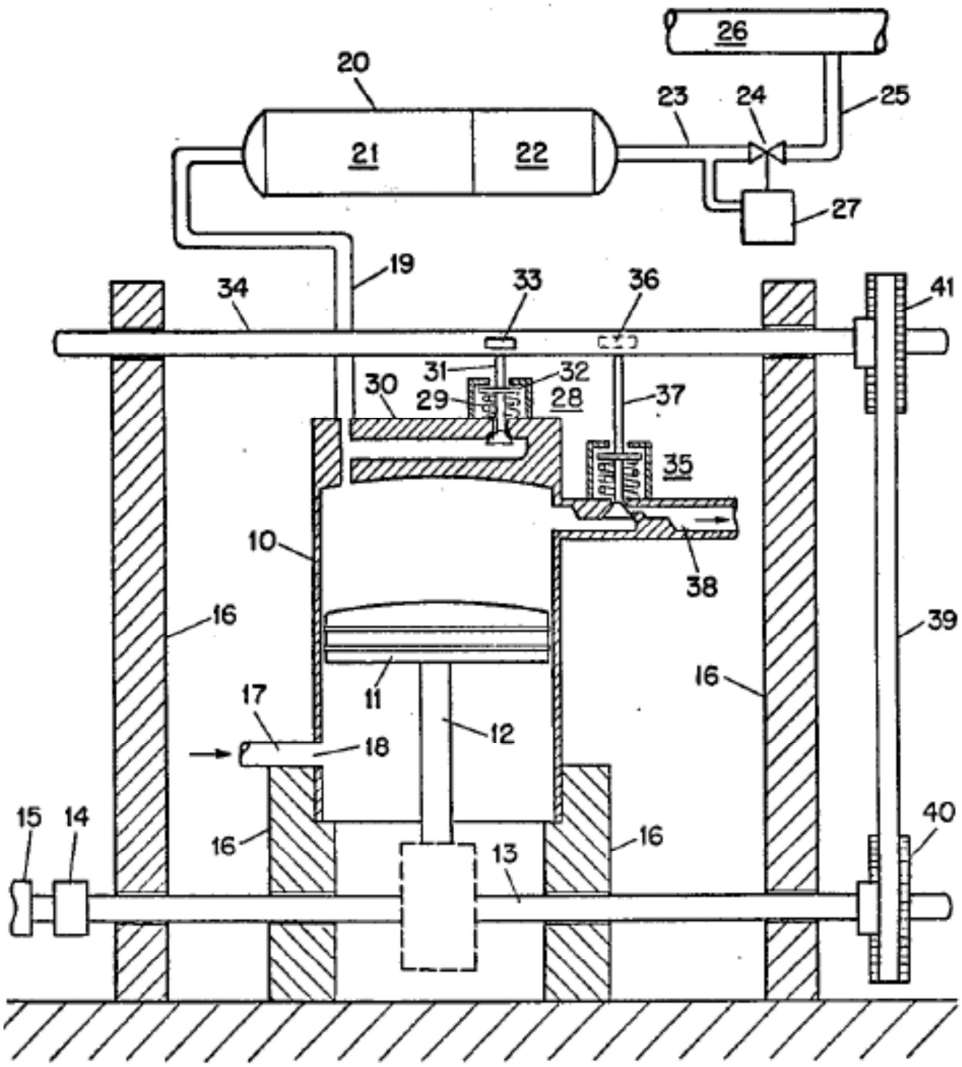

Figure 3.2 Single Piston Driven PSA by Eriksson (Eriksson 1979)

Inspired by this invention a dual-reflux, dual piston PSA was proposed by Keller and Kuo (1982), and shown in Figure 3.3. This system operates as a parametric pump (Ruthven et al., 1994). By cyclically varying the fluid pressure, temperature or other intensive thermodynamic variables, the equilibrium solute content of the particles in the parametric pump is caused to vary in a periodic fashion. This variation leads to a cyclic solute exchange between the solid

and fluid phases. The system thermodynamic variables are usually changes by configuring different running conditions, such as the frequency, phase angle and wave form (Wilhelm et al. 1968). For Keller and Kuo's system, the movement of the pistons induces cyclic gas flow and pressure variations on the gas mixture, which results in a high productivity separation that can produce both pure heavy and light components. The separation is achieved by varying the phase angle and stroke lengths of the pistons. Product withdrawal at the end of the pistons is controlled by valves.

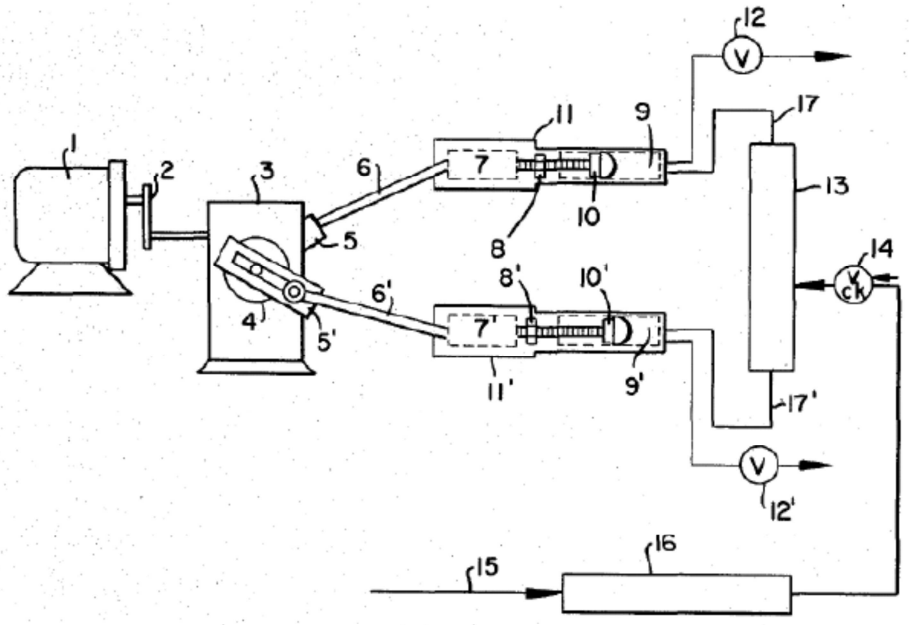

1 – Motor
2 – Chain drive
3 – Gear box
4 – Split hub
5, 5' – Stroke length adjustment bars
6, 6' – piston arms
7, 7' – Piston guides
8, 8' – Piston end volume adjustment nuts
9, 9' – End surge volumes
10, 10' – Piston heads
11, 11' – Pistons
12, 12' – Valves
13 – Column
14 – Check Valve
15 – Feeding lines
16 – Dryer
17, 17' - Lines

Figure 3.3 Dual-Piston Driven PSA configured by Keller and Kuo (Keller and Kuo, 1982)

Keller and Kuo demonstrated in their studies that for air separation on zeolite 13X, a stroke length ratio of around 3.5, which is roughly the ratio of the equilibrium constants of oxygen and nitrogen, and a lead of the piston with the short stroke length of 45˚ (1/8 cycle ahead) gives the best productivity. They also discovered that two pure products from the stripping and rectifying

sections could be recovered when feed is introduced midway through the column. These results are confirmed by a recent numerical optimisation study (Beck et al., 2012). Dual-reflux PSA processes will be discussed briefly in section 3.3.

Piston-PSA processes have been studied in the literature. Sakoda and Suzuki (Suzuki et al., 1996; Suzuki et al., 1997) modeled a single piston rapid PSA process. Much of the study focused on the adsorbent bed itself. The effect of moisture on the bed has been studied by comparing the performance of hydrophobic and hydrophilic adsorbent respectively. It is found that the latter led to poor separation performance so moisture content should be controlled during the separation.

Singh and Jones (1997) presented a non-isothermal model for the dual-piston PSA process. Farooq et al. (Farooq and Thaeron, 1998) developed an isothermal model for a dual piston driven process using a parallel passage contactor, showing the benefits of contactors with reduced pressure drops. Rajendran et al. (2002) did a further study of the dual piston PSA process for air separation based on zeolite 13X. They confirmed that a stroke length ratio equal to the ratio of the equilibrium coefficients of the components gives better performance. Use of adsorbents with higher equilibrium selectivity improves separation performance. Since the transport in the adsorbent was macropore diffusion controlled, reduction in particle size enhances the separation. However, further reduction of the particle size might not prove to be beneficial, because smaller particle size leads to higher pressure drop. They also observed that higher mean pressure of the system leads to improved separation (Rajendran et al., 2002), and this was attributed to mass transfer resistances.

The dual piston PSA provides the means to overcome all 3 requirements identified above. If the process is transformed into an experimental technique where the system is operated at total reflux, no gas is consumed therefore reducing significantly the costs of the experimental campaign. This can also be seen as a potential extension of frequency response techniques used to characterise adsorbents which are summarised in the following section.

3.2 Frequency Response techniques

Frequency Response (FR) is one of the most important methods to study the kinetics in various processes (Stephanopoulos 1984). It is a perturbation method, in which some property of a system is varied periodically about an equilibrium state and dynamic measurements are made on the responses of the system. By repeating the experiment and changing the period of the perturbation it is possible to generate a spectrum of the system responses, which contains a lot of information that it is assumed to be the finger-print database of the processes in the system.

In adsorption measurements there are two classes of FR techniques:

1) Closed systems where the volume is perturbed and the pressure (Yasuda 1982) or temperature (Grenier et al., 1999) are measured. This system corresponds to a differential version of the single piston PSA process with total reflux.
2) Open systems where either the pressure (Glover et al. 2008; Sward and LeVan 2003) or the concentration (Boniface and Ruthven, 1985) is varied. This is a variant of the classical breakthrough experiment but suffers from the use of large quantities of gas.

The technique was first used in adsorption by Yasuda to measure diffusion coefficients in gas-zeolite systems by applying a sinusoidal-wave perturbation to the equilibrium gas phase volume of the system.(Yasuda and Saeki, 1978; Yasuda, 1982; Yasuda, 1994) He considered a case where a sorption system at equilibrium is perturbed by changing the equilibrium volume and the change is described by

$$V = V_e(1 - v_a e^{i\omega t}) \qquad \text{Eq.3.1}$$

where V_e denotes the mean volume and v_a is the relative amplitude of the volume variation. ω is the angular velocity of the sinusoidal generator. In the closed system, the pressure P and the concentration c of a diffusing substance in a medium or a pore are perturbed and they are expressed at cyclic steady state by

$$P = P_e(1 + pe^{i(\omega t+\varphi)}) \qquad \text{Eq.3.2}$$

$$c = c_e(1 + \gamma e^{i(\omega t+\varphi-\chi)}) \qquad \text{Eq.3.3}$$

The relative amplitudes p, γ and the phase lags φ, χ depend on the angular velocity of the perturbation.

Yasuda showed that the experimental measurements could be interpreted easily using the in-phase out-of-phase functions:

in-phase: $(P_B / P_Z)\cos\phi_{Z-B} - 1 = K_f\delta_{in} + S$ Eq.3.4

out-of-phase: $(P_B / P_Z)\sin\phi_{Z-B} = K_f\delta_{out}$ Eq.3.5

In which, $\phi_{Z-B} = \phi_Z - \phi_B$, ϕ_Z and ϕ_B are the phase lags determined in the presence and the absence of adsorbent, respectively. P_B and P_z are the pressures response to the volume perturbation in the absence and presence of adsorbents, respectively. K_f is a constant related to the gradient of the adsorption isotherm at the equilibrium pressure, S is a constant that represents a rapid adsorption or desorption process. δ_{in} and δ_{out} are the overall in-phase and out of phase characteristic functions, respectively, which depend on the theoretical models describing the overall kinetic processes of a system. (Yasuda 1994; Yasuda 1982)

Lovat Rees improved the technique by the use of a square-wave volume perturbation which allowed a reduction of the cycle time to 0.1 seconds resulting in an expansion of the frequency range that could be measured. (Shen and Rees, 1991; Shen and Rees, 1993; Shen and Rees, 1994)

Many theoretical models were developed to study the diffusion processes in micropore systems. Yasuda originally used a linear isothermal model describing a single diffusion process in a periodical adsorption system (Yasuda, 1982; Yasuda, 1994; Yasuda, 1976; Yasuda and Saeki, 1978). Sun et al. (1993) showed that in batch systems small perturbations in the system cannot eliminate temperature effects if they are present in the system (Sun et al.,

1993). This is due to the fact that although the loading changes caused by the heat of adsorption released are reduced, as the perturbations are decreased in magnitude, they scale at the same rate as the overall change in the loading of the system. Grenier and Meunier included the temperature response into the original pressure response system and developed a mathematical model which allows to measure the heat transfer resistance (Bourdin et al., 1998; Grenier et al., 1999). They did so through the use of infrared measurements of the sample temperature. They found that the thermal relaxation of the gas was fast enough that one could assume that the gas phase temperature was constant and that heat transfer from the particle to the gas was the controlling heat transfer resistance. Do analysed different diffusion mechanisms in the adsorbent and extended the FR technique to non-isothermal systems (Do 1998; Jordi and Do 1993; Jordi and Do 1994). He used high frequency response functions to analyse the isothermal and non-isothermal nonlinear frequency response system and found the second-order frequency response function can provide enough information to identify different kinetic processes (Petkovska and Do, 1998; Petkovska and Do, 2000). Do and LeVan's group explored the flow-through frequency response method and proved it has some advantages, such as ease of implementation of a wide range of frequencies, reducing heat effects and potentially using large relative amplitudes (Park et al., 1998a; Park et al., 1998b; Do et al., 2000; Wang and LeVan, 2008). Bonivace and Ruthven (1985) were the first to develop the concentration frequency response. They demonstrated that with weakly adsorbed species it is possible to measure intracrystalline diffusional time constants spanning a range of about six orders of magnitude (Boniface and Ruthven, 1985). LeVan's group used pressure-swing frequency response (PSFR) and concentration-swing frequency response (CSFR) methods to study mass transfer rates for both pure and mixed gases and vapors and have applied the methods to carbon molecular sieve, silica gel and activated carbon materials (Glover et al., 2008; Wang and LeVan, 2008; Wang and LeVan, 2007; Wang and LeVan, 2005a; Wang and LeVan, 2005b). The frequency of the experimental system can reach up to 3Hz (Wang and LeVan, 2007).

3.3 Dual-Reflux PSA

The Dual-Reflux PSA can be compared to a distillation tower. In contrast to a conventional PSA system, it has both light reflux and heavy reflux. Concentration of product gas from the

adsorption column can be reduced in a stripping section, at the same time, less-adsorbing gas is enriched in an enriching section, where the purity can be further rectified and the adsorbing gas can be sent back to the stripping section. Figure 3.4 shows a basic Dual-Reflux PSA. Dual-Reflux cycles are characterised by reflux streams among the beds and sometimes by the introduction of the feed at some middle point depending on the feed gas concentration, thus reproducing the stripping and rectifying sections of distillation columns (Diagne and Goto , 1994).

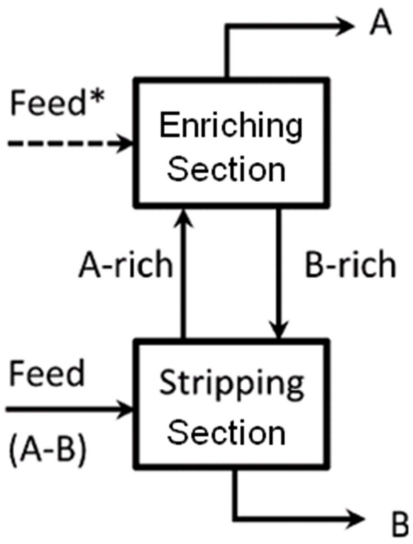

Figure 3.4 A Dual-Reflux PSA (Grande and Blom, 2012)

Reynolds explained the difference between “stripping" section and “enriching” section: the word “stripping” is used to denote that the feed step is conducted at high pressure and that the adsorbent bed strips the heavy component from the gas phase, because of strong selective adsorption. The “enriching” section works at low pressure so the gas phase is enriched with heavy component due to desorption (Reynolds and Ebner, 2006).

An idealised analysis of the Dual-Reflux PSA conducted by Ebner and Ritter (2002, 2004) was carried out on the basis of the isothermal equilibrium theory. In this analysis, the ideal Dual-Reflux PSA was shown to achieve the separation of a binary mixture with high purity and high recovery, even reaching 100%. Although there are several simplifying assumptions, this analysis proved the separation efficiency of a Dual-Reflux PSA. It is interesting to note that the

recent studies on the dual-reflux PSA process have not recognised explicitly the fact that the dual piston PSA process falls in this category and the origins of this approach go back to the early 1980s.

3.4 Conclusions

As mentioned in Chapter 1 and Chapter 2, the adsorbents for carbon capture are developed so fast that their properties can not be obtained immediately by the current instruments. Therefore, there is a need to develop novel laboratory measurements for rapid testing of the adsorbents.

The dual piston PSA system operated at total reflux can be seen both as a derivation from the original Keller and Kuo (1982) process and as an extension of the closed volume frequency response apparatus of Yasuda (1982). While a single piston PSA process could also be used to characterise an adsorbent the key advantages of operating a dual piston configuration are:

1) Pressure drops can be fully quantified independently using experiments where the two piston are fully out of phase with equal stroke lengths, i.e. there is no change in the total volume;
2) The dual-reflux configuration allows the option of separating a binary mixture and determining in a closed system the maximum separation capability of a single adsorption column. If direct measurements of concentration in the closed system were to be possible, the technique could also be applied with limited modelling required.

The current configuration of the dual piston apparatus allows only measurements of pressures and temperatures, therefore the full interpretation of the results is only possible through the application of a dynamic adsorption simulator. The dual piston PSA models and the simulator have been developed in collaboration with Dr Friedrich and will be presented in Chapter 4.

4. Mathematical Model of the DP-PSA

4.1 Introduction

Due to the large number of experiments under different conditions that can be run using the DP-PSA system, there is a need for a simulation tool which can accurately describe the adsorption process over a wide range of experimental conditions. In this study, we applied a model which was developed by Dr. Friedrich (Friedrich et al. 2013) and is briefly introduced in this chapter.

A schematic of the adsorption column is shown in Figure 4.1. The flow through the packed bed is described by the axial dispersed plug flow model (Ruthven 1984).

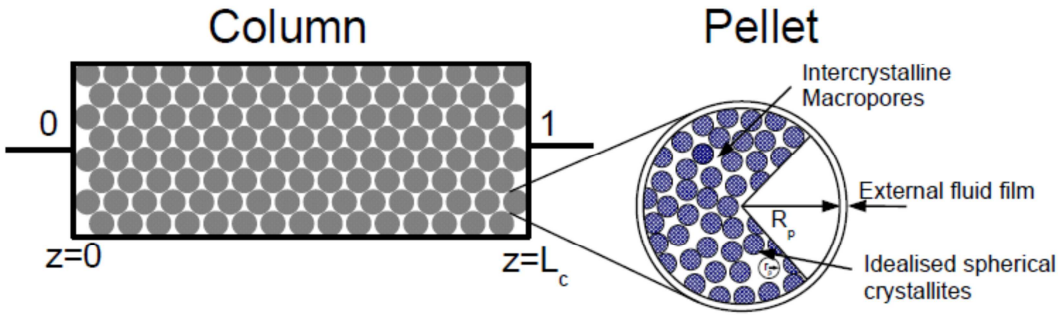

Figure 4.1 Schematic of an adsorption column showing the two inlets and the adsorbent pellets. The inset shows a schematic of an idealised adsorbent pellet including the spherical crystallites.

A schematic diagram of an adsorbent pellet can be found in the inset in Figure 4.1. The adsorbent pellet consists of microporous crystallites which are held together by a binder; thus the pellet has inter-crystalline macropores and intra-crystalline micropores. The pellet macropore void fraction is denominated ε_p. Figure 4.1 shows an idealised spherical pellet and thus the radius R_p is the radius of the equivalent volume sphere with volume V_p. The non-sphericity coefficient φ_p allows the calculation of the surface area A_p. The microporous crystallites are also represented and modelled as idealised spherical particles with radius r_p.

In the model, the governing equations for the pistons and the column will be described separately and linked together through boundary conditions. The models are based on the following assumptions:

1. Axial dispersed plug flow
2. Momentum balance: Pressure drop described by the Ergun equation
3. Energy balance: Non-isothermal with $T_f \neq T_p$ and $T_w = T_w(z,t)$
4. Mass transfer: macropore LDF(Linear Drive Force) and micropore LDF
5. Adsorption isotherm: dual-site Langmuir
6. The gas concentrations and temperature in the pistons are assumed to be uniform
7. The dead volume in the system is placed at the top of the piston-cylinder assemblies
8. Flow resistances between the pistons and the column are included.

4.2 Governing equations for the column

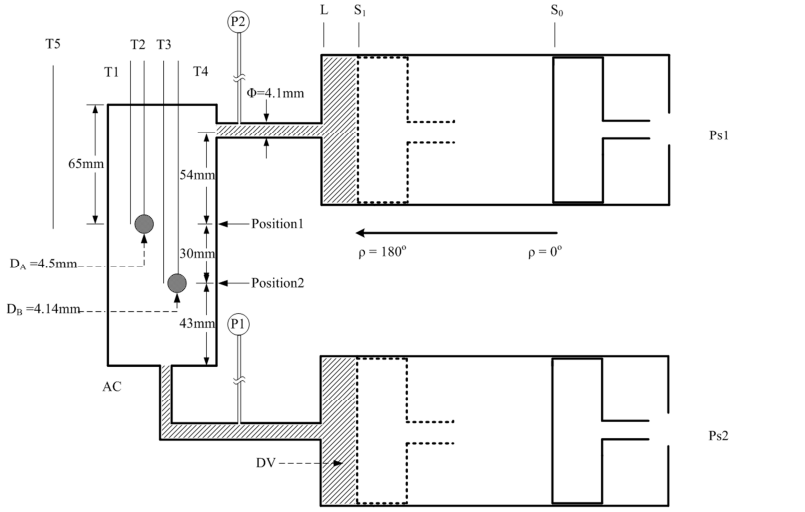

Figure 4.2 Schematic of the adsorption column and the two piston-cylinder assemblies showing the dimensions and also the location of the thermocouples

The adsorption column is placed between the two pistons. The column dimensions can be found in Figure 4.2. The detailed description is given in the next chapter.

Since the flow is assumed to be dispersed plug flow the material balance along the column is given by

$$\frac{\partial c_i}{\partial t} + \frac{(1-\varepsilon)}{\varepsilon} \cdot \frac{\partial \overline{Q}_i}{\partial t} + \frac{\partial (c_i \cdot v)}{\partial z} + \frac{\partial J_i}{\partial z} = 0 \qquad \text{Eq.4.1}$$

$$\overline{Q}_i = \varepsilon_p c_i^m + (1-\varepsilon_p)\overline{q}_i \qquad \text{Eq.4.2}$$

Here and from now on the index i goes from 1 to the number of components N_c. The mass transfer in the macro- and micropores is given by

$$\varepsilon_p \frac{dc_i^m}{dt} + (1-\varepsilon_p)\frac{d\overline{q}_i}{dt} = k_i^p \frac{A_p}{V_p}(c_i - c_i^m) \qquad \text{Eq.4.3}$$

$$\frac{d\overline{q}_i}{dt} = k_i^{cr} \frac{3}{r_p}(q_i^* - \overline{q}_i) \qquad \text{Eq.4.4}$$

where q_i^* is the sorbate concentration in the adsorbent crystal at equilibrium. This value depends on the adsorption isotherm used. Here the dual-site, multi-component Langmuir isotherm is considered

$$q_i^* = \frac{q_{i,s}^1 b_i^1 P x_i}{1 + \sum_{j=1}^{N_c} b_j^1 P x_j} + \frac{q_{i,s}^2 b_i^2 P x_i}{1 + \sum_{j=1}^{N_c} b_j^2 P x_j} \qquad \text{Eq.4.5}$$

$$b_i^l = b_{i,0}^l \exp\left(\frac{-\Delta \widetilde{H}_i^l}{RT}\right) \qquad \text{Eq.4.6}$$

The energy balance in the column is written in terms of the internal energy in the fluid and pellet plus a term for the column wall temperature

$$\varepsilon\frac{\partial \breve{U}_f}{\partial t}+(1-\varepsilon)\frac{\partial \breve{U}_P}{\partial t}+\varepsilon\frac{\partial\left(\breve{H}_f\cdot v\right)}{\partial z}+\frac{\partial J_T}{\partial z}+\sum_{i=1}^{N_c}\frac{\partial\left(J_i\tilde{H}_i\right)}{\partial z}+h_w\frac{A_c}{V_c}\left(T_g-T_w\right)=0 \qquad \text{Eq.4.7}$$

$$\frac{d\breve{U}_P}{dt}=\varepsilon_P\frac{d\breve{U}_g}{dt}+(1-\varepsilon_P)\frac{d\breve{U}_S}{dt}=h_p\frac{A_P}{V_P}\left(T_g-T_P\right) \qquad \text{Eq.4.8}$$

$$\rho_w\hat{c}_{P,w}\frac{dT_w}{dt}+h_w\frac{A_c}{V_w}\left(T_w-T_f\right)+U\alpha_{wl}\left(T_w-T_\infty\right)=0 \qquad \text{Eq.4.9}$$

The pressure in the system is calculated from the gas phase concentration and temperature through the ideal gas law. The interstitial flow velocity v is calculated from the Ergun equation

$$-\frac{\partial P}{\partial z}=\frac{150\mu(1-\varepsilon)^2}{d_p^2\varepsilon^2}v+\frac{1.75\rho_f(1-\varepsilon)}{d_p\varepsilon}v|v| \qquad \text{Eq.4.10}$$

The form of Eq. 4.10 reflects the fact that in the DP-PSA unit flows are reversing during a cycle.

4.3 Column boundary and initial conditions

The boundary equations for the mass and energy balance in the column are given by the Danckwert's boundary conditions which can be written concisely for reversing flows as (Rouse 2004)

$$J_T\big|_{z=0}=\frac{v+|v|}{2}\left(\breve{H}_{f,0-}-\breve{H}_{f,0}\right) \qquad \text{Eq.4.11}$$

$$J_T\big|_{z=L}=\frac{v-|v|}{2}\left(\breve{H}_{f,L+}-\breve{H}_{f,L}\right) \qquad \text{Eq.4.12}$$

$$J_i\big|_{z=0}=\frac{v+|v|}{2}\left(c_{i,0-}-c_{i,0}\right) \qquad \text{Eq.4.13}$$

$$J_i\big|_{z=L}=\frac{v-|v|}{2}\left(c_{i,L+}-c_{i,L}\right) \qquad \text{Eq.4.14}$$

The velocities at the column boundaries are calculated from the resistance term between the pistons and the column. Initially the column is at uniform pressure, temperature and gas phase concentration. The adsorbent material is assumed to be in equilibrium with the set gas phase concentration.

4.4 Governing equations for the piston

In the current study each piston performs a sinusoidal cycle and can thus be described by the following equation

$$S(t) = S_0 + \frac{S_1 - S_0}{2}\left(1 - \cos\left(\omega t + \varphi\right)\right) \qquad \text{Eq.4.15}$$

where S_0 and S_1 are the start and end position of the piston, respectively, $\omega = 2\pi / t_c$ is the cycle frequency and φ the initial piston offset. The material balance in the pistons is given by

$$\frac{d\left(c_i V\right)}{dt} = \frac{F + |F|}{2}\frac{c_{i,n}}{c_{T,n}} + \frac{F - |F|}{2}\frac{c_i}{c_T} + f(t) \qquad \text{Eq.4.16}$$

where $f(t)$ characterises the leak of the piston and the subscript n indicates the concentration in the neighbouring unit, i.e. the concentration at the top or bottom of the column depending on the piston. The flow rate at the piston outlet is modelled through a resistance term

$$F = \kappa\left(P_n - P\right) \qquad \text{Eq.4.17}$$

The energy balance includes heat transfer through the wall

$$\frac{dU_f}{dt} = F\widetilde{H} - P\frac{dV}{dt} - A_c h_w\left(T_f - T_w\right) \qquad \text{Eq.4.18}$$

$$\rho_w \hat{c}_{P,w}\frac{dT_w}{dt} = h_w\frac{A_c}{V_w}\left(T_f - T_w\right) + h_w\frac{A_{c,o}}{V_w}\left(T_{\infty,o} - T_w\right) + U\alpha_{wl}\left(T_\infty - T_w\right) + g(v,T) \qquad \text{Eq.4.19}$$

$$g(v,T)=\frac{f_1}{1+\exp\left(\frac{-(t-f_2)}{f_3}\right)} \qquad \text{Eq.4.20}$$

Here the terms on the right hand side of Eq.4.19 are the heat transfers to the piston wall from the gas inside the piston; from the space between the piston and the oven; and from the oven, respectively. The term $g(v,T)$ characterises the heat generated by friction, the need for which became evident once the thermocouples were added to the experimental system.

4.5 Other parameters

In the model, the adsorption isotherm parameters for zeolite 13X are assumed constant in accordance with the experimental isotherms determined on the Autosorb iQ systems (see Chapter 2).

We assume that the available site in the adsorbent for adsorption is constant, so the saturation capacity for CO_2 and N_2 are the same in accordance with thermodynamic consistency (Rao and Sircar 1999).

Table 4.1 lists all the input variables and parameters needed in the model. In the experiment, the variables with * can be configured by the automated LabVIEW interface, which will be detailed in Chapter 6. The variables marked with △ are the variables which can be determined from DP-PSA experiments. In this thesis, the adsorption isotherm (Quantachrome Autosorb IQ system and a ZLC) and heat/mass transfer kinectics (correlations) of the adsorbent were taken from the literature to validate the DP-PSA experiments.

Table 4.1 The list of the variables and parameters needed in the model

General	With pressure drop or not	Size of output time step
	Isothermal or non-isothermal	Dynamic CSS (cyclic steady state)?
	Wall temperature is constant or not	CSS tolerance
	Number of components	Screen output flag
	Component ID	File output flag

	Restart flag	Relative tolerance
	Number of cycles	Absolute tolerance
	Cycle time *	
Pistons	Fluid temperature (initial)	Pressure
	Wall temperature (initial)	Initial mole fraction component 1
	Oven temperature	Starting stroke position *
	Cylinder length	End stroke position *
	Wall thickness	Piston offset angle *
	Heat transfer coefficient cylinder wall △	Inner cylinder radius
	Heat transfer coefficient wall-oven △	Specific heat cylinder wall
	Specific heat cylinder wall	Friction parameters (Eq.4. 20)
	Cylinder wall density	Leak parameter △
	Inlet flow resistance △	
Adsorption Column	Column length	Macropore mode
	Column radius	Micropore mode
	Void fraction of the bed △	Number of spatial grid points
	Pellet radius	Number of smaller boundary cells
	Void fraction of the pellet	Effective macropore diffusivity △
	Void fraction of the bed △	Saturation concentration, component1, site1 △
	Axial diffusion coefficient △	Equilibrium constant, component1, site1 △
	Axial thermal conductivity △	Heat of adsorption, component1, site1 △
	Pressure (initial)	Saturation concentration, component1, site2 △
	Temperature column fluid phase (initial)	Equilibrium constant, component1, site2 △
	Temperature column wall (initial)	Heat of adsorption, component1, site2 △
	Heat transfer coefficient, pellet-bed △	Saturation concentration,

		component2, site1 △
	Heat transfer coefficient, column wall △	Equilibrium constant, component2, site1 △
	Heat transfer coefficient, wall-oven △	Heat of adsorption, component2, site1 △
	Specific heat capacity at constant T solid phase	Saturation concentration, component2, site2 △
	Solid density	Equilibrium constant, component2, site2 △
	Specific heat column wall	Heat of adsorption, component2, site2 △
	Column wall density	Initial mole fraction of component1
	Column wall thickness	Initial mole fraction of component2
	The type of isotherm	With film resistance or not

Table 4.1 shows that even for a relatively simple system with only one adsorption column there are a large number of parameters that need to be either measured or determined from correlations and/or direct measurements on the DP-PSA system. This can be done effectively only by planning carefully the sequence of experiments that need to be carried out.

4.6 Conclusions

The DP-PSA system is able to characterise adsorbent materials under a large range of experimental conditions. The analysis of these experiments requires an efficient tool for the simulation of the DP-PSA system. In this chapter, a mathematical model was presented and applied to the DP-PSA system. The mass balance and energy balance of the pistons and the column were studied. The dual-site, multi-component Langmuir isotherm is applied for the mass balance of the column. The heat transfer is even more complicated. Here, the heat transfer among the adsorbent, the column, the oven and the pistons are considered. Many input variables and parameters are needed in the model, in which, 24 of them can be

determined from the DP-PSA system. For zeolite 13X, many of them are well-known parameters. The known values will be used in the simulation to establish the validity of the DP-PSA system. In the remainder of this thesis, the novel adsorbent materials will be tested in the DP-PSA system and the model parameters will be determined.

5. A Semi-automated DP-PSA system

5.1 Introduction

Besides the multitude of different process configurations a vast number of adsorbents are developed for a wide range of applications. Each of the different adsorbents is characterised by a large number of parameters, such as the adsorption isotherm and mass transfer kinetics, which have to be considered in the design of an efficient PSA process. In this chapter the DP-PSA system for the semi-automatic characterisation of adsorbent materials is presented. The flexibility of the DP-PSA process, i.e. independent control of pressure and flow rate, makes it an ideal experimental system for the characterisation of adsorbent materials.

The original mechanical design of the DP-PSA is by Professor Stefano Brandani and before the start of this work, an adsorbing columns and the pistons were already built. However, the column and the pistons were impractical, because the pistons were not able to be moved properly and small adsorbent pellets were able to get into the pipe. Additionally, the temperature in the column was not conserved. The aim of the work presented in this thesis was to build up a system, combining the existing mechanical and electronic components, which is able to test the properties of adsorbent materials by running a series of experiments automatically. To do that, a new column was designed and rock wool was applied as a safe bed in the column. Four thermocouples were designed in different locations to monitor the temperatures along the column. The movement of the pistons was a challenge because of the high frequency and high accuracy are required. It was achieved by applying the trapezoid strategy, which will be described in Chapter 6. In this chapter, first the mechanical design is described and then the operational principle will be given. Finally the experimental procedures will be discussed.

5.2 Semi-automated DP-PSA system set up

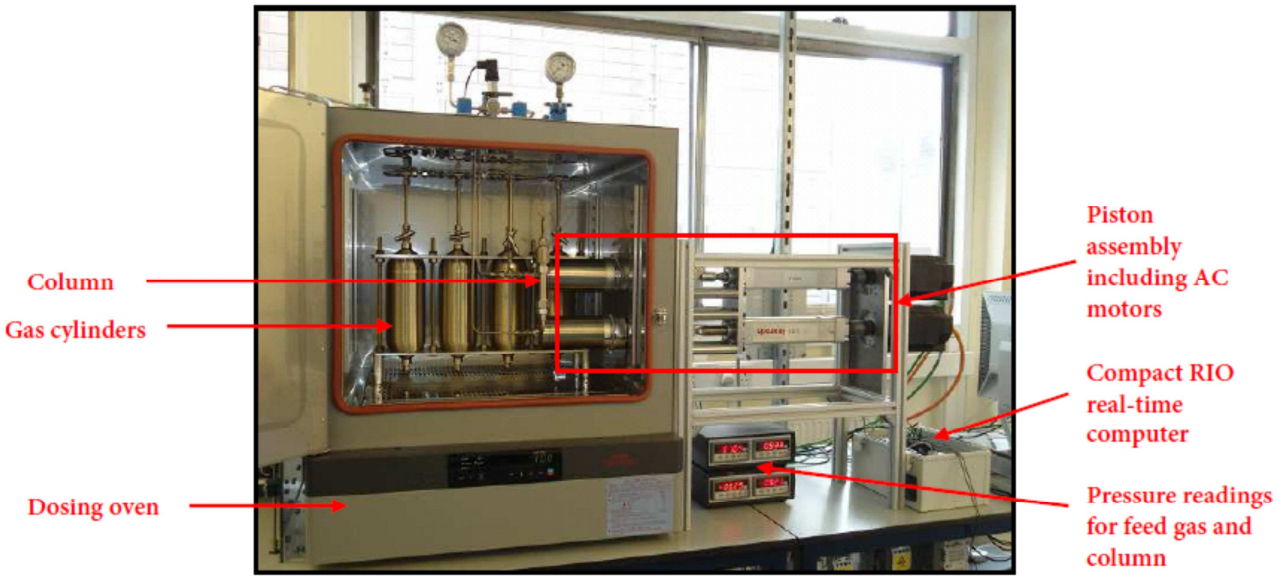

Figure 5.1 DP-PSA system

The Dual Piston-Pressure Swing Adsorption (DP-PSA) apparatus is a unique system for testing novel adsorbent materials and is being developed to be applied to the separation of carbon dioxide from a binary mixture with nitrogen. A picture of the DP-PSA system is shown in Figure 5.1 and a schematic diagram of the experimental system is shown in Figure 5.2. The main parts of the system are the two computer controlled pistons, Ps1 and Ps2, which are connected to the top and bottom of the adsorption column, AC. The auxiliary parts are the surrounding oven, the dosing system, the pressure and temperature sensors and the real-time controller. The feed side is on the left of valve V8, while the part on the right of V8 is the column side. From now on the part of the system on the right of valve V8, i.e. the adsorption column and the two pistons, are termed the column side while the part to the left of valve V8 is termed the feed side.

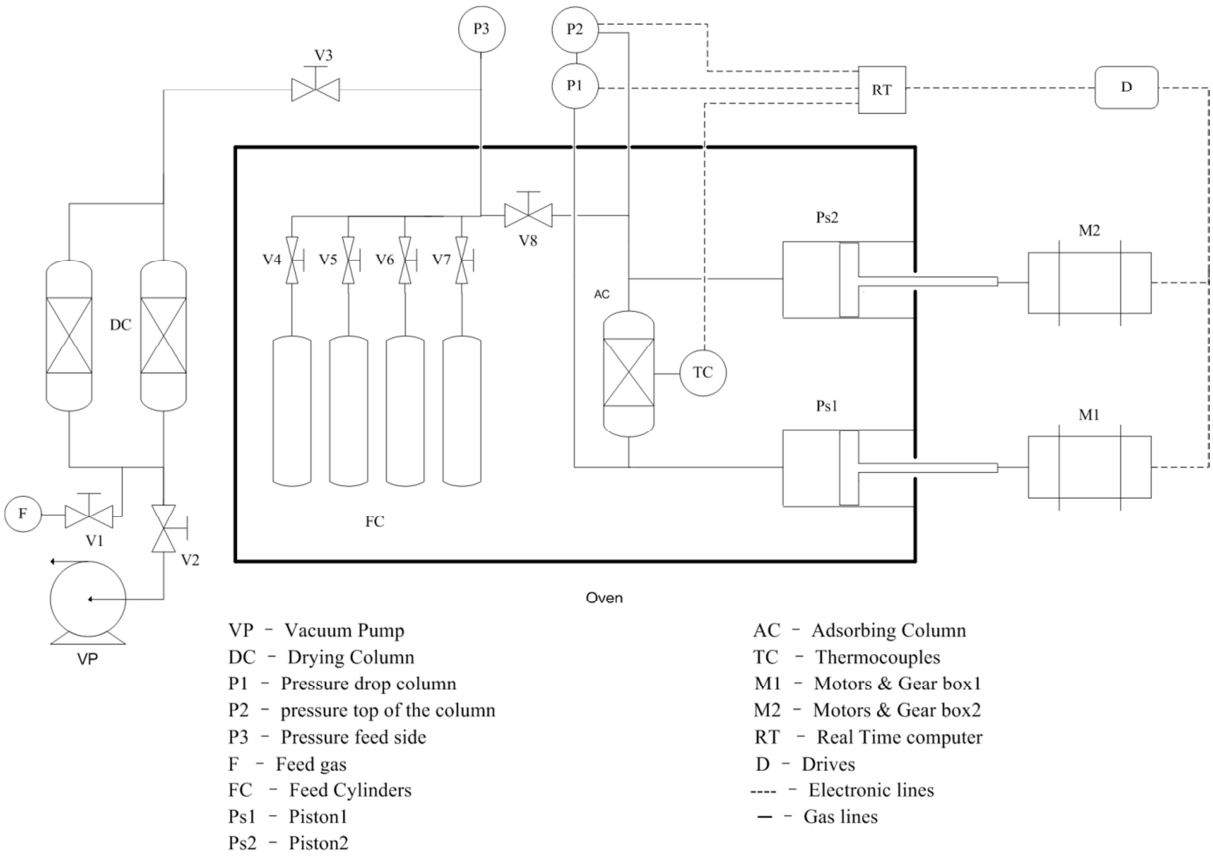

Figure 5.2 Schematic diagram of the DP-PSA system

5.3 Piston-Cylinder assembly

The two piston-cylinder assemblies, Figure.5.3, were fabricated in the university workshop to fit inside the oven. The inner diameter of the cylinders is D_c = 50 mm, while the length is L_c = 110 mm and the wall thickness is d = 12.5 mm. The seals of the piston-cylinder assembly are designed to work at pressures between 0.001 bar and 20 bar and temperature up to 260˚C; thus allowing Vacuum Swing Adsorption (VSA) and PSA experiments.

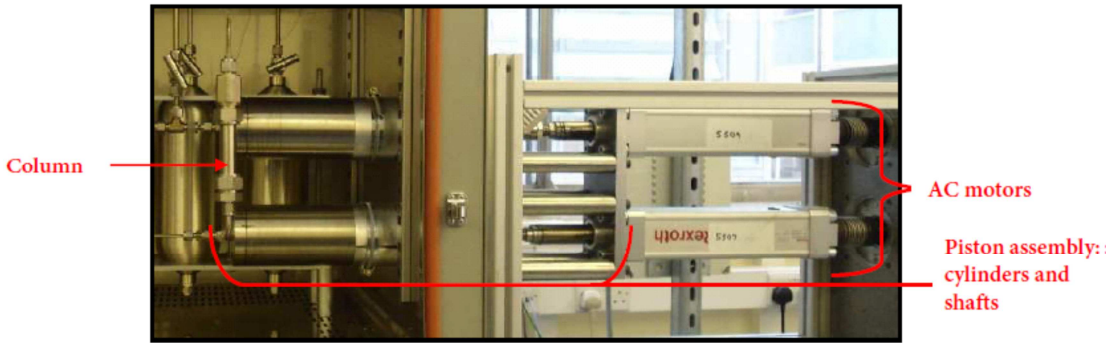

Figure 5.3 Piston-cylinder assembly with motors

The pistons can each be run at different velocities and stroke lengths. Their positions are accurately controlled and recorded and this aspect will be detailed in Chapter 6.

5.4 ABB Drives

The pistons are driven by AC (alternating current) motors through a linear motion gearbox (Bosch Rexroth AG, R156030000). The AC motors are controlled by two independent ACSM1 drives from ABB (Figure.5.4), which, in turn, are controlled through the real-time computer.

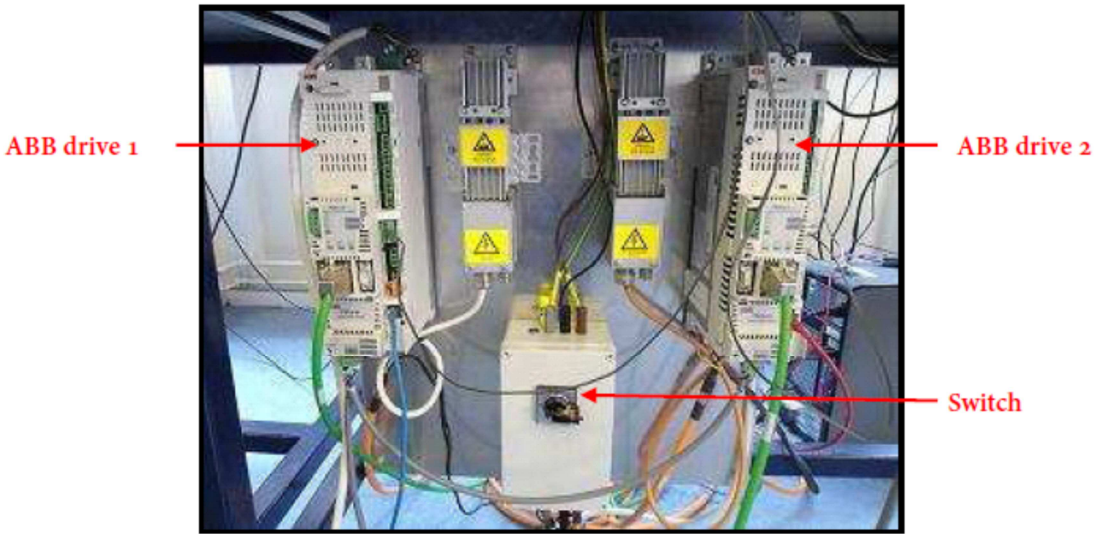

Figure 5.4 ABB Drives

In this configuration the two pistons are totally independent thus they can run cycles with different conditions (see Chapter 6). The LabVIEW interface through which the ABB drives are controlled allows the configuration for each piston-cylinder assembly of the cycle duration,

stroke length, start position, phase angle and experiment duration. The cycle duration can be set to between one second and one hour; thus allowing the user to test different time constants over 3 orders of magnitude. The cycle shapes have been designed to be sinusoidal which generates a smooth cyclic process similar to the previously reported DP-PSA systems where sinusoidal movement was achieved through rotating components but with much lower spatial accuracy (Farooq et al. 1998; Rajendran et al. 2002; Singh and Jones 1997). In the ABB system the piston movement could be programmed in principle to any shape but this has not been investigated further in the current study.

5.5 Adsorption column

The adsorption column is placed between the two piston-cylinder assemblies. The current column dimensions are reported in Table 2.1. The column side, i.e. the adsorption column and the two piston-cylinder assemblies, is separated from the feed side by valve V8.

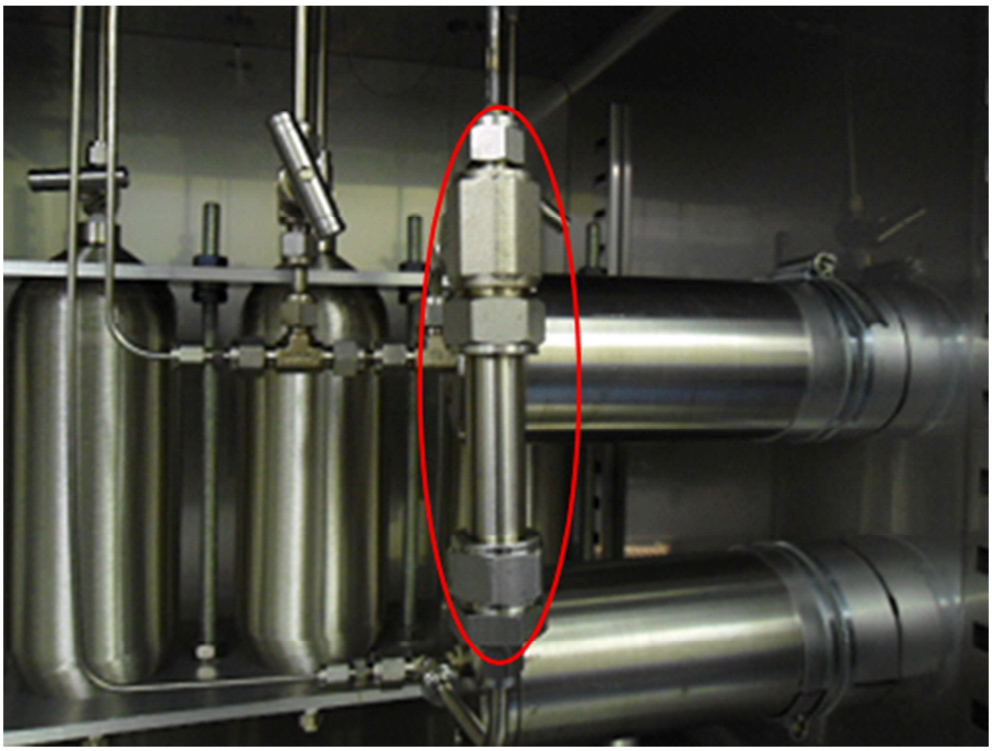

Figure 5.5 Adsorption column

Two pressure transducers, P1 (of precision 0.01mbar and range -0.5bar to 0.5bar) and P2 (of precision 0.001bar and range 0 to 3.5bar) are connected to the adsorption column. P1 is a

differential pressure transducer used to determine the pressure drop across the column and P2 measures the absolute pressure and is connected to the top piston. The lines connecting the pistons and the column in the system are made from 1/4" OD Swagelok stainless steel tubing with an inner diameter of 4.1 mm to minimise the flow resistance between the piston and the column. The lines connecting the pressure transducers are made from 1/8" OD Swagelok stainless steel tubing and the total length is 0.21 m to keep the dead volume as low as possible. Four thermocouples of type K are placed inside the column and their locations are shown in Figure 5.6. The schematic diagram can be found in Figure 4.2. The thermocouples are arranged in pairs along the length of the column. One thermocouple from each pair is inserted into an adsorbent pellet which allows the measurement of the solid temperature. The two current adsorbent pellets are zeolite 13X with diameters of 5.5 mm and 5.14 mm, respectively, and have been selected to be slightly larger than the average size in order to ensure that drilling of the hole would not be difficult and also to compensate the loss of adsorbent material, i.e. the resulting pellets with the holes where the thermocouples go are similar to the average size pellets. Another thermocouple is placed outside the column (T5 in Figure 4.2) and is fixed near the column to monitor the temperature variation in the oven.

The dual piston PSA system is designed to operate at average pressures up to 25 bar, therefore can be used to test adsorbents under conditions relevant to both post-combustion (vacuum swing) and pre-combustion capture (pressure swing). In this study the main focus has been on low pressure but an additional pressure transducer is available for the high pressure experiments and has a wider range, up to 30bar, but with a lower accuracy, 0.01bar.

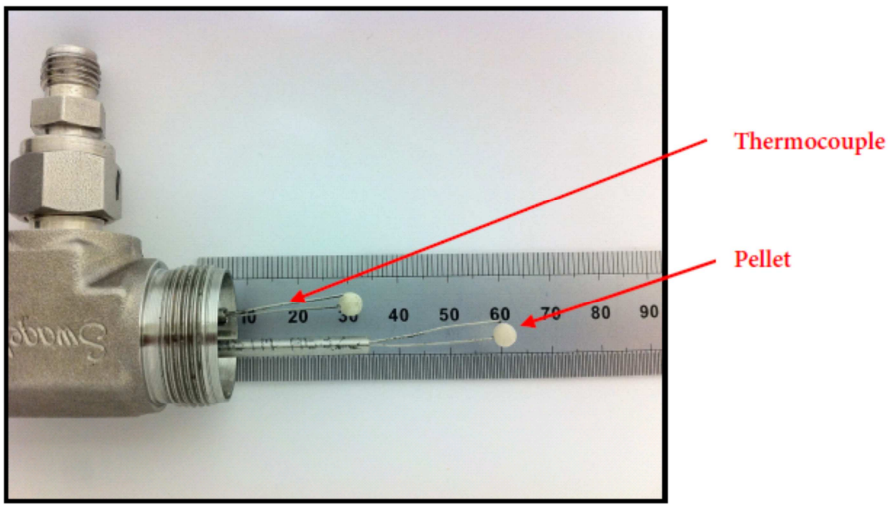

Figure 5.6 Thermocouples with 13X pellets

5.6 Oven and gas dosing system

The pistons, the adsorption column and the feed cylinders are enclosed in an oven (Sanyo MOV-112). This oven, which can reach a maximum temperature of 260 °C, ensures that all parts of the system have the same initial temperature and constant surrounding conditions. The gas lines inside the oven are separated from the gas lines outside by valve V3, see Figure 5.2.

The dosing system consists of drying columns connected to CO_2, N_2 and He lines, a vacuum pump and 4 cylinders of exactly 1 litre each. The drying columns ensure that the feed gas entering the DP-PSA system is as dry as possible. The vacuum pump is required for the evacuation of the system and is used also for the regeneration of the adsorbent, normally also setting a high temperature in the oven. The 4 cylinders which are located inside the oven are used for the preparation of feed gas. Preparing the feed gas, both single and multi component, inside the oven ensures that the option of adding a vapour in the feed is available, thus allowing for example to test in the DP-PSA unit also the effect of water. The pressure transducer, P3, is used to measure pressure in the dosing volume. By measuring the pressure before and after the gas is fed to the adsorption column and piston assembly, it is possible to determine the total number of moles in the closed system.

5.7 Drying columns

A set of drying columns is located next to the oven and these are used to remove any humidity present in the gas lines. The actual gas cylinders are located outside the building for safety reasons and water has been detected in the lines on the zero length column system that uses the same gas source.

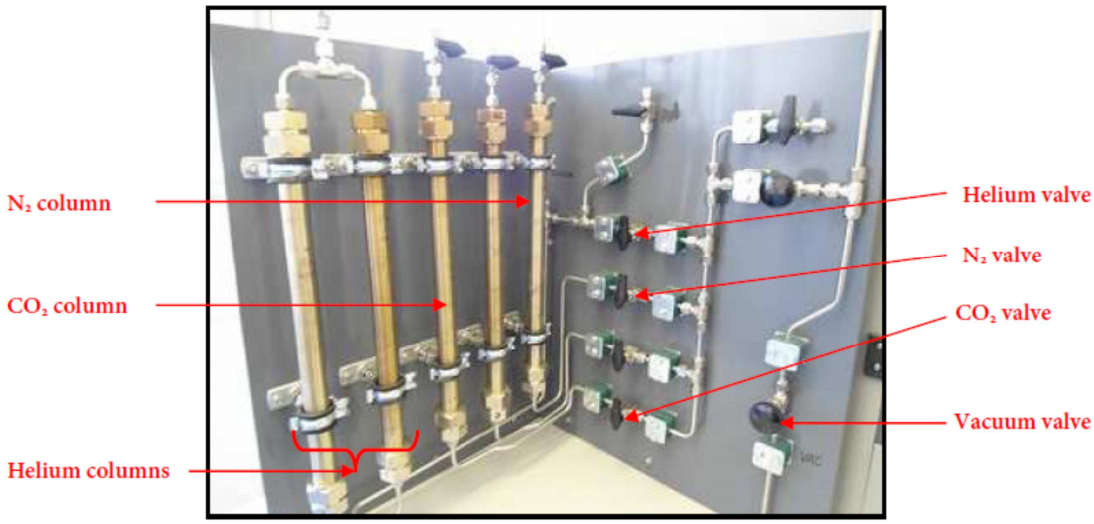

Figure 5.7 Drying columns and control valves

The columns in Figure 5.7 are packed with silica gel close to the inlet and zeolite 13X on the outlet side. They are the links between the original pure gases and the system.

5.8 Operation principle of the DP-PSA

The system can be compared to a distillation column with total reflux. The pistons perform a cyclic sinusoidal movement generating mass and energy exchange inside the system. Figure 5.8 shows a cycle with a phase angle of 0.5 π between the two pistons (one piston is ahead by ¼ cycle time) and a stroke length ratio of 2. The pistons are running at different velocities and different stroke lengths but sharing the same frequency. Figure 5.9 shows the profile of pressure and flow velocity according to the cycle shown in Figure 5.8. Moving to the right is assumed to correspond to a positive velocity and the other direction is negative. In such condition, the highest pressure occurs at around 0.58 s, when piston 1 is moving away from

the adsorbing column and piston 2 is moving towards it. Here, the system volume is at its minimum.

If a gas mixture (i.e. CO_2 and N_2) is in the system, continuous, cyclic operation of the pistons generates fluid flow and pressure variations which induce the separation of the mixture. Depending on the pistons phase angle and stroke length ratio, the strongly adsorbed component (CO_2) is collected at one end of the column while the weakly adsorbed component (N_2) is left at the other side.

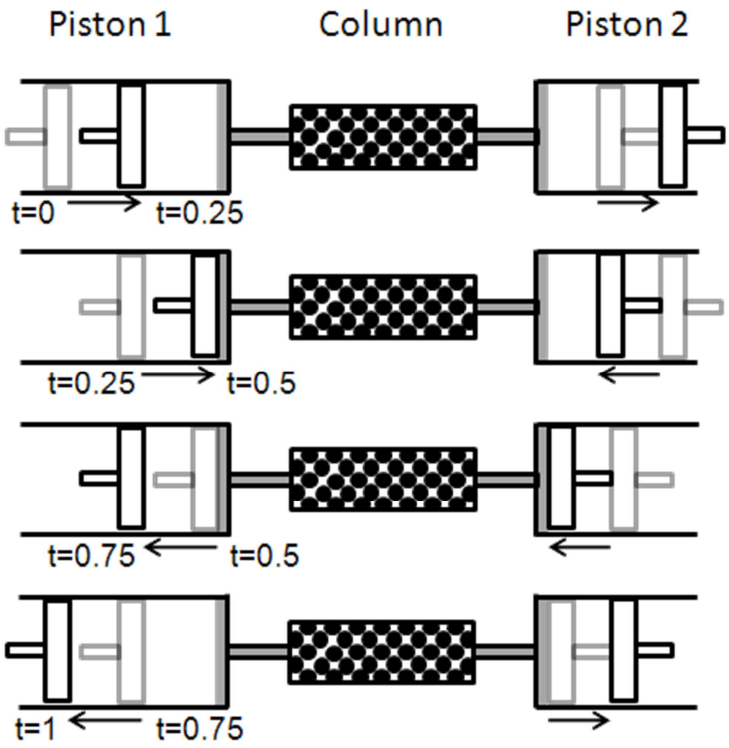

Figure 5.8 Operation of the pistons (stroke length ratio = 2, phase angle = 0.5 π)

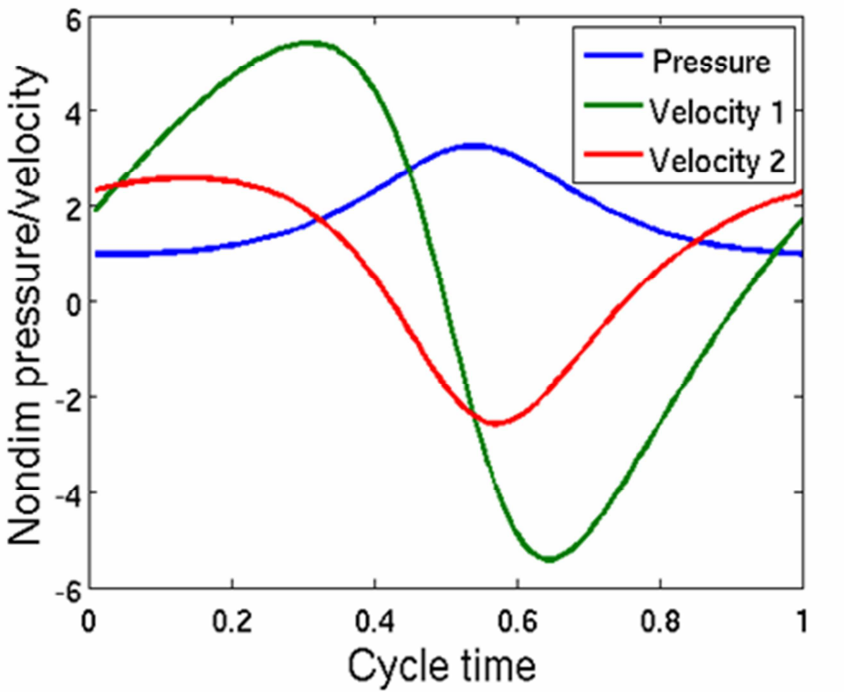

Figure 5.9 Pressure and flow velocity profile in non-adsorbing case (stroke length ratio = 2, phase angle = 0.5 π)

In the case of Figure 5.9 running with CO_2 and N_2, more CO_2 is adsorbed at the time of high pressure thus the gas phase is at a higher concentration of N_2. Because the gas is flowing to piston 1, the gas with higher concentration of N_2 goes to piston 1. Oppositely, CO_2 is released at the time of low pressure, when the gas is flowing to piston 2. So the gas with higher concentration of CO_2 goes to piston 2. If this cycle is repeated, the purity of each component at each side of the column increases up to the maximum that is obtained at cyclic steady state, where the purity, temperature and pressure performance during a cycle do not change even the cycle is repeated further.

5.9 Experimental procedure

The computer-control of the piston movement and data logging allows the semi-automated running of a series of experiments, detailed in Chapter 6. However, several steps have to be manually performed to prepare the system for a series of experiments. These steps are in the order in which they have to be performed: i) preparation of the gas mixture, ii) regeneration of the adsorbent and iii) setting of the oven temperature and feeding gas to the column.

5.9.1 Preparation of the gas mixture

The gases are prepared in the feed cylinders inside the oven and fed into the column side sequentially. To explain how to prepare a mixture, an example of the preparation of a typical mixture of 50% CO_2 and N_2, with a total pressure of 5 bar, is shown below. Note that during this process, the temperature should be kept constant. The non-ideality of the gas phase is neglected, but the correction is relatively small especially if the mixture is prepared at higher temperatures. The lines are flushed at least three times with the gas for the experiment every time before filling (for a mixture this is repeated for each gas). To reduce mixing times, it is better to feed the pure gases by a crossed sequence. The detail operations are as below.

i) Filling with N_2

a) Open the vacuum valve to evacuate the system.
b) Close the vacuum valve and refill with N_2, then empty as before. Repeat this filling and emptying procedure three times.
c) After the third vacuum evacuation, open V3 and open the cylinder valves to allow 0.5 bar of N_2 gas to flow into it. Make sure V8 is still closed.
d) Close the cylinder valve to retain the gas inside the cylinder.
e) Open the vacuum valve to evacuate the N_2 from the lines.
f) Close the vacuum valve and close V3.

ii) Filling with CO_2

a) Open the CO_2 valve for a few seconds. Then close it.
b) Open the vacuum valve to evacuate the CO_2, then close the valve.
c) Repeat this filling and emptying procedure a further two times.
d) After the third vacuum evacuation, close the vacuum valve and open V3.
e) Open the same cylinder valve as the one used for N_2.
f) Open the CO_2 valve and fill the oven cylinder with CO_2 until the pressure reading shows 3 bar, i.e. 2.5 bars of CO_2 have been added.
g) Close the cylinder valve to retain the two gases inside the cylinder.
h) Close the vacuum valve and close V3.

iii) Filling with N_2 again

It is similar to the step of filling CO_2, but to fill the cylinder with N_2 until 5 bar. So the partial pressures of CO_2 and N_2 in the cylinder are both 2.5 bar respectively. At these pressures the assumption that the gases are ideal is sufficiently accurate. If this is an issue the dosing of the gases can be carried out at a higher temperature. For high pressure experiments one would need to take into account gas phase non-ideality using an equation of state (EOS) and a standard cubic EOS should provide sufficient accuracy.

However, this is still not enough to guarantee that the gases are mixed homogeneously. The mixture gas in the cylinder should be kept overnight at high temperature (typically 200 °C) to ensure complete mixing.

5.9.2 Regeneration of the adsorbent

The adsorbent material inside the column has to be regenerated in between each experiment as well as when the column is packed or after a period of shut-down. Additionally regeneration is also carried out when a gas has been used for more than 3 days, since water may leak into the system. This will be demonstrated in Chapter 9. The regeneration consists of heating up the adsorbent zeolite 13X pellets inside the column gradually from room temperature to its regeneration temperature to ensure it is moisture-free.

a) Check first that all the valves to the system are open.
b) Switch on the vacuum pump. The gases are emitted from the base of the pump into the ventilated lab. Evacuation can take from 30 minutes to an hour.
c) Open the vacuum valve slowly and the other valves in the oven gradually to allow all the gases to flow out from the oven. Caution: Opening the valve too fast could damage the pump.
d) Monitor the digital pressure reading in the top right panel of the meter (for 0 to 3.5 bar) for up to 10 minutes to confirm no leakage in the system. The reading is sensitive to 0.001 bar.
e) Set the oven temperature to the regeneration temperature of 200 ˚C.
f) Leave the vacuum pump on for the whole regeneration time.

g) After regenerating for 12 hours, fresh gas is fed to the system.

5.9.3 Gas feed

After preparing the gas mixture and regenerating the adsorbent, the gas is fed into the column side. The oven is allowed to cool to the experimental temperature. Meanwhile, the two pistons are moved in a slow cycle (T_c = 60 s) and out-of-phase. This ensures that the piston-cylinder assembly is at a uniform temperature and minimises leaks while keeping the volume in the system constant. The procedure for the gas feed is as follows:

a) Make sure all of the valves are closed;
b) With the vacuum pump running, open valve V3 to evacuate the piping on the feed side;
c) Close valve V3;
d) Open one feed cylinder valve and record the pressure, P_b (b = reading before entering the column), on the feed side of the system with the pressure transducer P3;
e) Valve V8 is opened to feed the gas mixture into the column side of the system and closed very quickly otherwise the composition in a mixture may have a large uncertainty due to uneven adsorption of the components inside the column.
f) The pressure, P_a (a = the reading after entering the column), at the feed side allows the calculation of the number of gas molecules that are in the system assuming ideal gas behaviour:

$$n = \frac{(P_a - P_b) \times V}{R \times T} \qquad \text{Eq.5.1}$$

Where, V is the dosing system volume, i.e. feed cylinder plus piping between V3 and V8.

Once the system reaches the set temperature and is stable, which can be monitored through the thermocouples inside the column, the series of experiments is started. Since the oven is not controlled through the LabVIEW interface each series of experiments is run at a single temperature. The parameters of the experiments are passed to the real-time computer which runs the experiments in a sequential way. Between individual experiments the pistons are kept moving with the same cycle duration of the previous cycle but with the pistons in the

out-of-phase configuration, i.e. no change in total volume. The experiments are usually run with increasing frequencies, i.e. progressively shorter cycle times. This reduces the influence of friction heating between experiments, as this effect is greater for shorter cycle times, i.e. the average temperature increases in the sequence.

5.9.4 Calculation of the initial gas and solid phase concentrations

To initialise the simulations, the total gas fed to the column has to be converted to a gas and solid phase concentration. Both the gas and solid phases of each gas in the mixture can be calculated assuming equilibrium.

By comparing the pressure of the dosing cylinders before and after feeding the gas to the adsorbing column, the total amount of gases, $n_{total\_1} + n_{total\_2}$, can be easily determined. Since the system is flushed from vacuum to high pressure in a very short space of time, we can assume that the ratio of the gases stays the same as the feed composition.

Considering the adsorption in the column, the total mass balance equation is given by

$$n_{total\_1} + n_{total\_2} = \frac{P_{col} \times V_{GAS}}{R \times T} + q_1 \times V_{sol} + q_2 \times V_{sol} \qquad \text{Eq.5.2}$$

and the single component mass balances are given by

$$n_{total\_1} = x_1 \frac{P_{col} \times V_{GAS}}{R \times T} + q_1 \times V_{sol} \qquad \text{Eq.5.3}$$

$$n_{total\_2} = x_2 \frac{P_{col} \times V_{GAS}}{R \times T} + q_2 \times V_{sol} \qquad \text{Eq.5.4}$$

where,

$$x_1 = \frac{n_{gas1}}{n_{gas1} + n_{gas2}} \qquad \text{Eq.5.5}$$

$$x_2 = 1 - x_1 \qquad \text{Eq.5.6}$$

$$q_1 = q_s{}^1 \times \frac{x_1 \times P_{col} \times b_1{}^1}{1 + (b_1{}^1 \times x_1 + b_2{}^1 \times x_2) \times P_{col}} + q_s{}^2 \times \frac{x_1 \times P_{col} \times b_1{}^2}{1 + (b_1{}^2 \times x_1 + b_2{}^2 \times x_2) \times P_{col}} \quad \text{Eq.5.7}$$

$$q_2 = q_s{}^1 \times \frac{x_2 \times P_{col} \times b_2{}^1}{1 + (b_1{}^1 \times x_1 + b_2{}^1 \times x_2) \times P_{col}} + q_s{}^2 \times \frac{x_2 \times P_{col} \times b_2{}^2}{1 + (b_1{}^2 \times x_1 + b_2{}^2 \times x_2) \times P_{col}} \quad \text{Eq.5.8}$$

In the gas phase, n_{gas1} and n_{gas2} should obey the ideal gas law.

$$n_{gas1} + n_{gas2} = \frac{P_{col} \times V_{GAS}}{R \times T} \quad \text{Eq.5.9}$$

By solving equations 5.2 to 5.9, it is possible to quantify the state of the gases (mole fraction of each component) in the system under equilibrium.

5.10 Conclusions

The DP-PSA system was fully described in this chapter. Compared to the conventional PSA, it is more flexible and robust. It is a closed system where pistons moving in cylinders at each end of the adsorbent column induce the cycling of fluid flows and pressure variations in the fixed bed. As it is a closed system, samples can be tested repeatedly under different conditions with minimal consumption of gas. Since only a relatively small amount of solid material (a few grams) is needed for the experiments, rapid testing of novel adsorbent materials can be undertaken. The most important function is that the materials' characteristics, including kinetic and equilibrium properties, can be determined. Moreover, The DP-PSA's analog communication system enables very fast cycle times to be run, ranging from 1.5 Hz up to cycles that last for several minutes. The accurately controlled pistons are designed independently, so their movement are flexible. It allows the DP-PSA to run a wide range of operating conditions varying:

a. cycle speed (maximum speed is 1.5 cycles in 1 second for a stroke length of 100 mm)
b. phase angle
c. piston stroke lengths , i.e. either small or large pressure variations.

A real time computer is applied for the pistons' control and data logging. The automation of the experiments is facilitated by LabVIEW. The automation of the DP-PSA system will be described in detail in Chapter 6.

6. DP-PSA Automation

To run a series of experiments with the DP-PSA with minimum attention from the user, LabVIEW (Laboratory Virtual Instrument Engineering Workbench) , a software from National Instruments (NI) that provides a system-design platform and development environment for a visual programming language (NI 2013), was used to develop a user interface to automate the system.

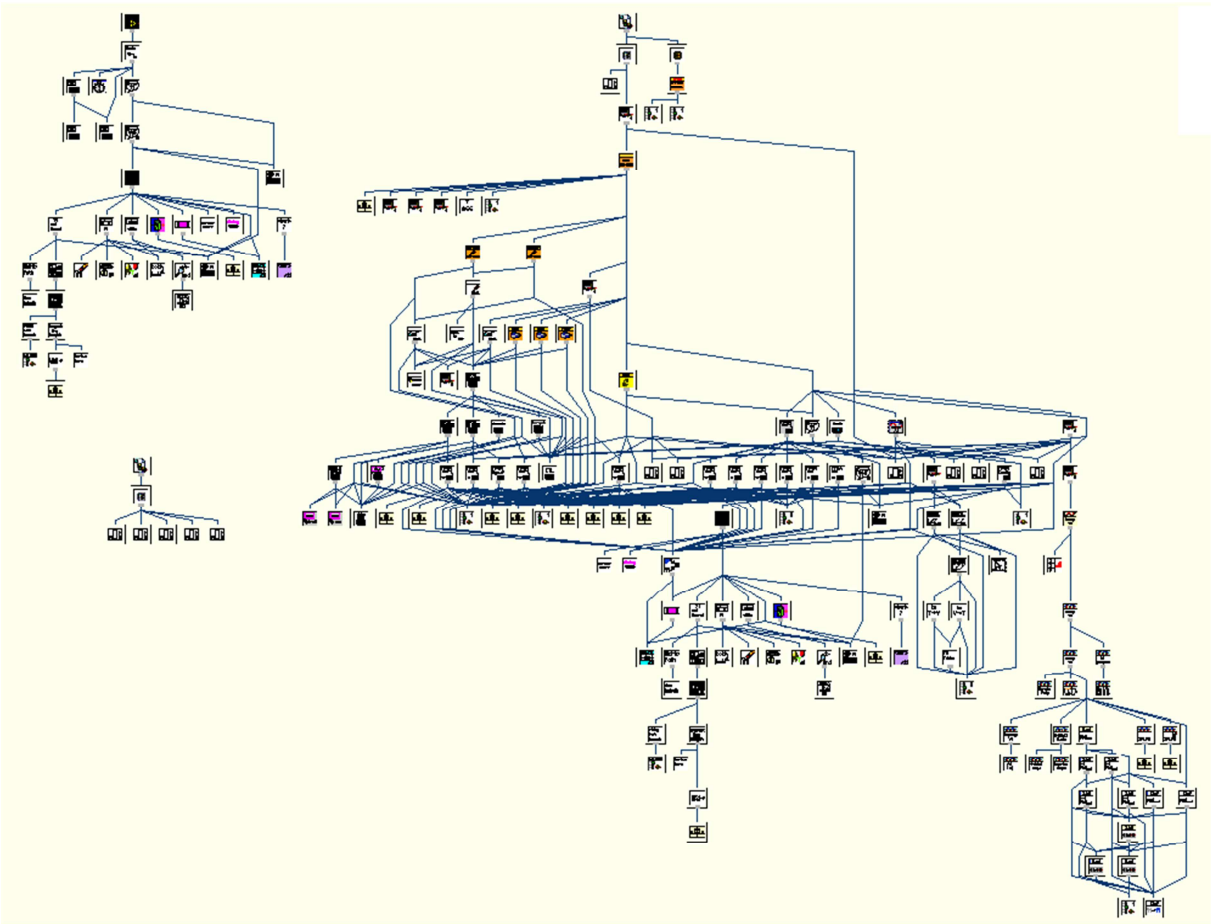

Figure 6.1 An overview of the VI hierarchy and its complexity

The whole DP-PSA automation task has been divided into many small tasks. In the LabVIEW code, each small task is represented by a program/subroutine which is called a Virtual Instrument (VI). An overview of the VI hierarchy can be found in Figure 6.1, which shows

the complexity of the overall automation system. In the VI hierarchy, each block stands for a VI and the lines show the connections between lower level VIs and upper level VIs.

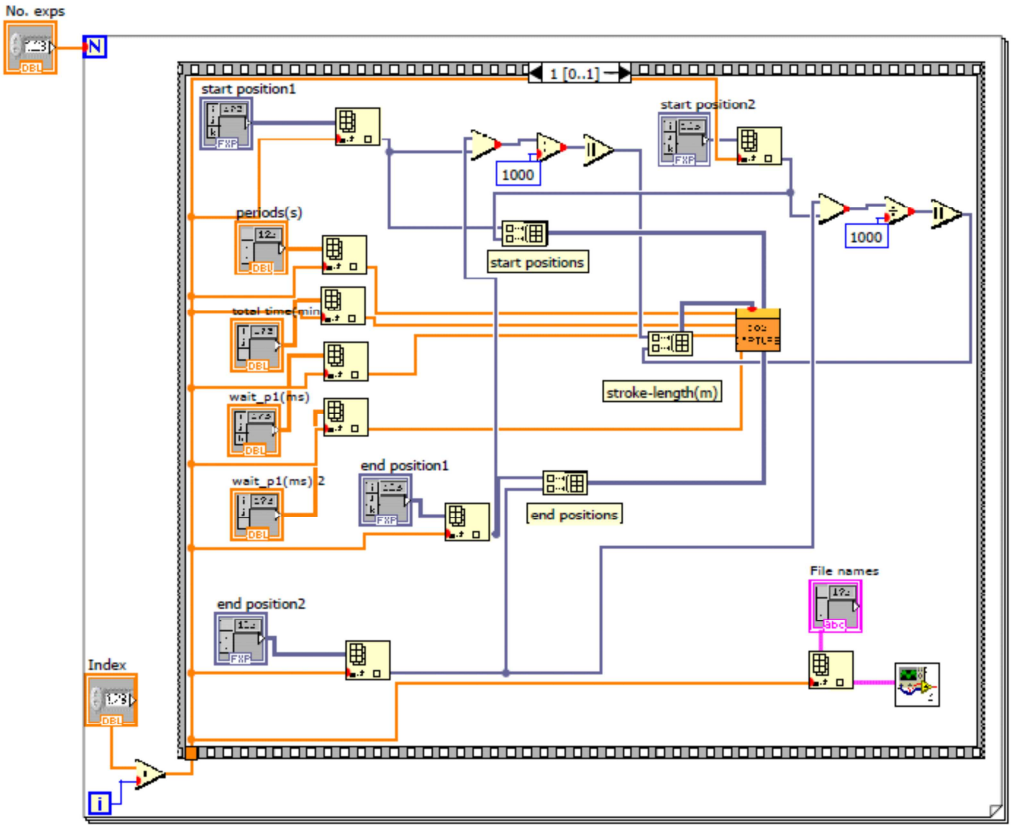

Figure 6.2 An example of the block diagram of a VI

Figure 6.2 shows an example of the block diagram of a VI. There are a total of 191 VIs involved in the final version of the LabVIEW code for the DP-PSA system. Of these 68 VIs are written specifically for this task and are mainly top level VIs. The other VIs are from the libraries provided by the software with only minor modifications needed in some cases. To achieve the correct implementation of the code several training courses and discussions with the technical support from NI and ABB, and the electronics workshop technicians were particularly useful in order to have an overview of the best approaches for a specific sub-task.

This section describes briefly each sub-task of the automation system with the aim of giving a brief logic for the coding strategies.

6.1 Control instrumentations

A Compact RIO 9022 real-time computer, RT, from NI is employed to facilitate accurate control of the piston movement and high frequency data logging. Specific modules from NI are connected to the Compact RIO as peripherals. The motor drives from ABB and pressure transducers from GE are directly controlled by these modules. In the development phase the Compact RIO can operate also with a link to a PC and transfer data continuously. This will slow down the speed of execution, but allows the user to monitor the system and take corrective action. This function can also be used once the code is developed to check the variables that are not normally included in the data log, i.e. the piston and motor information from the ABB drives.

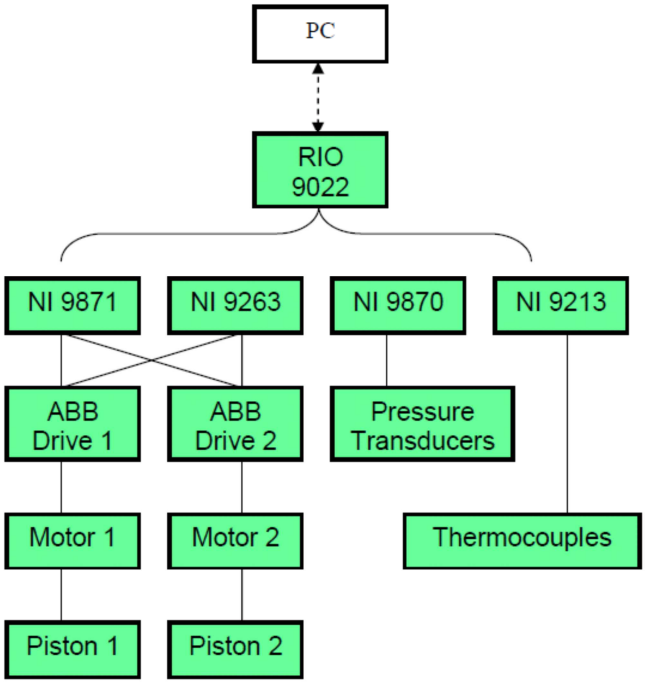

Figure 6.3 Schematic diagram of pistons control system

The main challenge is the accurate control of the pistons. Figure 6.3 shows the schematic diagram of the pistons control system and Figure 6.4 shows the picture of the Compact RIO, including the four modules.

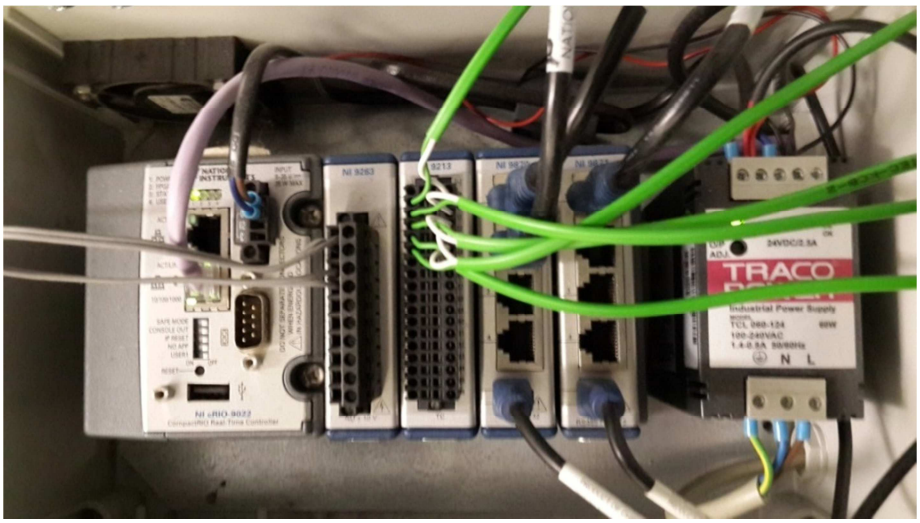

Figure 6.4 Compact RIO with the modules

The ABB drive directly controls the working conditions of the pistons and the LabVIEW interface is used to change the settings of the control parameters and acquire several status indicators. The real-time computer is employed to facilitate accurate control of the piston movement and high frequency data logging. The Compact RIO was housed in a chassis, NI9113, which provides Xilinx Virtex-5 RIO (reconfigurable I/O) FPGA (Field-Programmable Gate Array) core. NI9113 is able to automatically synthesise custom control and signal processing circuitry on FPGAs using LabVIEW. The real-time computer communicates with the ABB drives through 2 different NI modules: a serial interface module, NI9871, is used to configure the drive at the start of the experimental run, i.e. setting the speed, acceleration and deceleration of the motor, and to record the actual piston position during the experiment and other status indicators such as the power in the electrical motors; an analog output module, NI9263, is used to control the direction of movement of the pistons during the experiment. The use of an analog module is required for the control of fast cycles, i.e. cycle durations below ~10 s, due to the high latency in the serial interface module. The pressures are recorded through a serial interface module, NI9870, and the temperatures from the five thermocouples are recorded through a thermocouple input module, NI9213.

6.2 LabVIEW Operator interface

The operator interface refers to the LabVIEW front panel on the development PC, before the program runs on the Compact RIO. For the convenience of the user, the operator interface just

includes all the key condition variables related to the experiment. A screenshot of the interface is shown in Figure 6.5.

Figure 6.5 Operator interface

There are 10 columns relating to the 10 parameters for each experiment. They are labelled as below.

- Index – Label the sequence of experiments
- File names – Name the output text file of the experimental data
- periods(s) – Sets the cycle time of the piston, in seconds
- total time (min) – Total running time of the experiment, in minutes
- wait_p1(ms), wait_p2(ms) – By setting the wait time of each piston, the phase angle between pistons is set in milliseconds
- start position1, start position2 – The minimum positions during the stroke
- end position1, end position2 – The maximum positions during the stroke

Each row defines one experiment. If the default number of experiments is not enough, the user can increase the number by a dragging of the mouse movement and the column number increases accordingly.

On the top of the screen the general conditions for a series of experiments are listed as below,

- No. exps – How many experiments in this series.
- Index – Which experiment is the first to be run.
- Initial position P1/P2 – What are the initial positions for both pistons before the experiment.
- Wait after each exp – Waiting time (in minutes) from the end of one experiment to the beginning of the following one.

Once all of the relative parameters are set, the user has to save them as the default parameters. This ensures that when the code is transferred and executed in the Compact RIO the correct settings are used. The whole code and the new set of parameters are built as an independent program. This program is triggered by restarting the Compact RIO once it is uploaded, but this requires up to 2 minutes to execute.

Once the series of experiments is finished, the data files can be transferred from the Compact RIO to the PC through the Measurement & Automation software. The output data is aligned in 10 columns:

1) Time, in seconds;
2) Position of piston 2, in mm;
3) Position of piston 1, in mm;
4) Absolute pressure of the system, in bar;
5) The pressure drop across the adsorbing column, in mbar;
6) –9) Temperatures inside the column (see picture 4.7), in ˚C;
10) Temperature of the oven, in ˚C.

6.3 Piston movement and cycle shape

The piston movement is not inherently sinusoidal but can take in principle almost any shape. However, to facilitate the analysis of the results it is better to approximate a sinusoidal cycle

shape so that there is only one main frequency for each experiment. This cycle produces a smooth change of the pressure and flow velocities in the system and allows the comparison with previously reported results (Farooq et al. 1998; Rajendran et al. 2002; Suzuki et al. 1996).

In order to allow accurate positioning of the pistons for fast cycles a control scheme combining digital and analog communications is used. Because of the latency in the digital communications it was found that a single half-cycle instruction was the best way to operate the system when compared to breaking down the movement into a number of sections. The movement in a half-cycle is approximated using a trapezoid velocity strategy, shown in Figure 6.6, by which the acceleration, deceleration and maximum speed of each piston are set for the chosen cycle configuration and transferred via a serial link to the ABB drives, at the start of each experiment. Speed, acceleration and deceleration can be derived from the configuration of the sinusoidal cycle for each piston, i.e. stroke length and cycle time. Since the pistons are independent, different speeds for two pistons are possible.

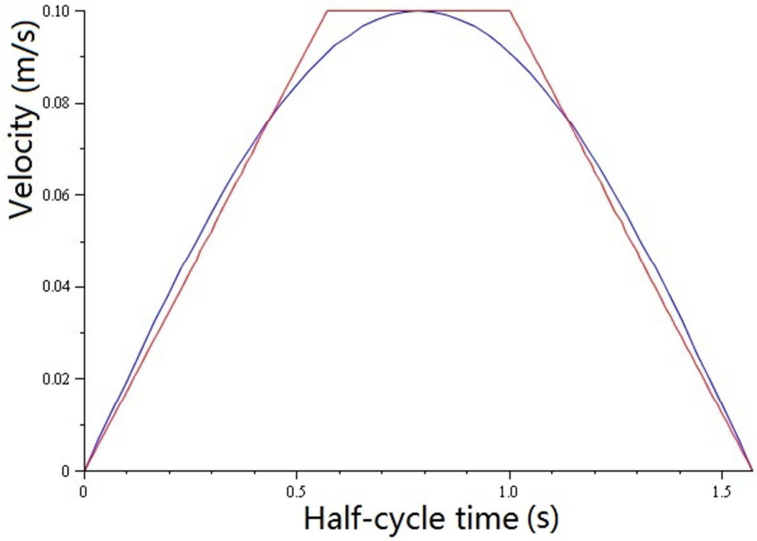

Figure 6.6 Trapezoid to sine profile

The trapezoid profile is directly calculated from cycle conditions and there are 6 parameters in total that can be modified: the acceleration; the maximum speed; the deceleration; and the corresponding times of these movements. In practice though there are several constraints: symmetry imposes that both acceleration and deceleration have equal absolute values and

durations (2 equations); the integral of the velocity over a half-cycle must equal the stroke length; the total time of the three movements is equal to the half-cycle time; the initial acceleration times its duration is equal to the maximum speed to ensure continuity. With these constraints there is only one degree of freedom and the constant speed is selected to be the same as the maximum speed of the sinusoidal wave as this minimises the mean square error in the area (i.e. position) and satisfies the condition below,

$$\int_0^T (A_{\sin}(t) - A_{tra}(t))^2 \, dt = \min \qquad \text{Eq. 6.1}$$

From the parameters set by the user and the constraints set above the initial acceleration is calculated from

$$Acceleration = \pi^2 \frac{Strokelength}{2T^2(\pi - 2)} \qquad \text{Eq. 6.2}$$

$$Maxspeed = \pi \frac{Strokelength}{2T} \qquad \text{Eq. 6.3}$$

Where T is the half-cycle time. Figure 6.7 shows the comparison of the ideal sinusoidal cycle vs the positions calculated from the trapezoid velocity profile. Figure 6.8 shows the comparison of the actual position of the piston obtained in representative cycles and that of the ideal sinusoidal cycle, confirming that for the analysis of the results a simple sinusoidal forcing function can be used. The RMS (Root-Mean-Square) error between the calculated piston position and the actual, measured piston position over one cycle is within 1% of the stroke length for a wide range of conditions (over 10 different experimental cycle times and/or stroke lengths).

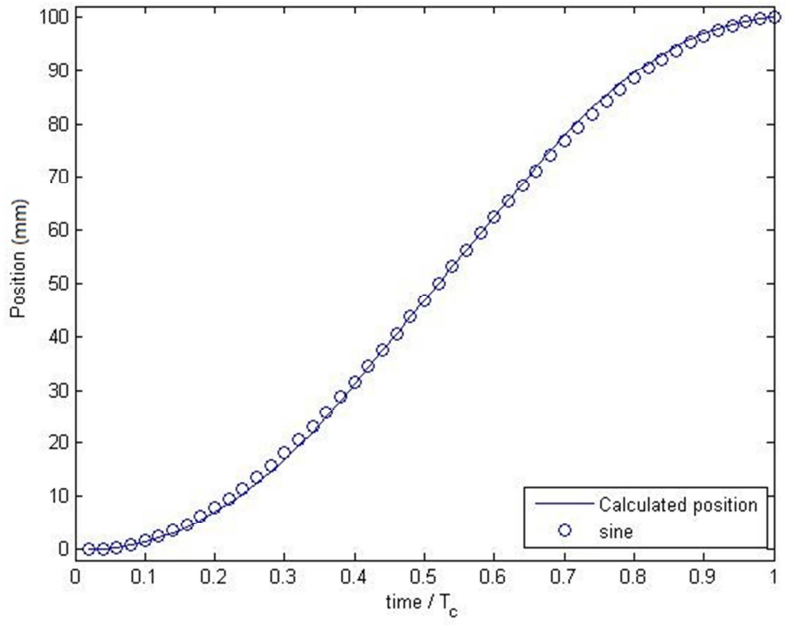

Figure 6.7 Comparison of calculated piston position from the trapezoid velocity strategy and the standard sine

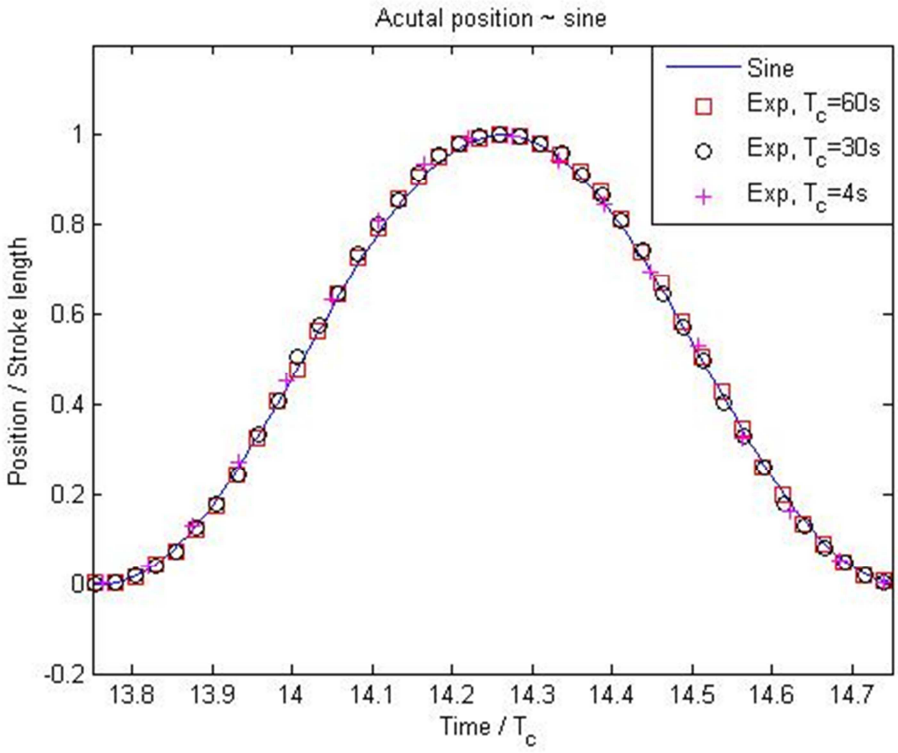

Figure 6.8 Comparison of actual piston position and standard sine

6.4 LabVIEW Software Design overview

As mentioned before, to increase the communication and calculation efficiency, an FPGA was applied between the real time computer and functional modules. Hence, the programming code generally consists of an FPGA configuration and processing control.

6.4.1 FPGA configuration

The code for an FPGA configuration was programmed as a parallel structure for each function. In this way all the information i.e. pressures, temperatures and piston positions can be read with minimum delay. This was found to be critical when aiming to achieve cycle times of 1 second or less.

The FPGA coding structures are mainly for communication. They include sending a command to the target, receiving data, error processing, etc. There are 5 parallel functional structures.

- Reading all temperatures via Module NI9213;
- Communication with pressure display box for absolute pressure via Module NI9870 port 1;
- Communication with pressure display box for differential pressure via Module NI9870 port 2;
- General communication with ABB drives, i.e. position data reading via Module NI9871;
- Sending the position reference command via Module NI9263 to the ABB drives during the experiments

In 4 of the total 5 functional structures, there is a labelled IRQ (Interrupt ReQuest) for each of them. When a function is activated, it sends an interrupt request to ask the CPU to stop its current job and turn to the new request. However, too many IRQ settings may interrupt the work of the CPU too frequently and the work of the CPU at that moment is then delayed. So it is beneficial to reduce the number of IRQs by identifying a priority ranking. The highest priority is given to the piston control, i.e. the piston direction analog signal. Absolute pressure

and relative pressure follow in the priority order. The lowest priority is for the general communication. As discussed below no IRQ is set for the temperature read, therefore this does not appear in the priority list.

a)

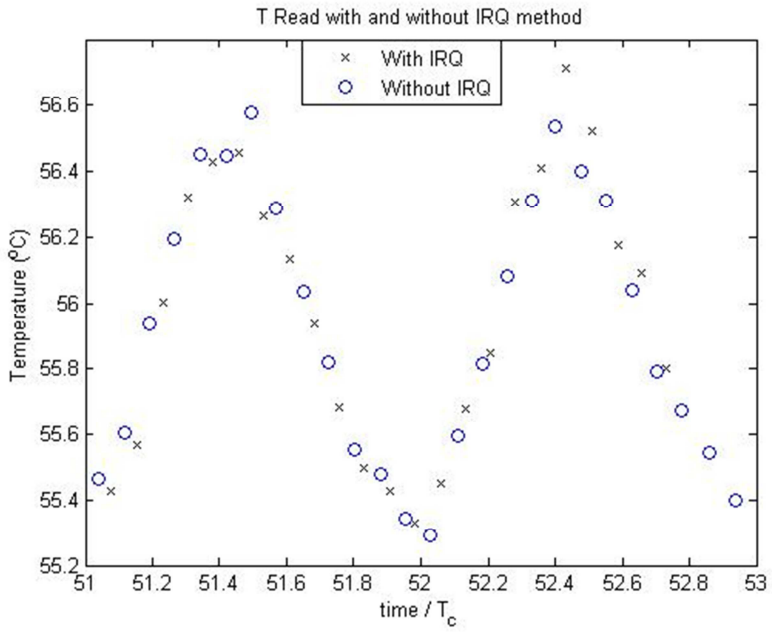

b)

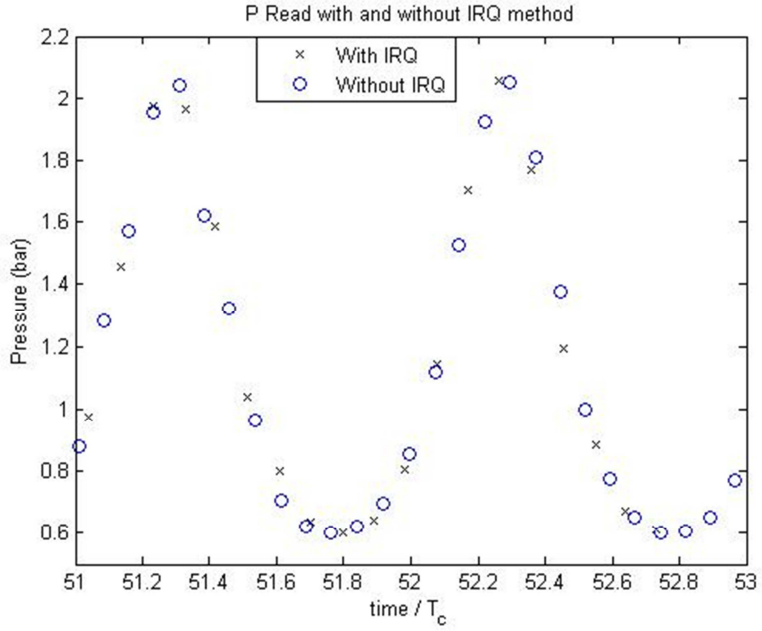

Figure 6.9 Comparison of the temperature (a) and pressure (b) data acquisition frequencies between the tests reading temperature with IRQ and without IRQ

Some tests have been carried out to establish the effect of different IRQs on the data acquisition rate. In each test, one of the labelled IRQs is replaced and the experiment is run. In the test of Figure 6.9, the pistons were run in high frequency, T_c=1s. By comparing their effects, it was found that the IRQ method actually did not effectively increase the temperature data acquisition frequency but it slowed down the pressure data acquisition. Considering that the temperature data acquisition frequency provided enough detail for the fitting, the IRQ method is not applied to the temperature reading.

Table 6.1 IRQ labels for the functional structures in FPGA configuration

Structure function	General communication	Absolute pressure	Differential pressure	Sending position reference commands
IRQ labels	IRQ 1	IRQ 2	IRQ 3	IRQ 4

Every IRQ used in the structures is labelled differently as this avoids the conflict that different structures call one IRQ at the same time. Their labels are listed in Table 6.1.

Two FIFO (First in, First out) buffer channels are used to improve the data transfer efficiency. The FIFO data exchange policy creates a data buffer with a customised size, in which data is removed after it is read. If the FIFO is full (at the maximum depth), it is not possible to write additional data until some data is read. Read operations create space in the buffer as they remove the data they read. To minimise CPU access, a DMA (Direct Memory Access) method is applied to access the data in the FIFO. This allows transferring data between an FPGA target and the host computer and does not involve the host processor. Therefore, it is the fastest available method for transferring large amounts of data between the FPGA target and the host and does not affect the running and data acquisition rates. By this method, FPGA resources will be saved when transferring large amounts of data. It also frees the host processor to perform other calculations during data transfer and automatically synchronises data transfers between the host and the FPGA target. The NI Scan Engine enables efficient single point access to sets of data channels, such as I/O channels, using a scan that stores data in a global memory map and updates all values at a single rate, known as the scan period (NI

2011). The scan engine used here needs 2 DMA channels to transfer data from the Compact RIO to the FPGA and vice versa (read and write).

6.4.2 Processing control

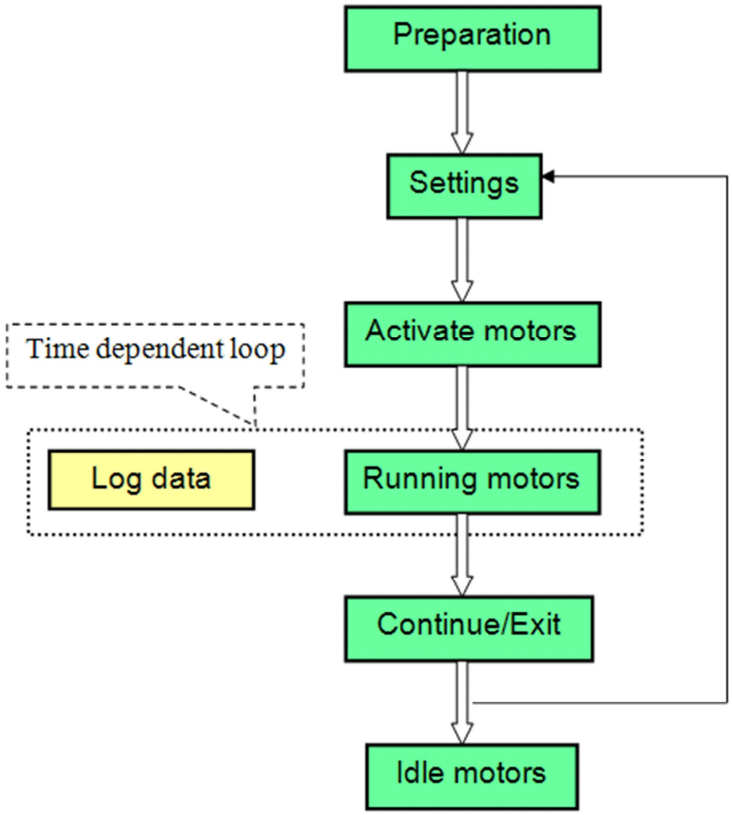

Figure 6.10 Flowchart of LabVIEW programme running an experiment

In order to minimise the interaction among the control project and optimise control operations, the strategy of using state machines is applied. A state machine implements any algorithm described by a "Moore machine," which performs a specific action for each state in the diagram (NI 2013). The code for different functions is modularised in the processing control code. It consists of seven modular code blocks which are shown in Figure 6.10. In the preparation state machine at the start of the program the parameters of the motor, i.e. position and velocity reference, are set to safe default values. Based on the user's cycle configuration parameters, the acceleration, deceleration and speed settings of the motors are calculated and transferred via a serial link to the ABB drives. Then the motors are activated and the pistons

are moved to their initial positions. Once the pistons are in the starting positions the set cycle is run for the specified runtime. During the running of the experiment, the actual piston positions, two pressures and the five temperatures are read continuously with a fixed frequency and written to the log files. Once the runtime for this experiment is reached, the code identifies if there is still an experiment in the queue. If there is a further experiment the code moves to the next set of experimental parameters and goes back to the Settings module. Otherwise, the pistons are moved to the initial safe conditions and the motors are set to idle.

6.4.2.1 Preparation of the motors

The FPGA reference is called and will go through all the control procedures. The Compact RIO communicates with the ABB drive by Modbus. The serial port is configured as follows:

Band Rate: 115.2bps
Parity: Even
Data Bits: 8
Stop Bits: 1

According to Firmware Manual ACSM1 Motion Control Program (ABB Oy 2008), to reset the motor, the command given to the ABB drive is formed in 32 bits.

When a broadcast request is sent on the serial bus, in case no response is returned from the slaves (ABB drives) immediately, there is a delay by the master (Compact RIO) in order to allow any slave to process the current request before sending a new one. This delay is called "Turnaround delay". Therefore the master goes into "Waiting Turnaround delay" state before going back to the "idle" state and before being able to send another request. Typically the Turnaround delay is between 100 ms and 200ms. Within the Turnaround delay, if the communication is successfully established, the ABB drives begin to accept the settings of the motors, otherwise, an error is returned.

6.4.2.2 Settings of the motors

The settings for the two motors are totally independent. Once the initial and full stroke positions of the two pistons are set, the code can construct a piston cycle shape. The ABB

drive will accept an instruction that fixes the acceleration, maximum speed and deceleration and calculate the associated length of time for the movements. Therefore different cycle shapes can be achieved in principle by deconstructing the position vs time plot into subsections and matching the desired shape into the instructions that the ABB drive will accept. To avoid time delays between different sections, it is preferable though to achieve a full half-cycle with a single instruction. A sinusoidal movement can be effectively approximated via a single instruction through an optimal choice of the acceleration/deceleration times and duration of the maximum speed and as discussed in section 6.3.

The parameters in the ABB drives are initialised via the RS485 link at the beginning of the experiment and each half cycle is pre-programmed.

6.4.2.3 Activate and stop motors

After all the settings are given, the motors can be activated by sending a 32 bits command. Once the drives receive this command, the pistons will be driven by the motors to move to the initial position and hold until all is set to initiate a sequence. To ensure that the correct initial condition and state of parameters is achieved, this state machine includes a wait stamp. The default piston movement to the initial position is set as a total time of 30 s with a close to sinusoidal movement.

To activate all data acquisition and control functions a global Boolean variable is used and switches on the simultaneously running programs, such as data logging. This is set to false when the motor is active and the piston has reached the starting position.

After the experiment, the motors need to be released. At this point the global boolean variable is set to true and this stops all the functions that are still running.

If the user requires the flexibility of running experiments one by one, then it may become cumbersome to re-initialise the Compact RIO each time. Therefore the LabVIEW interface allows to run the PC connected to the Compact RIO and in this case in between experiments the motors are held in a loop and keep the state until the user makes the decision of which

experiment to run next. This is sometimes necessary to establish the range of experimental conditions that will then be explored in the automatic mode.

6.4.2.4 Running motors

There are four blocks of functions listed in Figure 6.11 running simultaneously in this state machine. The FPGA reference goes to each of them, but only one goes from the piston control function and connects to the function in the next state machine. By this arrangement, it allows all of the functions in the blocks to be governed by an FPGA but only one FPGA reference goes to the next state machine and this avoids an FPGA reference conflict in the next state machine.

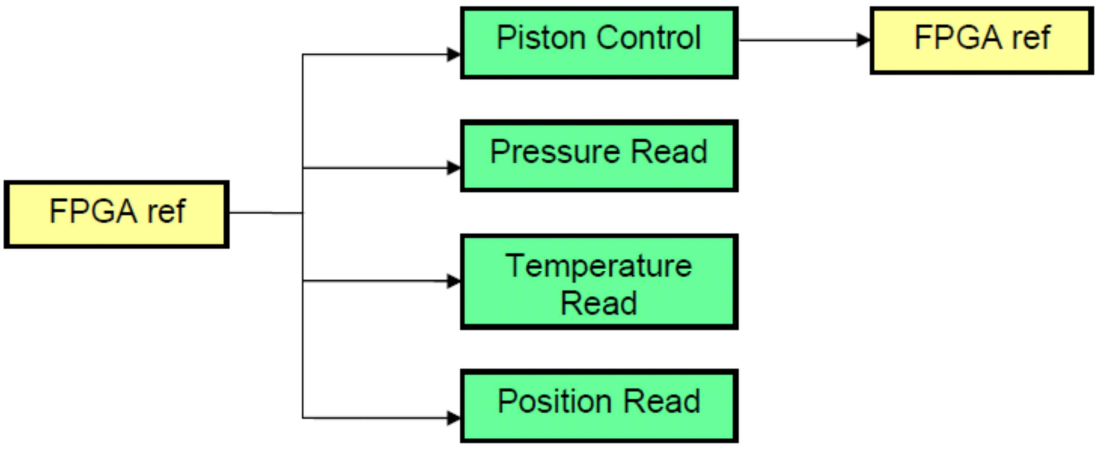

Figure 6.11 Function blocks during experiment

Piston Control

Initially the system operated a digital output to control the ABB drives. This generated a delay between the intended position and the actual position of the pistons when the Compact RIO was sending the instruction to reverse the direction of movement. To overcome this issue a number of options were discussed with NI and the system was modified to use an analog output module, NI9263. This module ensures a total delay of less than 10 ms. The final position during the half-cycle is sent to the ABB drive via the analog output and the drive then moves to that position using the acceleration, maximum speed and deceleration plus corresponding times that are given in the state machine of settings. This movement is a half-cycle.

In LabVIEW there is a timed loop which changes the value of the analog output. A boolean variable located in the timed loop is used to keep track of the direction in which the piston is moving. Ideally this operation can be repeated at each half of the cycle period, however, due to computing time and communication lag, it was found that a 2ms lag is introduced. This is taken into account in the timed loop.

The two piston control codes are run in parallel but located in different loops. Each loop allows to wait *n* milliseconds to form a phase difference between them. The value of *n* is calculated directly from the cycle time and phase angle required.

Data acquisition

The signal of pressure goes directly to a digital readout box (Druck DPI 280 Series) and through a serial port RS232. The transmitted strings exchanged between the control computer and the readout box use ASCII code. The readout box is accessed by the Compact RIO. The digital signal of absolute pressure and differential pressure can be read by a NI module, NI9870.

Besides the pressures, we have to obtain the temperatures and the piston positions as discussed in section 6.2. To guarantee enough information to analyse each experiment, it is required to obtain a data set (an absolute pressure, a differential pressure, five temperatures and two positions) within 100 ms, i.e. at least 10 data points for the fastest cycle (1 Hz). DMA channel communication can be used to achieve high data acquisition frequency. However, to read the pressure from the digital readout box, the reading command must be sent to it, so it needs two channels (read and write) to build the communication. Two DMA channels have been taken by NI9871 while there are only 3 DMA channels in total on the Compact RIO. Since there is only 1 DMA channel left, an interrupt scheme is used for pressure data transfer in both directions (read and write) and temperature data from the FPGA. By this strategy and the optimal IRQ selection as discussed in the previous section and a fast pressure read option (see below) a full data set can be obtained within 70ms.

The convention used is that a VI always starts with the FPGA asserting a labelled IRQ, i.e. IRQ 2 and IRQ 3. In the LabVIEW code the command to read the absolute pressure is accessed when IRQ 2 is invoked and the differential pressure is accessed when IRQ 3 is used. This directs the input/output to the correct serial port. To ensure a fast data acquisition rate, less than 20 ms according to DPI 280 Series Digital Process Indicator Serial Interface (GE Druck 1997), a short read command is sent to the box. The full format of the command is shown in Table 6.2. Once the box receives the read command it returns a seven character readout of the pressure to the host computer. The typical string that is logged is in the format <±0.9999>.

Table 6.2 Command to read a pressure data (GE Druck 1997)

Byte	1	2	4,5,6	7
Meaning	Start Character	Address	Command	End Character
Code	2	00	000	13

After asserting an IRQ, configurations of TO (Time Out) and EOS (End of String) are given. If a TO occurs during reading, the data already gathered will be returned and the TO indicator will be true. If it happens during the transmission of the read command, the Write VI will attempt to send the byte again and it will make as many attempts as there are bytes in the original string. EOS specifies a termination character and is applied during reading. If an EOS is detected, the read will terminate and all bytes received, including the EOS byte, will be returned. The EOS setting in the LabVIEW code is to guarantee the full string from the box is received.

Five temperatures are read by five thermocouples of type K which are connected to module NI9213. The NI9213 multiplexes 16 thermocouple input channels, one cold-junction compensation (CJC) channel, and one autozero channel to a single analog-to-digital converter (ADC). Each channel of the NI9213 passes through a differential filter and then is multiplexed and sampled by a 24-bit ADC.

Temperature measurement errors depend partly on the thermocouple type. In addition, heat dissipated by adjacent modules or other nearby heat sources can cause errors in thermocouple

measurements by heating up the NI9213 terminals to a different temperature than the cold-junction compensation sensor. The thermal gradient across the terminals can cause the terminals of different channels to be at different temperatures, in which case the resulting measurement creates errors not only in absolute accuracy but also in the relative accuracy between channels.

The NI9213 provides an internal autozero channel to compensate error. When the autozero channel is on, the NI9213 measures the autozero channel and subtracts that measurement from the measurement of each thermocouple channel. In our application, this channel has been used. By doing this, the error between the measured data and real temperature can be reduced significantly.

The NI9213 provides two timing modes to satisfy different requirements detailed in Table 6.3. In this table, it is assumed that the autozero channel is on.

Table 6.3 High-resolution mode and High-speed mode of the NI9213 module (NI 2009a)

Timing Mode	Conversion Time (Per Channel)	Sample Rate (All Channels)	Accuracy (type K)
High-resolution	55 ms	1 S/s	0.02˚C
High-speed	740 µs	75 S/s	0.25˚C

In the current LabVIEW code, high-speed mode is applied to meet the fast sample rate requirement. To simplify the analysis, the raw data is fitted by the Matlab function SPLINEFIT before analysis.

The temperature signal read by NI9213 is in binary format. The equations of converting this binary value to an actual temperature using the cold junction to minimise signal noise can be found in Appendix I.

6.4.2.4 Data log

Since all the data readings are coded in modular structures, it is necessary to collect the data and log them uniformly in an output file. This process is in parallel with the piston control and data acquisition, but independent. All tasks can read and write I/O from the memory table. However, to pass data between tasks, a new set of data was added into the memory table, which also features a component called the LabVIEW shared variable. With LabVIEW shared variables, data can be shared globally within a controller or across a network. Shared variables are configurable, and can be used to provide functionality within a controller and across the network.

There are seven shared variables involved,

stop – A trigger to stop all of the functions.
Position1 – The position of piston1.
Position2 – The position of piston2.
P_a – The absolute pressure in the system.
P_r – The differential pressure across the column.
thermocouples – An array that includes five temperatures.
Time – A uniform clock for all of the tasks.

6.4.3 Task sequence during running the experiment

Most controllers use a single processor to handle all control, monitoring, and communication tasks. Because there is a single resource (processor) with multiple demands, the controller needs a way to manage the demands that are most important. By setting critical control loops to a high priority, a full-featured controller that still exhibits good determinism and responsiveness can be obtained (NI 2009b). For instance, in an application with a pressure control loop and embedded logging functionality, if the control loop is set to a high priority to preempt the logging operation and provide deterministic pressure control. This ensures that lower-priority tasks, such as nondeterministic operations, do not negatively affect analog controls or digital logic (NI 2009b). In this project, three tasks must be set to deterministic controls: piston direction control, absolute pressure read, differential pressure read. Since the

piston position data is read in an Interrupt scheme, using IRQ 1, this command is run prior to the temperature read. Therefore, the tasks run during a cycle of the experiment are executed in the sequence shown below,

1) Piston direction control.
2) Absolute pressure read.
3) Differential pressure read.
4) Position read.
5) Temperature read.
6) Data log.

During the execution, if any task in a period is not executed, there will be a nil value in the data log for the specific task. The frequency of the missing steps will depend on the order of priority, i.e. tasks with highest priority are seldom missed.

6.5 ABB drives configuration

ABB drives control the AC motors directly and have over 100 parameters that can be set. Most of these have been left to their default value as supplied by ABB. Some parameters have been modified and since the drives perform an essential task for the DP-PSA it is important to identify and record all the specific values that are not default. The information on the ABB drives used is shown in Table 6.4. The Compact RIO communicates with the drives by an RS485 port.

Table 6.4 ABB drives properties

Product Family	Drive Type	ACSM1 Motion
	Drive Model	ACSM1-04Ax-07A0-4
Software	Firmware Version	UMFI,1480,0,
	Empty Template	UMFI,2,1.6,ACSM1 Motion Empty Template
	Standard Library	CUSL,1430
	FW API Interface	1.2
	Backup Interface ver	0.3
	FW PARAM IFACE	1.7
	Product Variant	2
Serial Numbers	Memory unit Config	109090551000000000000000000000
	Memory unit HW	68634644d8490106ws
	Power unit	00000000000068689112D7220005V5

Drive references and signals can be monitored with Drive Studio (Data Logger or Monitor Window)(ABB Oy 2008). All the configuration operations of the ABB drives are through this software. Before running the pistons, related parameters should be set in advance.

The key concern is safety. Once the drives are calibrated, a series of limits about the pistons must be double checked. In this project, the settings are listed in Table 6.5.

Table 6.5 Limitation parameters set in this project

Index	Parameters	values
60.13	Maximum Position	0.102m
60.14	Minimum Position	−0.002m
20.01	Maximum Speed	8000rpm
20.02	Minimum Speed	−8000rpm
20.05	Maximum Current	12.16A
20.06	Maximum Torque	125%
20.07	Minimum Torque	−125%
22.05	Zero Speed Limit	30rpm

In the limit parameters listed in Table 6.5, the zero speed limit is the slowest speed that the motor can reach.

Accurate control and real time data logging are important issues for the DP-PSA. The problem lays in the time spent from giving the command from the Compact RIO to the execution of the half cycle inversion of direction. Any communication system delay can be minimised by using an analog input on the drive as the position reference. The control of each VSD (Variable Speed Drive) can be done via the Modbus link. The drives are switched to analog input of the position reference by changing the parameter 65.21 POS REF ADD SEL = AI1. The position reference from the NI controller module, NI9263, is the output via an analog interface. The drive must then be set up to scale the analog input for the position range required. This is done as follows.

For a voltage input at 0-10 V,
13.02 AI1 Max = 10 V
13.03 AI1 Min = 0 V
13.04 AI1 Max Scale = 0.1 m (scaled for maximum travel required)
13.05 AI1 Min Scale = 0 m

Therefore the NI controller outputs 5V to the ABB drive, when the desired final half-cycle position for the piston is 0.05m. The timed loop will then revert to a value of the output of 0V when the piston is to move back to the initial position at 0 m.

Many other parameters of the ABB drives have been changed and these are listed in Appendix II.

6.6 Conclusions

The communications among PC, Compact RIO, ABB drives and pressure readout box have been arranged with the help of the technicians from the University of Edinburgh, ABB and NI. The automation code is programmed in LabVIEW. In the LabVIEW code, different functions have been implemented by individual VIs and they are controlled by a host VI. The host VI

gives a simple interface to the user and provides the user options for the variables which determine the conditions of a sequence of experiments.

Several strategies have been carried out to achieve accurate control and data logging. Through the research and development effort carried out, it was possible to achieve a high frequency data acquisition which allows in less than 70ms to obtain the absolute pressure, the differential pressure, the temperatures and the piston positions for the DP-PSA system. With the Compact RIO system used in this study, this data rate was found to be the fastest achievable. If faster acquisition frequencies are needed, the hardware would need to be modified and the key improvement would be to have a new system with additional DMA channels. National Instruments have recently released a new Compact RIO, the cRIO-9068, which uses the new Artix-7 FPGA and has 16 DMA FIFO channels on a single chassis.

The automation code is now being used by PhD students and PostDocs in the carbon capture group who are currently using the DP-PSA and a user manual has been produced.

7. Characterisation of the DP-PSA system

Table 4.3 included the list of variables and parameters needed to model the DP-PSA system. In order to determine as many parameters as possible under non-adsorbing conditions, experiments were run with an empty column with different pure gases and a column packed with 13X pellets with helium as the non-adsorbing gas. This chapter presents the results of these experiments which were used to characterise the geometry of the system; to develop a correlation for the heat generated in the pistons by friction; and to verify the pressure drop correlation. The results presented in this chapter are all from experiments under non-adsorbing conditions. The parameters of heat and mass transfer during adsorption will be studied in Chapter 8 and Chapter 9.

7.1 Empty column runs

The experiments with an empty column are used to characterise the system with respect to the dead volume, resistance in the piston-column connection, leak rates and heat effects due to the piston movement.

7.1.1 Piston-cylinder and dead volumes

The DP-PSA unit includes dead volumes inside the pistons and in the lines that connect the pistons to the column and in the smaller lines that are linked to the pressure transducers (see Figure 7.1).

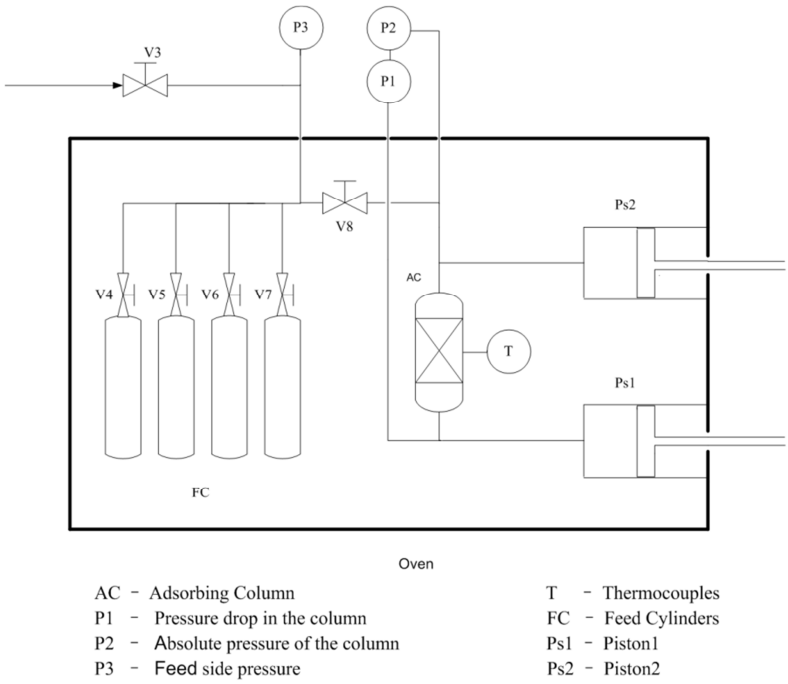

Figure 7.1 The schematic diagram of the DP-PSA in the oven

The procedure adopted to measure these dead volumes is as follows: with the pistons at the maximum stroke position, i.e. minimum system volume, gas is fed into the system through valve V8. Since the total amount of gas in the dosing system and the pressure P3 are known the amount of gas in the column-piston assembly can be calculated from a mass balance using the ideal gas law. By moving the pistons slowly by a known distance the variable volume of the cylinder can be calculated. The pistons are moved slowly, i.e. $v_p = 10 mm/s$, to minimise friction and expansion temperature effects. Using to the ideal gas law the piston cylinder volume and the volume from V8 to the fully compressed pistons are averaged to be $V_p = 1.96 \cdot 10^{-4} m^3$ and $V_{V8-p} = 5.75 \cdot 10^{-5} m^3$, respectively. V_{V8-p} includes the column volume and the dead volume.

$$V_{V8-p} = V_{column} + V_{dead} \qquad \text{Eq.7.1}$$

$$V_{dead} = V_{line1} + V_{line2} + V_{ch} \qquad \text{Eq.7.2}$$

Figure 7.2 The DP-PSA components in the oven

V_{line1} is the volume of the lines between the pistons and the column. V_{line2} is the volume of the lines connecting the column to the pressure transducers. Generally, the volume of the lines does not contribute much to the dead volume. The heads of the two piston cylinders, V_{ch}, are the main contribution to the dead volume. The head of the piston actually is a dead space that the piston never reaches and is included in the design to avoid mechanical wear of the piston assembly and for safety.

The measured dimensions are listed in Table 7.1 and their corresponding components are shown in Figure 7.2.

Table 7.1 Measured dimensions for the DP-PSA components

	Column radius	Column length	Piston cylinder radius	Piston cylinder Length	Line1 radius	Line1 length	Line2 radius	Line2 length
Values (mm)	7.6	13	25	106.5	2.1	380	0.7	1905

From the dimensions in Table 7.1, the column volume is $V_{column} = 2.36 \cdot 10^{-5} m^3$ and the dead volume can be calculated by Eq.7.2 to be $V_{dead} = 3.32 \cdot 10^{-5} m^3$.

7.1.2 Resistance in the piston-column connection

Running the two pistons out-of-phase, i.e. the volume in the system remains constant, allows the measurement of the pressure drop between the two pistons. In the case of an empty column this pressure drop will be dominated by the pressure drop in the lines between the pistons and the column and the contributions from the rapid expansion and reduction at the top and bottom of the column. This mode allows the characterisation of the resistance in the pipes and connections. While the length and shape of the piping is slightly different for the two pistons the pressure drop is small and thus the same resistance is assumed for both pistons.

The maximum pressure drops for He, N_2 and CO_2 and for different cycle times are given in Table 7.2.

Table 7.2 Maximum pressure drop between the two pistons for the empty column run with full stroke at 303K and out of phase. The value reported is the mean value plus/minus the standard deviation if more than one experiment was run.

Cycle time [s]	ΔP He [mbar]	ΔP N_2 [mbar]	ΔP CO_2 [mbar]
4	3.06±0.33	8.97±0.03	13.21
10	0.89±0.02	2.39±0.08	3.07
20	0.4	0.77±0.05	1.02

The pressure drop for an internal flow in pipes can be expressed by Eq.7.3

$$\Delta P = f \frac{L}{D} \frac{\rho_f}{2} v^2 \qquad \text{Eq.7.3}$$

In Eq.7.3, ρ is the density of the gas, v is the velocity of the gas, L and D are the length and diameter of the column respectively, f is the Darcy friction factor which depends on the Reynolds number, Re, of the gas.

In the DP-PSA system, to compare the maximum pressure drops among the experiments in Table 7.2, the maximum flow velocity in the column is used when calculating the Reynolds number. Thus,

$$Re = \frac{\rho_f v_{max} D}{\mu} \qquad \text{Eq.7.4}$$

If $\mathrm{Re} < 2300$, the flow is laminar. If $\mathrm{Re} > 4000$, the flow is turbulent. In the case of laminar flow the Darcy friction factor is given by

$$f = \frac{64}{\mathrm{Re}} \qquad \text{Eq.7.5}$$

Taking Eq.7.4 and Eq.7.5 into Eq.7.3, the density cancels out and the pressure drop is proportional to the viscosity and velocity of the gas. For turbulent flows (Incropera et al. 2011):

$$f = \frac{0.316}{\mathrm{Re}^{1/4}} \qquad \text{Eq.7.6}$$

Clearly in turbulent flow the friction factor will be almost constant, therefore for different gases the pressure drop should be proportional to the molecular weight.

Table 7.3 shows the values of the Re numbers for the cases reported in Table 7.2. N_2 and CO_2 are in turbulent flow while He is always in viscous flow conditions. The ratio of the pressure drops of N_2 and CO_2 are proportional to the ratio of their molecular weights in line with theory. In the case of He the flow regime is laminar which results in a larger Darcy friction

factor; this explains the deviation from the pressure drop which would be expected based on the molecular weight in turbulent flow.

Table 7.3 The Re number for the flows in Table 7.2

Cycle time [s]	Re He	Re N_2	Re CO_2
4	1541	11973	22240
10	616	4789	8896
20	308	2395	4448

7.1.3 System leak rates

Since the system is run in total reflux mode and several experiments are run sequentially it is important to quantify the leak rate of the system. The leak rate is usually defined as $\tilde{k}$ in $\frac{dP_i}{dt} = \tilde{k}(P_{i,\infty} - P_i)$. Here $P_{i,\infty}$ is the partial pressure of component i outside the system and P_i is the partial pressure of component i in the system. In our model, to build the link between the leak rate and the system volume, the leak rate is represented by K,

$$K_{leak} = \frac{\tilde{k} \times V_{system}}{R \times T} \qquad \text{Eq.7.7}$$

In the model, the leak rate is expressed by $f(t) = K_{leak}(1 - P_i)$, where P_i is the partial pressure of component *i*.

Table 7.4 Leak rates of different gases

GAS	T [K]	$P_{i,0}$ [bar]	K [mole s^{-1} bar^{-1}]
He	315	1.97	8.4×10^{-8}
N_2	317	1.54	6.4×10^{-8}
CO_2	370	1.8	3.5×10^{-8}

For different gases, the values of K were normalised and listed in Table 7.4.

The parameter K is estimated by fitting the experimental pressure to the leak rate equation. Several experiments and fittings were performed for the three gases and spanning temperatures from 300 to 380 K and cycle times from 4 to 20 s. The leak rate for these experiments varied between 3.5×10^{-8} and 12.4×10^{-8} mol s^{-1} bar^{-1} with no clear dependency on the gas composition, temperature or cycle time. While it would be preferable to match the leak rate to the specific experimental conditions, simulations with the average leak rate of 8×10^{-8} mol s^{-1} bar^{-1} are able to match the experimental data for simulations up to 3 hours with a relative error , $\frac{\left|P_{\exp}-P_{sim}\right|}{P_{\exp}}$, of less than 8% in the pressure. In the model, it is assumed that the leak is localised in the pistons with a rate of 4×10^{-8} mol s^{-1} bar^{-1} at each piston. In Figure 7.3, it shows a leak rate experiment where the pistons were running out-of-phase. The average pressure of the simulation and of the experiment are compared. The slope of the experimental pressure increases during the first 1.5 hours. The potential reason is that the system heats up due to friction in the pistons which will be discussed in the next section.

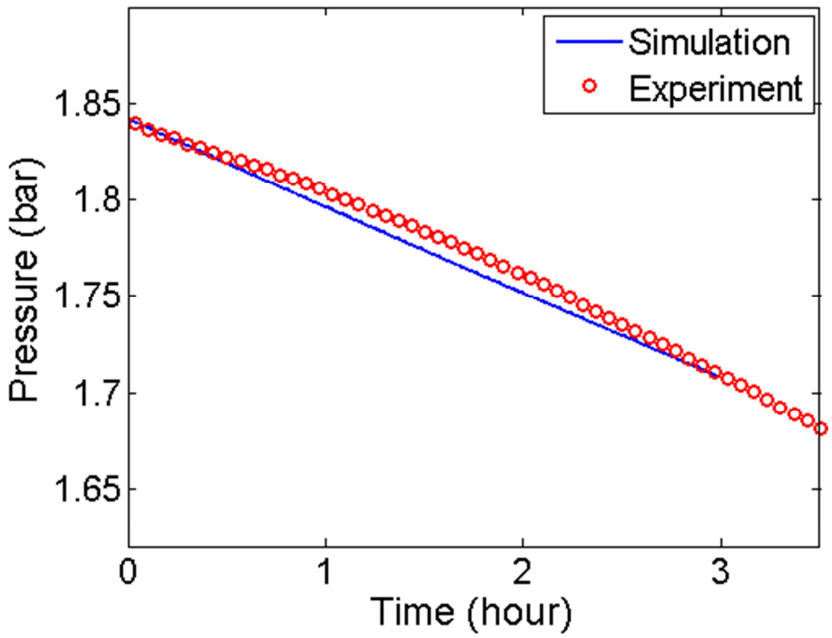

Figure 7.3 A representative leak comparison between the experiment and the simulation

7.1.4 Friction heating

During the leak tests it became evident that the temperature in the system increases due to the heat generated by friction in the moving pistons.

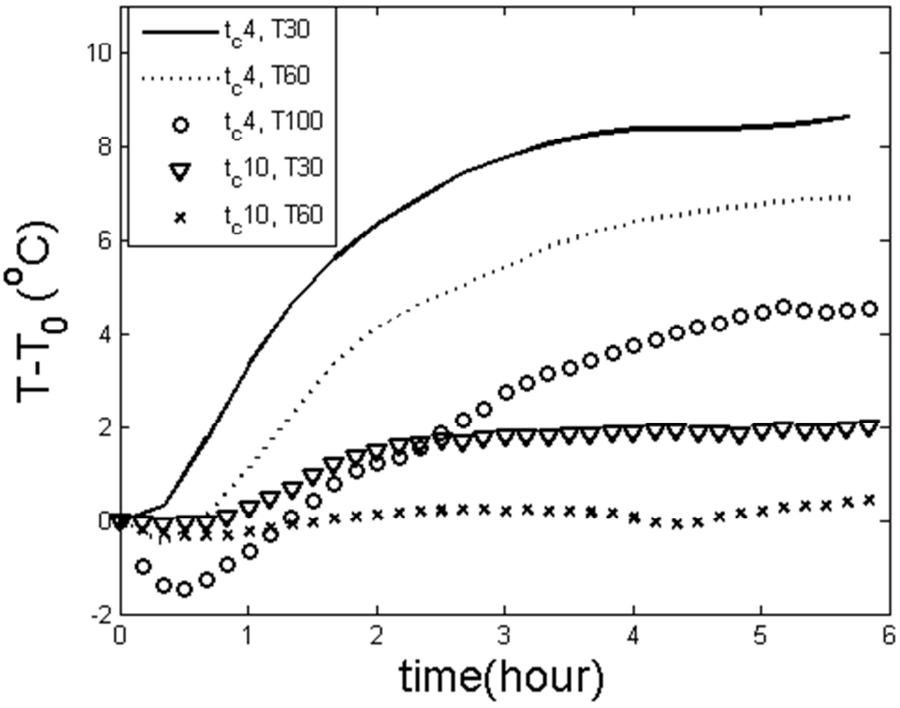

Figure 7.4 Column temperature profiles in different conditions

Table 7.5 Maximum temperature increases, due to friction heat, among different experiments (T: temperature; T_c: cycle time)

Experiment	T30 T_c =10	T30 T_c =4	T60 T_c =10	T60 T_c =4	T100 T_c =20	T100 T_c =10	T100 T_c =4
$T_{max} - T_0$ (°C)	2.0472	9.1139	0.5818	7.1093	0.1743	0.2152	4.9168

Several experiments with pistons running out of phase have been run using helium to study the heat generated by the friction of the pistons. The maximum temperature increases, compared to the initial temperature, are shown in Table 7.5. It is clear that with the same velocity, the temperature increases more for a lower oven temperature. If the initial temperatures are the same, the runs with higher piston velocities produce more heat, as would be expected. The detailed temperature profiles are shown in Figure 7.4.

The friction parameters, f_1, f_2 and f_3, see Eq.4.20, are determined from the empty column experiments for each set of operating parameters: temperature, cycle time; and stroke length. Table 7.6 gives the friction parameters for some representative fast cycle experiments.

Table 7.6 The friction parameters for a few experiments (T_c: cycle time; SL: stroke length)

T (°C)	T_c (s)	SL (mm)	f_1 (J m^{-3} s^{-1})	f_2 (s)	f_3 (s)
30	1	0-25	115520	1.71	3670
30	1	75-100	104800	1.50	2555
30	2	0-50	140689	1.95	3131
30	4	0-100	116140	1.81	2150
60	1	0-25	85590	2.66	2032
60	1	75-100	96790	1.43	3054
60	4	0-100	124100	1.88	2586
100	1	0-25	78310	2.86	3076
100	4	0-100	124740	1.64	3788
30	10	0-100	52246	2.76	1544
60	10	0-100	32810	-0.23	5948
100	10	0-100	52790	-0.10	2167
100	20	0-100	56490	-0.77	4054

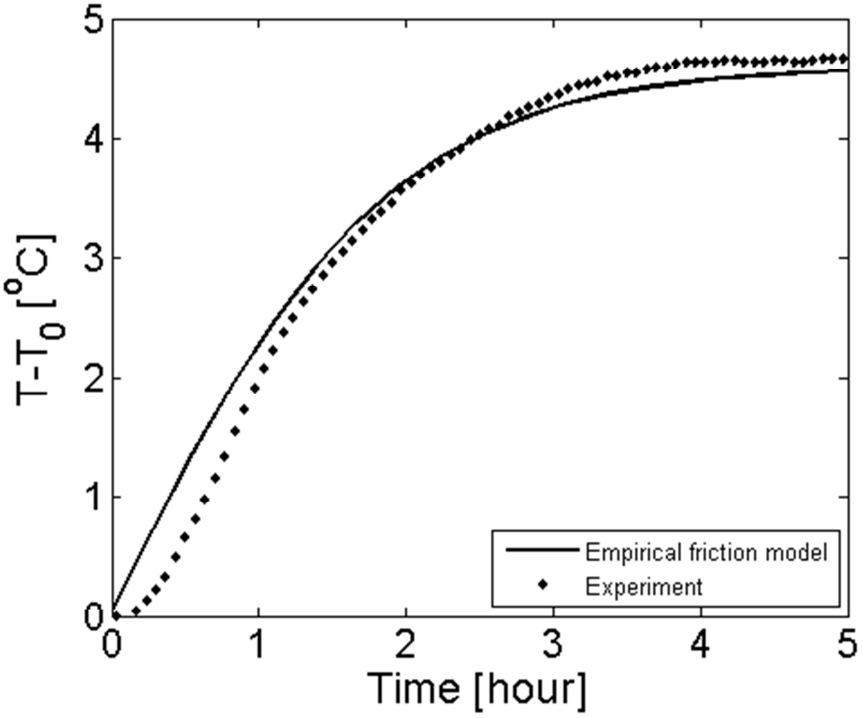

Figure 7.5 Comparison of the average temperature between the experimental and the calculated from the empirical piston friction model

Figure 7.5 shows a representative example of the comparison between the experimental temperature and that calculated from the empirical piston friction model.

7.2 Packed column runs

7.2.1 Void fraction

The adsorption column was then packed with zeolite 13X pellets. The column was filled with 12.979 g of large 13X pellets which have an average diameter of 4 mm, plus two pellets in which thermocouples are inserted. These two pellets have weights of 0.0527g and 0.0676g. The dry sample weights are calculated from independent TGA experiments which show that the weight loss after regeneration of the adsorbent is usually between 10% and 12.9% of the total mass (Mangano 2013). In the DP-PSA experiment, we assume the dry sample packed in the column is 11.552g and the pellets attached to the thermocouples are 0.0469g and 0.0602g respectively. In the model simulations, the mass of solid has to be converted into a solid volume. The pellet density and the void fractions are linked to the dry mass of the pellets by

$$m = (1-\varepsilon)(1-\varepsilon_P)V_{8-p}\rho \qquad \text{Eq.7.8}$$

To determine the void space in the column, the system was run with helium to measure also the pressure drop along the column under non-adsorbing conditions.

The dead volume was determined using the procedure outlined in section 5.9.3. The volume from V8 to the fully compressed pistons averaged over three experiments is $V_{V8-p} = 4.42 \cdot 10^{-5} m^3$. This value includes the volume of the column as well as the dead volume.

As mentioned in Chapter 2, the pellet void fraction was measured by mercury porosimetry. The crystal void fraction was calculated from the framework structure of faujasite (Meier and Olson 1987). By running the helium experiment, the total void fraction is measured, $\varepsilon_t = 0.79$. The bed void fraction ε can be calculated by

$$\varepsilon_t = \varepsilon + (1-\varepsilon)(\varepsilon_P + (1-\varepsilon_P)\varepsilon_{cry}) \qquad \text{Eq.7.9}$$

The calculated result, $\varepsilon = 0.43$, which is reasonable for a column packed with a D/d_P of approximately 4 (De Klerk 2003).

7.2.2 Confirmation by the non-adsorbing experiments

In the non-adsorbing experiments, the main physical process is the compression/expansion of the gas and the associated heat transfer to and from the particles. It is expected that, if the cycle time is short enough, the heat transfer between the solid and the gas cannot reach equilibrium, so the temperatures should be quite different. To support this assumption experiments were run with T_c = 2 s and T_c = 10 s. The gas and solid temperatures are shown in Figure 7.7 for two cycle times.

a)

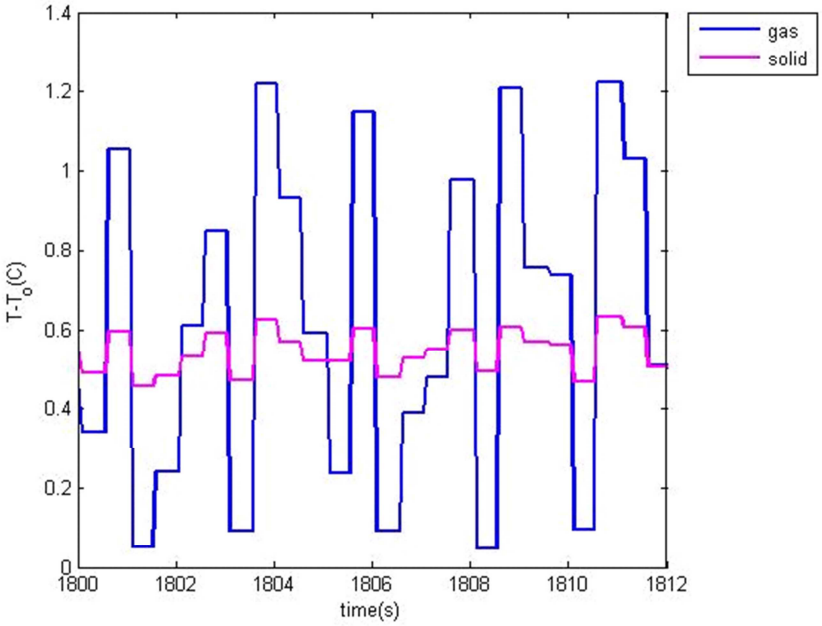

b)

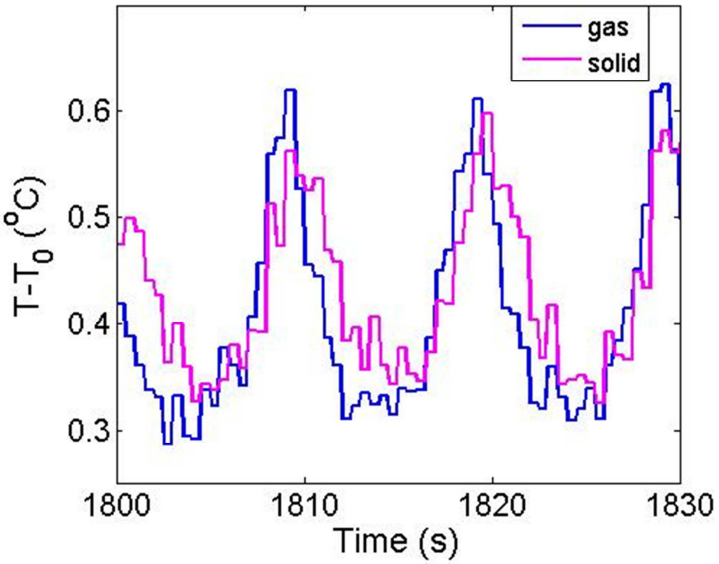

Figure 7.6 The solid and gas temperature profile of a helium experiment with T_c=2s (a) and T_c=10s (b) (He, T_0=30˚C; T_c=10s; Phase angle=0.5π; Stroke1=Stroke2=0~100mm)

This sequence of experiments clearly shows that the heat transfer time constant is of the order of 5-10s. The cycle time does not give a measurable effect to the total pressure for the non-adsorbing gas since the temperature drift due to the piston friction is less than 0.4%. It is clear that significant additional information is gained by the presence of the thermocouples.

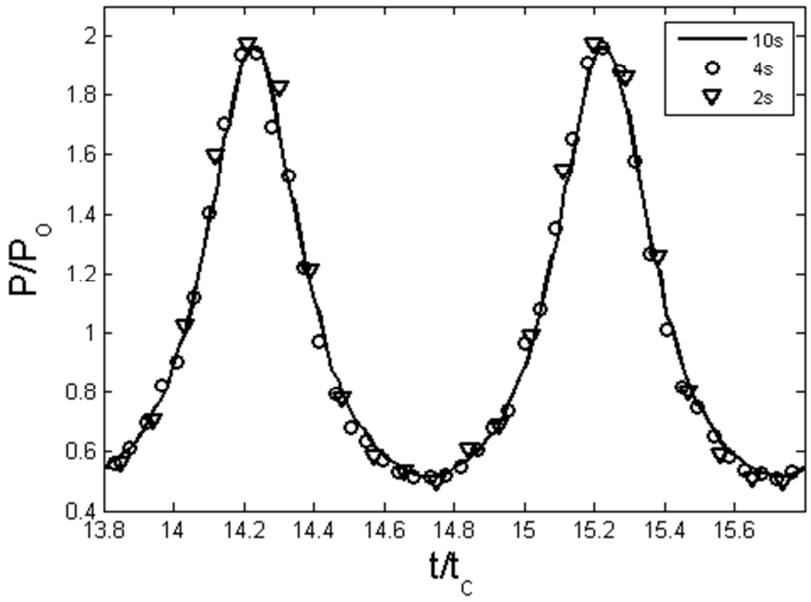

Figure 7.7 Dimensionless pressure profiles for different cycle times without adsorption (He, T_0=30˚C; Phase angle=0.5π; Stroke1=Stroke2=0~100mm)

In Figure 7.7, the pressure profiles are normalised with respect to the pressure amplitude and the cycle time. P_0 is the average pressure of the first cycle. The normalised pressure profiles for different cycle times overlap almost perfectly and it confirms that the resistance between the column and the pistons is negligible. The pressure curves are periodic and successive peaks have the same amplitude, which also confirms that the leak rate of the system is small enough when the pistons are running.

7.3 Conclusions

Preliminary experiments to characterise the system have been presented in this chapter. In the empty column experiments, the dead volume and the resistance in the piston-column connection of this system were measured. The leak rate and friction heat of the system were characterised as well. This characterisation of the system is crucial to account for these effects in the analysis of novel adsorbents. The friction heating is determined by experiments running under different conditions while still keeping the adsorbent column empty. In the following experiments, the column was packed with zeolite 13X. The void fraction was tested firstly. Then non-adsorbing experiments were run to confirm the system. Temperature and pressure

profiles were characterised. The result confirmed the feasibility of this apparatus, as well as its efficiency.

For ease of reference, the parameters obtained are listed in Table 7.7 and they are confirmed by running non-adsorbing experiments.

Table 7.7 The parameters obtained in chapter 7

Piston	Cylinder length [m]	0.1065
	Inner cylinder radius [m]	0.025
	Wall thickness [m]	0.0125
	Cylinder wall density [kg/m^3]	8238
	Friction parameter 1	See Table 7.6
	Friction parameter 2	See Table 7.6
	Friction parameter 3	See Table 7.6
	Leak parameter [mol s^{-1} bar^{-1}]	4×10^{-8}
Column	Column length [m]	0.13
	Column radius [m]	0.0076
	Void fraction of the packed bed	0.43
	Void fraction of the pellet	0.27
	Column wall density [kg/m^3]	8238
	Column wall thickness [m]	0.005
	Pellet density [kg/m^3]	841

8. Zeolite 13X Packed Experiments by DP-PSA

8.1 Introduction

There are many experimental conditions such as the gas composition; initial temperature and pressure; gas velocity; cycle time and compression ratios that can be varied in the DP-PSA apparatus. The resulting experiments can be interpreted using dynamic simulations to test the validity of the adsorption column model over a wide range of parameters which are representative of various conventional PSA processes. To obtain the parameters needed to characterise fully the DP-PSA model, more than 400 experiments with different conditions were run which are listed in Appendix III. Each experiment was run over a long period in order to ensure cyclic steady state. Although the system is designed to run experiments of 1Hz, these experiments take more than 6 hours to reach cyclic steady state due to the heat generated by the friction in the pistons. Thus, few 1Hz experiments are included and more experiments are at 0.5Hz and 0.25Hz to characterise fast cycle conditions. Carbon dioxide and nitrogen are used in the experiments, because they are the main constituents of flue gas. The basic information required is the adsorption kinetic and equilibrium behaviour of the pure components. In this chapter, the behaviour of the pure gases is reported first. Then experiments with mixtures of carbon dioxide and nitrogen are considered and predictions based on the pure component runs are used to confirm the parameters obtained. The current design of the DP-PSA unit does not include a concentration sensor, so the temperature gradient in the column is tested as a possible indicator of gas separation.

8.2 Pure gas experiments

8.2.1 Parameters determined in the simulations

After the characterisation of the system in Chapter 7, in the model the additional parameters required here are the isotherm and kinetic parameters; the axial dispersion coefficient; the axial thermal coefficient; and the heat transfer parameters. The isotherm parameters applied

here are those obtained from volumetric experiments by Dr Mangano, which are reported in Chapter 2. The other parameters were initially predicted by the calculations. Since the diffusion mechanism of CO_2 in zeolite 13X is macropore controlled (Hu et al. 2013), the adsorbed phase in the micropores is at equilibrium with the gas in the macropores. The LDF coefficient for the macropores, k^p, is the most important parameter to determine the adsorption kinetics. It can be calculated from the diffusivities (Ruthven 1984).

$$D_{k,i} = 97 R_{pore} \sqrt{\frac{T}{MW_i}} \qquad \text{Eq. 8.1}$$

$$D_m = 1.6\times10^{-7} \frac{\sqrt{T^3\left(\frac{1}{MW_1}+\frac{1}{MW_2}\right)}}{P\sigma_{12}{}^2\Omega_{12}} \qquad \text{Eq.8.2}$$

Using the Knudsen diffusivity, $D_{k,i}$, and molecular diffusivity, D_m, defined in Eq.8.1 and Eq.8.2, the combined diffusivity for a binary gas (for equimolar counter diffusion) can be expressed by (Ruthven 1984)

$$\frac{1}{D} = \frac{1}{D_k} + \frac{1}{D_m} \qquad \text{Eq.8.3}$$

In addition to Knudsen diffusivity and molecular diffusivity, viscous resistance must be considered and the equivalent diffusivity, D_v, is defined by Eq.8.4 (Ruthven 1984).

$$D_v = \frac{R_{pore}{}^2 P}{8\mu} \qquad \text{Eq.8.4}$$

Where P is the mean absolute pressure, r is the mean pore radius, and μ is the viscosity. Because the viscous flow is in parallel with the diffusive flow, D_v is additive to D. The combination of them is the overall diffusivity, D_o.

$$D_o = D + D_v \qquad \text{Eq.8.5}$$

At low pressure, Knudsen diffusivity is dominant. As the pressure increases, there is a transition from Knudsen control to viscous control. Taking the void fraction of the pellet, ε, and the tortuosity of the macropores, τ, into account, the effective macropore diffusivity, D_p^e, can be obtained by (Ruthven 1984).

$$D_p^{\ e} = \frac{\varepsilon_P}{\tau} D_o \qquad \text{Eq. 8.6}$$

The values used for the simulation in this chapter are listed in Table 8.1.

Table 8.1The effective macropore diffusivity used for the simulation

Gas	N_2		CO_2	
T (K)	303	373	303	373
$D_p^{\ e} \times 10^5$ (m^2/s)	1.282	1.2565	1.2392	1.2281

The axial dispersion coefficient and the axial thermal coefficient can be predicted from Eq. 8.8 and Eq.8.9 respectively.

$$D_Z = \frac{D_m}{\varepsilon}(20 + 0.5 Sc \,\mathrm{Re}) \qquad \text{Eq. 8.8}$$

$$\lambda_z = k(7 + 0.5\, Pr\, Re) \qquad \text{Eq. 8.9}$$

The Reynolds numbers are expressed by Eq.8.10 to Eq.8.12.

For the pellet: $$Re_p = \frac{MW_i \times F \times 2 \times R_p}{\pi \times R_p^{\,2} \times \mu}$$ Eq.8.10

For the column: $$Re_c = \frac{MW_i \times F \times 2 \times R_c}{\pi \times R_c^{\,2} \times \mu}$$ Eq.8.11

For the pipes: $$Re_{pipe} = \frac{MW_i \times F \times 2 \times R_{pipe}}{\pi \times R_{pipe}^{\,2} \times \mu}$$ Eq.8.12

The Nusselt number for the pellet is given by the Wakao equation (Wakao et al. 1979).

$$Nu_p = 2 + 1.1 \times \mathrm{Pr}^{0.33} \times \mathrm{Re}_p^{\,0.6}$$ Eq.8.13

The Nusselt number for the column is calculated from Li and Finlayson's correlation (Li and Finlayson 1977)

$$Nu_c = \frac{2.03 \times \mathrm{Re}_p^{\,0.8}}{e^{6 \times R_p / R_c}}$$ Eq.8.14

$$Nu_{pipe} = 1.86 + \left(\mathrm{Re}_{pipe} \times \mathrm{Pr} \times \frac{2 \times R_{pipe}}{L_{pipe}} \right)^{1/3}$$ Eq.8.15

The heat transfer coefficient is then derived by

$$h_i = \frac{k \times Nu_i}{2 \times R_i}$$ Eq.8.16

The specific heat capacity of the column and the adsorbent are 500 J/(kg K) (ASM Aerospace Specification Metals Inc. 2014) and 920 J/(kg K) (Grande and Rodrigues 2007), respectively.

Using the parameters calculated from the correlations above, a representative experiment is simulated. The pressure and temperature are shown in Figure 8.1 and Figure 8.2.

From Figure 8.1, it is found the experimental pressure can be well predicted. In Figure 8.2, the predicted gas temperature does not agree with the experimental. It is due to the reason that the thermocouple outside the particle when used in the packed column experiments may not measure the actual gas temperature since the thermocouple may be in contact with the surface of a particle. Thus, the disagreement of the gas temperatures in Figure 8.2 is acceptable since the experimental measurement is in fact an average of the predicted solid and gas temperatures. The solid temperature agrees well with the experimental values, validating the correlations given above. More accurate heat transfer coefficients could be obtained by fitting the experimental data exactly using a trial and error method. However, it is time consuming requiring several hours as for each case simulations to cyclic steady state have to be run and an automated fitting procedure would be preferable. Therefore, the calculated heat transfer coefficients are used to predict the experimental performance without further fitting.

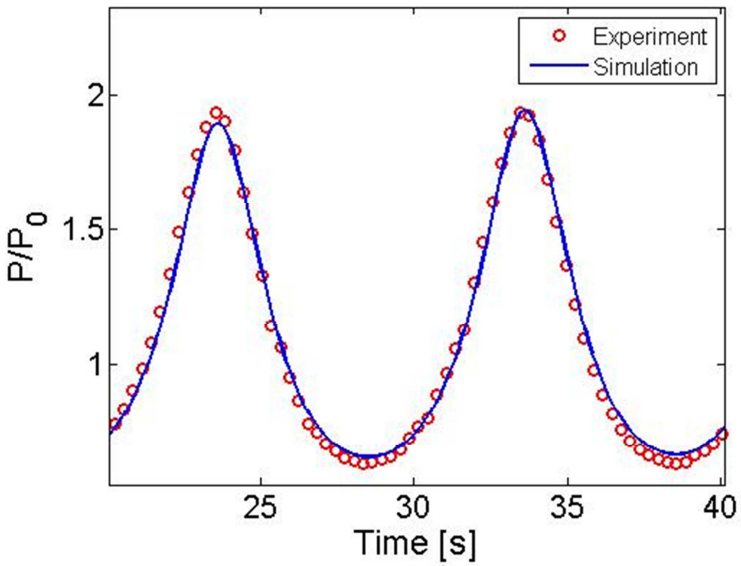

Figure 8.1 Comparison of the experimental pressure and the simulated pressure (CO_2; T_0=30˚C; T_c=10s; Phase angle=0.5 π; Stroke1=Stroke2=0~100mm; P_0 =1.16bar)

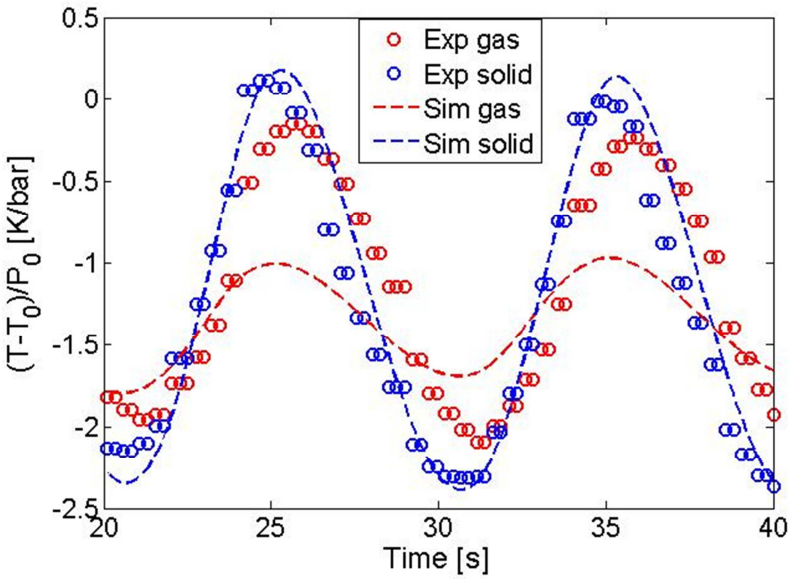

Figure 8.2 Comparison of the experimental temperature and the simulated temperature (CO_2; T_0=30˚C; T_c=10s; Phase angle=0.5 π; Stroke1=Stroke2=0~100mm; P_0 =1.16bar)

8.2.2 Effect of different gases

For adsorbing and non-adsorbing experiments there should be a clear difference. The absolute pressures are compared in Figure 8.3 and Figure 8.4. The initial pressure, P_0, is the average pressure of the first cycle.

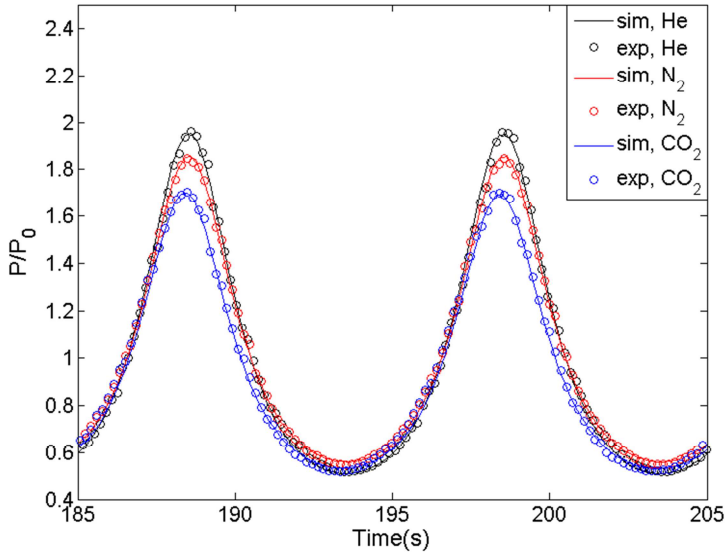

Figure 8.3 The pressure of different gases with an initial pressure of approximately 1 bar (T_0=30˚C; T_c=10s; Phase angle=0.5 π; Stroke1=Stroke2=0~100mm; P_{0_He}=0.975bar, P_{0_N2}=0.984bar, P_{0_CO2}=1.22bar)

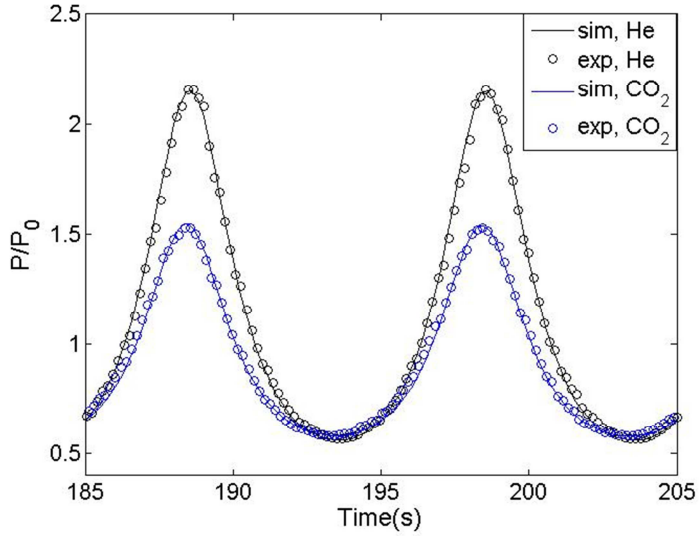

Figure 8.4 The pressure of different gases with a low initial pressure (T_0=30˚C; T_c=10s; Phase angle=0.5 π; Stroke1=Stroke2=0~100mm, P_{0_He}=0.3bar, P_{0_CO2}=0.22bar)

Figure 8.3 shows the effect of different adsorption strengths for a 10s cycle by comparing the pressure profile for CO_2, N_2 and He runs in the same cycle configuration. As expected the amplitude of the pressure fluctuations follows the inverse order of the adsorption strength, i.e. He > N_2> CO_2. In the CO_2 experiment of Figure 8.3, the pressure swings from 0.756bar to 2.074bar (note: the pressure shown on the figure is after normalisation). The adsorption difference between this range does not change significantly according to the isotherm shown in Chapter 2. The CO_2 and He experiments have been repeated for a lower initial pressure. The normalised pressures are shown in Figure 8.4. The pressure fluctuation range is from 0.13bar to 0.34bar.The adsorption capacity changes significantly in this range, so we can see clear pressure difference between CO_2 and He in Figure 8.4.

By comparing the position of the pressure peaks of the experiments it can be seen that there is also a corresponding time-shift in the order CO_2>N_2≈ He, which corresponds closely to the volume of the system. When the pressure increases, the peak pressure of the non-adsorbing He and weakly adsorbing N_2 occur at the time of the minimum system volume. However, this is not true for the strongly adsorbing CO_2 where the maximum pressure occurs slightly ahead of the minimum system volume, because the adsorbed phase concentration lags. This is a kinetic effect which reduces with increasing cycle time.

a)

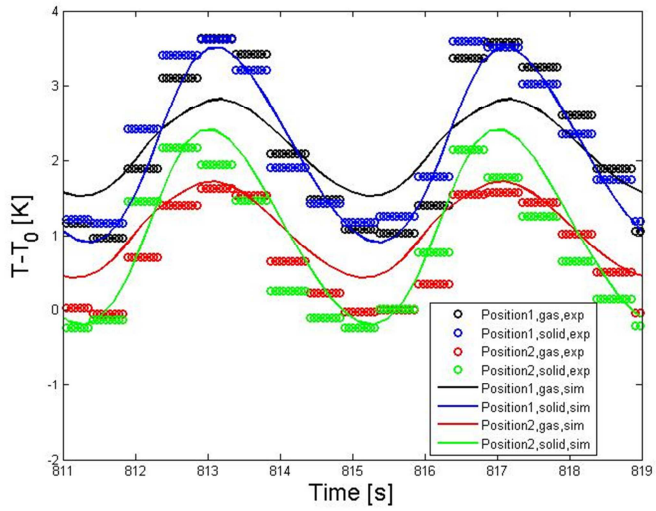
T-T0 [K]
Time [s]
Position1,gas,exp
Position1,solid,exp
Position2,gas,exp
Position2,solid,exp
Position1,gas,sim
Position1,solid,sim
Position2,gas,sim
Position2,solid,sim

b)

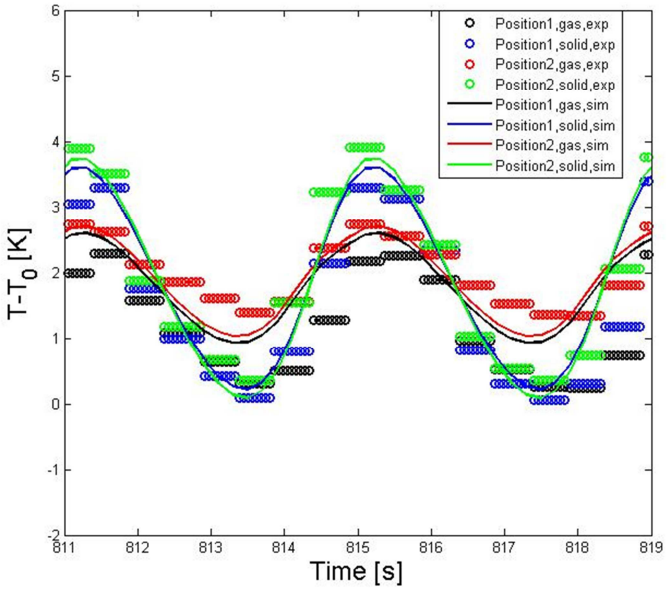
T-T0 [K]
Time [s]
Position1,gas,exp
Position1,solid,exp
Position2,gas,exp
Position2,solid,exp
Position1,gas,sim
Position1,solid,sim
Position2,gas,sim
Position2,solid,sim

c)

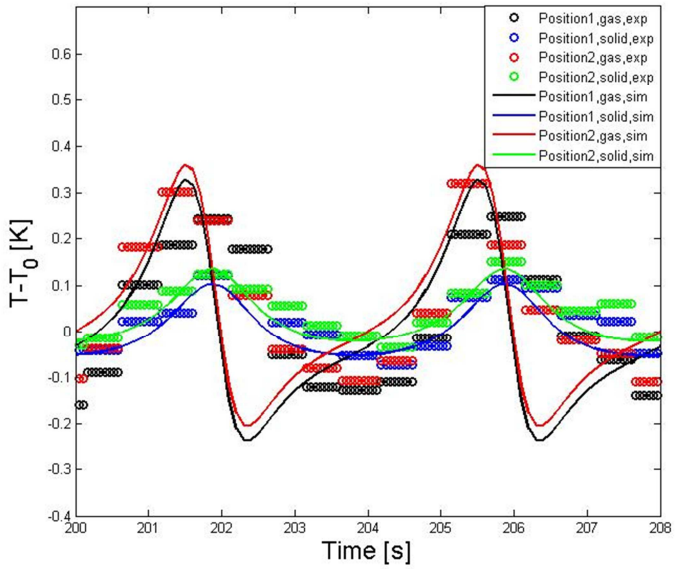

Figure 8.5 The temperature response for CO_2 in an asymmetric run (a) (T_0=30˚C; T_c=4s; Phase angle=0.5 π; Stroke1=Stroke2=0~100mm; P_0 =1.41bar) and for CO_2 in a symmetric run (b) (T_0=30˚C; T_c=4s; Phase angle=0; Stroke1=Stroke2=0~100mm; P_0 =1.15bar) and for He in an asymmetric run (c) (T_0=30˚C; T_c=4s; Phase angle=0.5π; Stroke1=Stroke2=0~100mm; P_0 =0.942bar)

The effect of the adsorbing and non-adsorbing gas becomes directly evident when the temperatures inside the column are displayed, see Figure 8.5. The temperature swing for the CO_2 experiment is above 2.4 K compared to 0.4 K for He. In addition the temperature difference between the two locations is a consequence of the asymmetric cycle (Ph=0.5$\boldsymbol{\pi}$) which generates a temperature gradient along the column (this will be explained in section 8.2.4). In contrast to Figure 8.5 (a), the CO_2 experiment was repeated but with a symmetric configuration (Ph=0), and as a result the temperature difference between the two locations disappears, see Figure 8.5 (b).

In order to assess the approach to cyclic steady state, it is useful to consider the average temperature over a cycle as a function of time. This has also highlighted the need to explain the long-time drifts in both temperature and pressure.

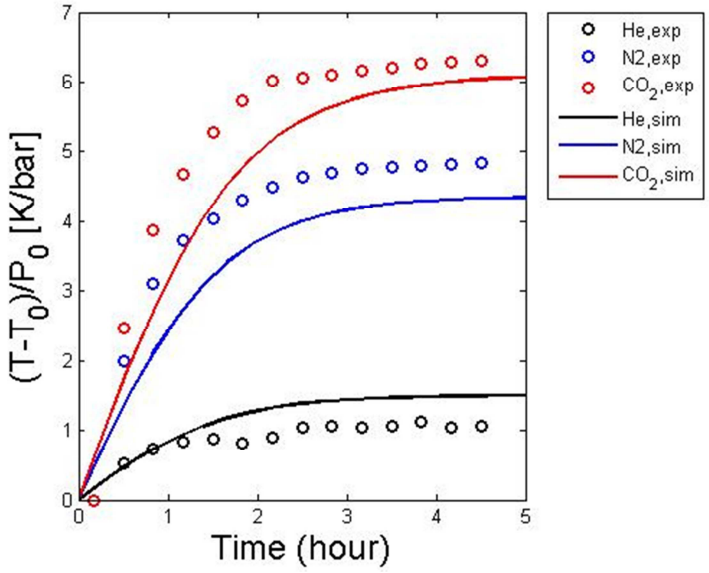

Figure 8.6 Average temperature profiles of different gas runs (T_0=30˚C; T_c=4s; Phase angle=0.5π; Stroke1=Stroke2=0~100mm; P_{0_He}=0.942bar, P_{0_N2}=0.956bar, P_{0_CO2}=1.41bar)

Table 8.2 Maximum averaged temperature increases during 5 hours (T_0=30˚C; T_c=4s; Phase angle=0.5π; Stroke1=Stroke2=0~100mm)

	He (K)	N_2 (K)	CO_2 (K)
T1	1.04	4.69	6.31
T2	1.05	4.72	6.19
T3	0.7	3.50	4.51
T4	0.69	3.34	4.37

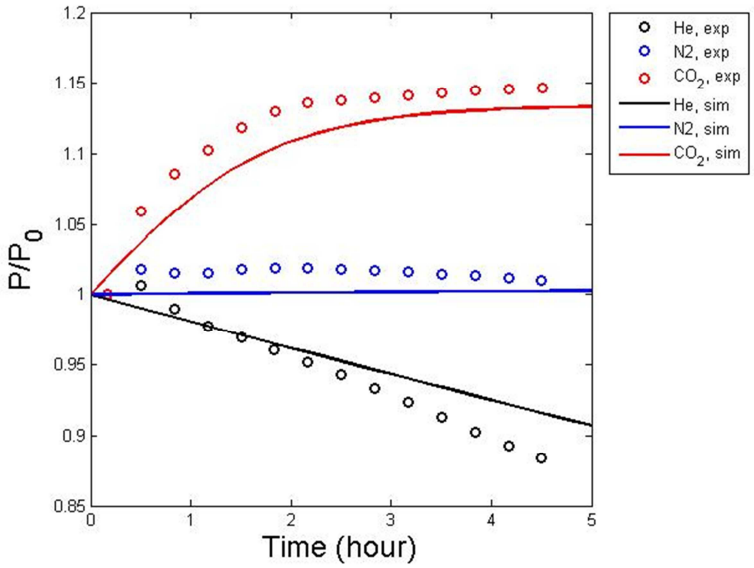

Figure 8.7 Average pressure profiles of different gas runs (T_0=30˚C; T_c=4s; Phase angle=0.5π; Stroke1=Stroke2=0~100mm; P_{0_He}=0.942bar, P_{0_N2}=0.956bar, P_{0_CO2}=1.41bar)

For strongly adsorbing gases, large amounts of gas molecules will be adsorbed in a very short time. Since the experiments are run with almost the same initial pressure, the total gas fed to the system is larger. Once the experiment starts, the temperature increases due to friction heat, which results in desorption following the adsorption isotherms. Therefore, in the case of the same initial pressure, the overall temperature of the strong adsorbing gas increases more than the less-adsorbing and non-adsorbing gases. The average gas temperature profiles at position1 for a 5 hour run are plotted in Figure 8.6. It shows that the temperature increase of CO_2 is the highest and that of He is the lowest. The maximum of the other three temperatures (gas and solid temperature at position2; solid temperature at position1) can be found from Table 8.2. T1 and T3 are the gas temperatures while T2 and T4 are the solid temperatures. T1 and T2 are measured near the middle of the adsorbing column while T3 and T4 are measured at 1/3 of the adsorbing column as illustrated in Figure 4.2. Figure 8.7 gives the average pressure for these three experiments. In all of the experiments, there is an unavoidable leak (see Chapter 7). That is why the average pressure of He (with highest leak rate) decreases. But the average pressure increase of CO_2 is due to desorption.

8.2.3 Effect of varying the cycle time

In the case of the adsorbing experiment, with various cycle times, the pressure profiles are different, see Figure 8.8.

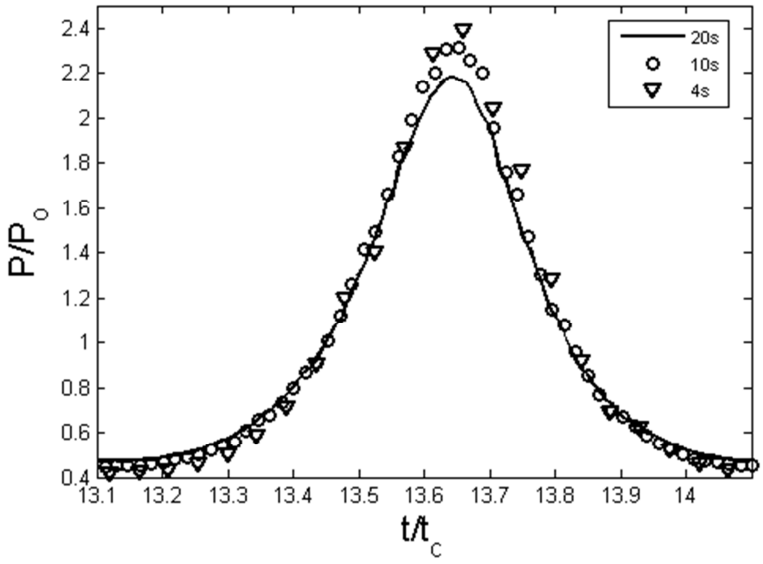

Figure 8.8 Comparison of the pressure profiles for CO_2 runs at different cycle times (CO_2, T_0=30˚C; Phase angle=0.5π; Stroke1=Stroke2=0~100mm; P_{0_20s}=1.19bar, P_{0_10s}=1.22bar, P_{0_4s}=1.41bar)

Comparing the peak pressure at maximum compression shows the effect of the mass transfer resistance on the adsorption of CO_2. The maximum pressure of these curves is decreasing with increasing cycle time. It was found that experiments with cycle times larger than 20s showed the same response as shown for the cycle with T_c=20s. Thus the pressure profile for these slow cycles is not dependent on the kinetics but only on the adsorption isotherm.

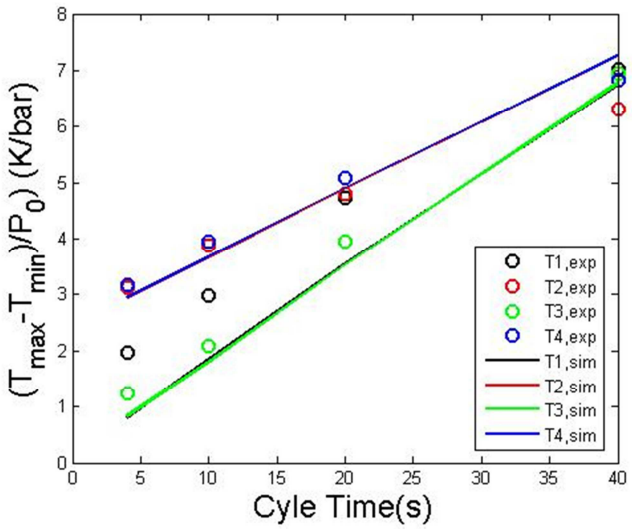

Figure 8.9 Gas and adsorbent solid temperature swing amplitude (T_{max}–T_{min}) for CO_2 (CO_2, T_0=30˚C; Phase angle=0; Stroke1=Stroke2=0~100mm; P_{0_4s} =1.15bar, P_{0_10s} =1.21bar, P_{0_20s} =1.3bar, P_{0_40s} =1.09bar)

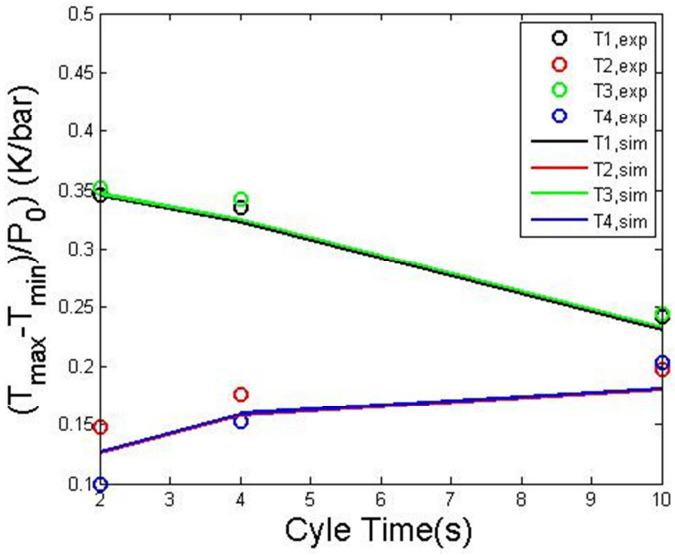

Figure 8.10 Gas and adsorbent solid temperature swing amplitudes for He (He, T_0=30˚C; Phase angle=0.5π; Stroke1=Stroke2=0~100mm; P_{0_2s} =1.25bar, P_{0_4s} =0.94bar, P_{0_10s} =1.07bar)

The gas and solid temperatures at different positions for adsorbing and non-adsorbing experiments are compared. The temperature swing amplitudes (T_{max}–T_{min}) are shown in Figure 8.9 and Figure 8.10. In the case of the adsorbing experiments the main contribution is given by the heat of adsorption. Therefore the average temperature of the solid is higher than that of the gas in the CO_2 experiments. The opposite is true for the He experiments where the only contribution is due to the heat generated during compression/expansion, so the heat

transfer is driven from the gas to the solid. As a result the temperature swing increases with cycle time for the CO_2 experiments, since the amount adsorbed increases accordingly. It is also found the temperature of the gas and the solid phase tend to converge at T_c=40s where the system is under equilibrium control. In the He experiments the gas temperature swing decreases with cycle time as more energy is transferred to the oven and the solid and gas temperatures tend to converge since the heat transfer time constant is of the order of 5 s.

For the in-phase CO_2 experiments there should be no difference in the temperature between the two positions. There seems to be good agreement for the temperatures of the solid, but there is a clear difference in the gas phase temperatures. These observations may be explained by the fact that the thermocouple in the gas phase may be in contact with the surface of a particle and hence what is recorded is an intermediate temperature. This uncertainty can be removed in the single pellet experiments reported in Chapter 9.

In the He experiments, the phase angle was 0.5π.This was chosen to avoid that the maximum pressure exceeded the allowable limit of the pressure transducer (3.5bar). In the case of the non-adsorbing gas there should be minimal temperature gradients in the column. In Figure 8.10, the temperature swing amplitudes for different positions are almost the same.

8.2.4 Effect of changing the phase angle

If the experiment with Ph=0.5 π is taken as an example, Figure 8.11 shows the average gas temperatures during 5 hours along with the simulation results. In the experiment of Ph = 0.5π, the temperature in position2 (close to piston 2) is around 2K lower than the temperature in position1 when the system reaches cyclic stead state.

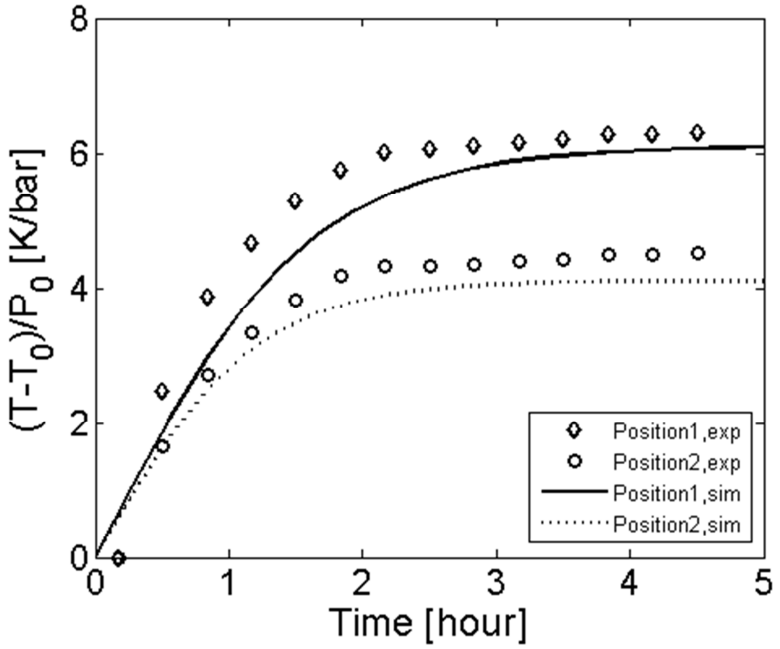

Figure 8.11 Average temperature in 5 hours when CO_2 was run in the column packed with zeolite 13X (CO_2, T_0=30˚C; Phase angle=0.5π; T_c=4s; Stroke1=Stroke2=0~100mm; P_{0_CO2}=1.41bar)

In the case of Ph=0.5π, a cycle process is shown in Figure 8.12.

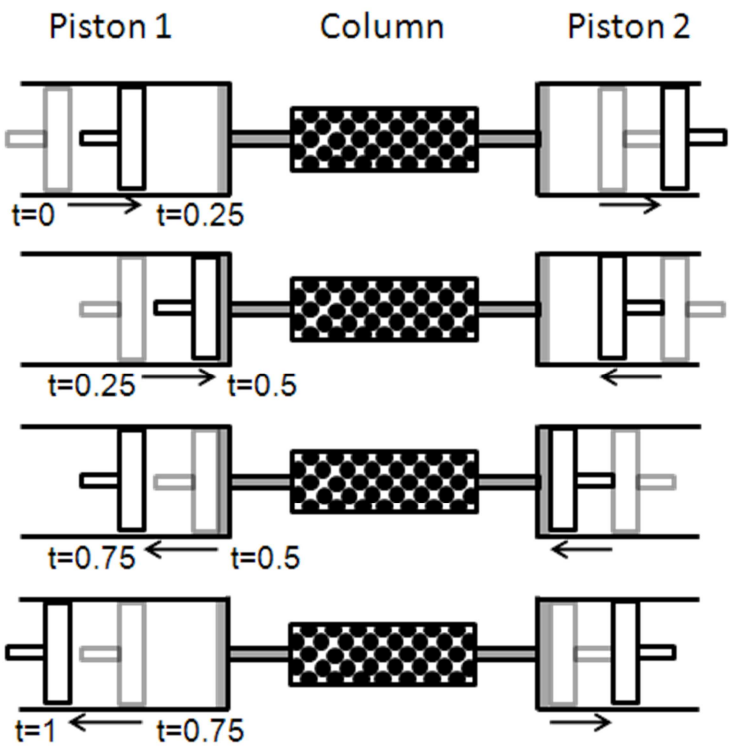

Figure 8.12 The pistons run in a phase angle Ph=0.5π

When the pressure is reaching the maximum, the system volume is at its minimum, piston 2 (corresponding to velocity2) just finished its compression but piston 1 is already on the way to expansion. In this case, the trailing piston (piston 2) always compresses at high pressure and expands at low pressure while the leading piston (piston 1) is opposite, which results in the average temperature on the side of the trailing piston to be higher than the other side due to the additional work done by the trailing piston.

Table 8.3 The maximum averaged temperature increases at cyclic steady state (CO_2, T_0=30˚C; T_c=4s; Stroke1=Stroke2=0~100mm; $P_{0\_0.5\pi}$=1.15bar, $P_{0\_0.5\pi}$=1.41bar, P_{0_π}=1.47bar, $P_{0\_1.5\pi}$=1.43bar)

	Ph=0 (˚C/bar)	Ph=0.5 π (˚C/bar)	Ph=π (˚C/bar)	Ph=1.5 π (˚C/bar)
T1	6.68	6.31	4.62	4.61
T2	6.89	6.19	4.63	4.59
T3	6.56	4.58	4.93	8.47
T4	6.67	4.46	4.95	8.78

The experiments with different phase angles have been run and their maximum averaged temperature increases at cyclic steady state are shown in Table 8.3.

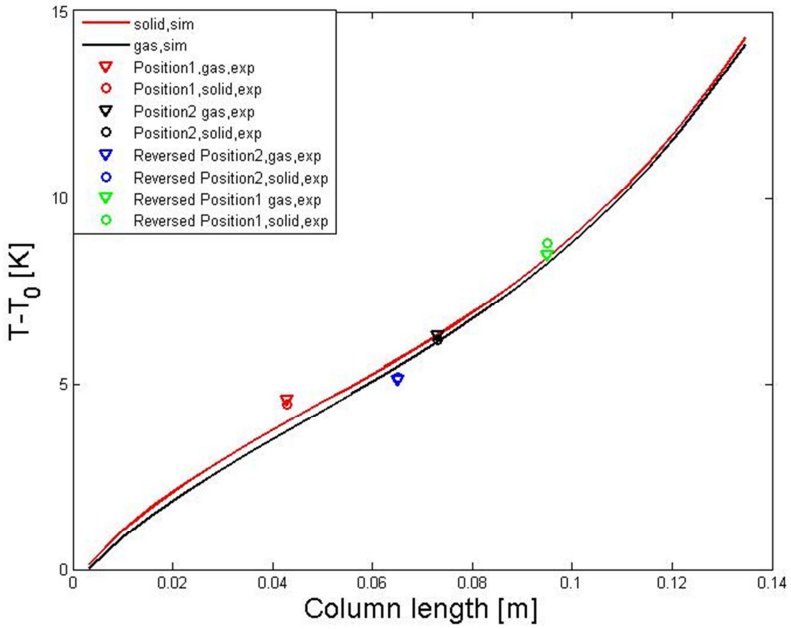

Figure 8.13 Temperature gradient along the column

In Table 8.3, the experiments are run in the same conditions except for their phase angles. So the experiment of Ph=0.5π and Ph=1.5π are the same but with pistons switched. This allows to have the temperatures of four positions. It is helpful to predict better temperature gradient along the column, see. The temperature gradient in Figure 8.13 is obtained when cyclic equilibrium between the effects of piston friction and heat transfer is achieved. This corresponds to a state where the experiment has been run for more than 4 hours. The gradient builds up over time. In the case of Ph = 0, it is a symmetric run, thus the temperature at each side of the column is very close. It is a similar case to the run of Ph = π.

8.2.5 Effect of changing the initial temperature

According to the adsorption isotherms of CO_2 on zeolite 13X, the adsorption capacity will be reduced as the system temperature increases. Experiments at 30°C and 100°C have been run

to show this effect. To maximise this phenomenon, both experiments were run with Ph = 0, resulting in the maximum pressure swing amplitudes.

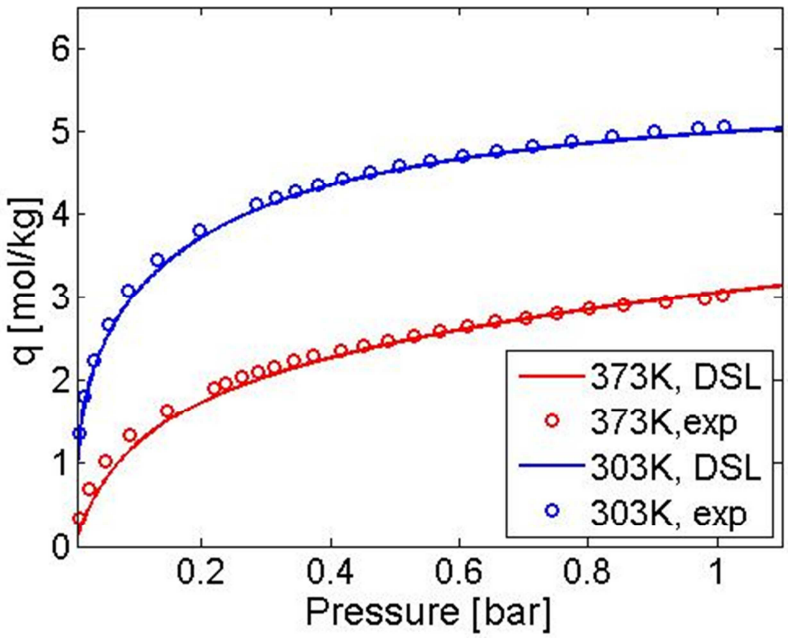

Figure 8.14 CO_2 adsorption isotherms on zeolite 13X at 373K and 303K. Shown are the experimental data points and the dual-site Langmuir fit.

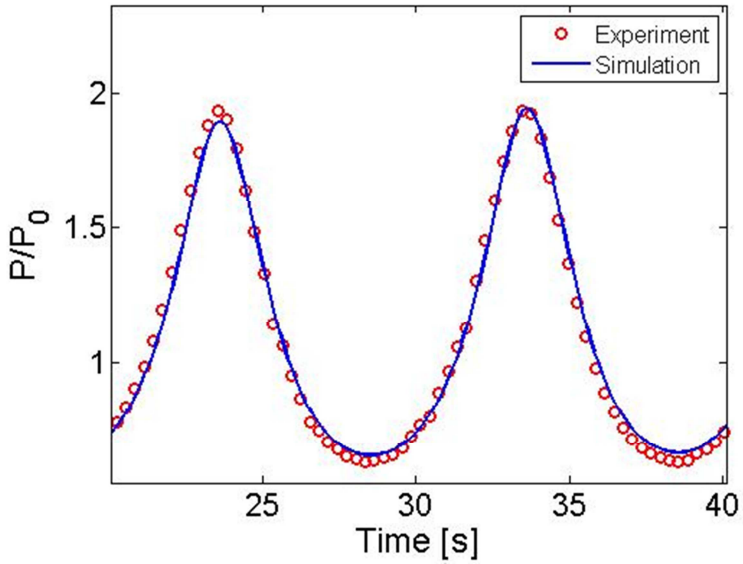

Figure 8.15 The pressure response at T=100°C (CO_2, T_0=100˚C; Phase angle=0.5π; T_c=10s; Stroke1=Stroke2=0~100mm; P_0=1.25bar)

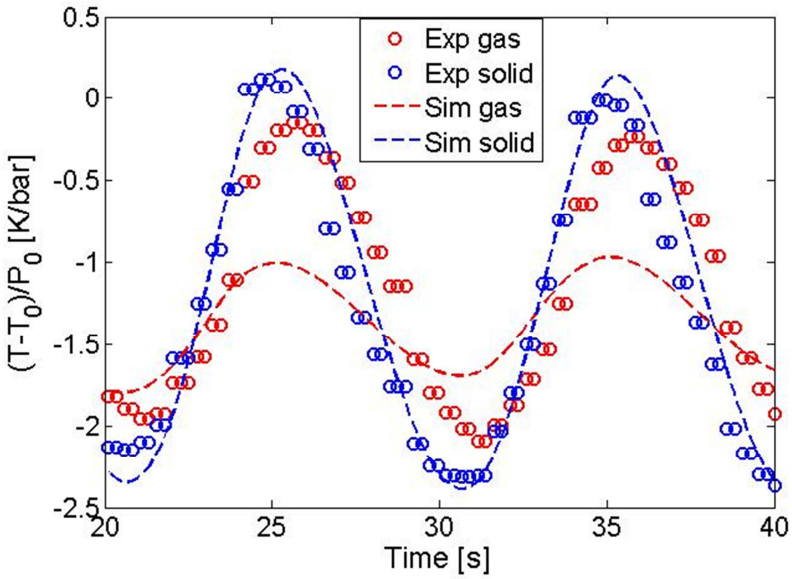

Figure 8.16 The temperature response at T=100°C (CO_2, T_0=100˚C; Phase angle=0.5π; T_c=10s; Stroke1=Stroke2=0~100mm; P_0=1.25bar)

Figure 8.1, Figure 8.2, Figure 8.15 and Figure 8.16 are under the same conditions except for their initial temperatures. The pressure and temperature for these two experiments are well predicted. In Figure 8.16, the solid temperature swing amplitude is 2.28K/bar while it is 2.98 K/bar in Figure 8.2. The temperature swing amplitude at 100˚C is lower than that at 30˚C, which agrees with the trend of their isotherms shown in Figure 8.14. However, for different initial temperatures, the isotherm is not the only factor contributing to the different temperature swing amplitudes. At a higher initial temperature, the thermal conductivity and the dynamic viscosity of the gas are higher. According to Eq.8.10 to Eq.8.16, the heat transfer coefficients for both the pellet and the column wall are higher, for a higher initial temperature. Thus, the temperature swing amplitude at a higher initial temperature is reduced by the heat transfer more than at a lower initial temperature. The average temperature for an experiment with an initial temperature of 100°C is lower than the initial temperature, which is due to the heat transfer between the piston shafts and the outside of the oven. If there is a large difference between the system temperature and room temperature, the heat exchange between the inside and the outside of the oven needs to be taken into account, because the shaft of the pistons are cooled down when they move out of the oven (expansion) and heated up when they move in (compression). In addition, the air outside the oven may come into the piston

cylinder when the pistons compress (Figure 8.17). The temperature around that area is then affected.

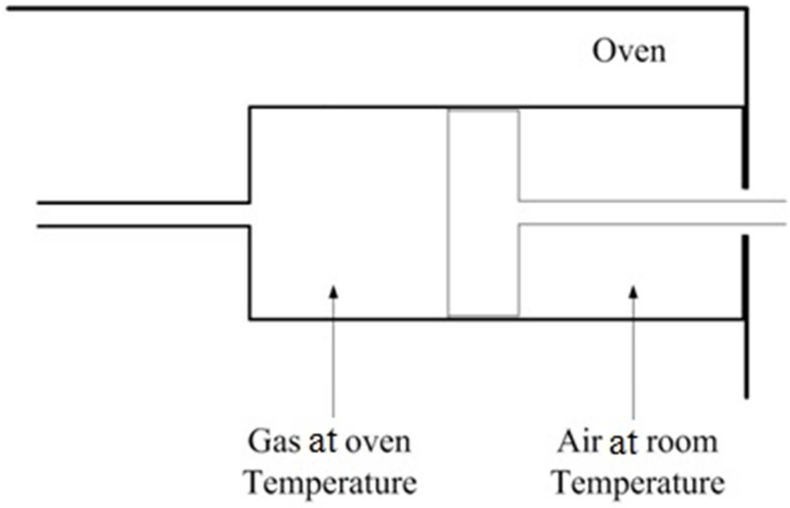

Figure 8.17 The temperature in the piston cylinder may be affected by the room temperature

8.2.6 Pressure drop

The pressure drop is mainly affected by the flow velocity, the density and viscosity of the gas. Figure 8.18 shows the pressure drop of a CO_2 run in the packed column for two different cycle times and a phase offset of 0.5π.

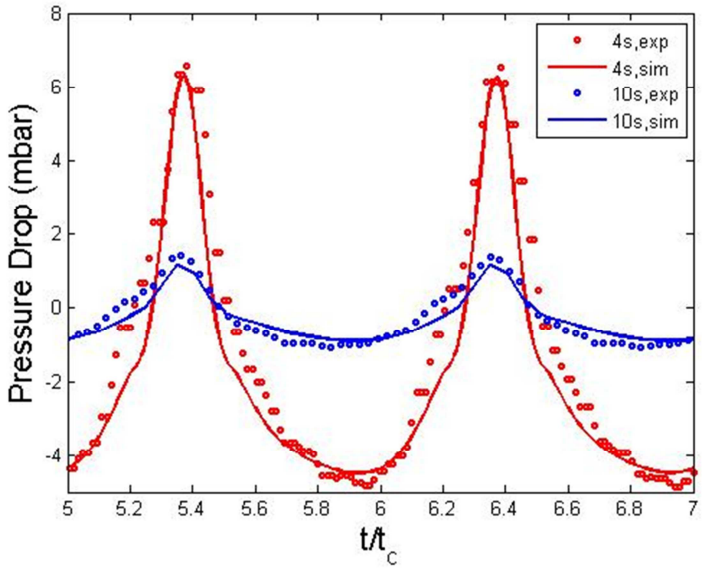

Figure 8.18 The pressure drop across the column for a fast and a slow cycle (CO_2, T_0=30˚C; Phase angle=0.5π; Stroke1=Stroke2=0~100mm; P_{0_10s}=1.22bar, P_{0_4s}=1.41bar)

From this figure, it is clearly seen that the pressure drop of fast cycles is significantly larger than that of slower cycles in agreement with the dependency on the fluid velocity, see Eq.4.10. Furthermore, both the pressure drop and the absolute pressure are following an asymmetric profile. Comparing the experimental pressure drop to the simulated result, they are in a good agreement. Thus the Ergun pressure drop equation represents with sufficient accuracy the description of the pressure drop in the DP-PSA system even with reversing flows and for an adsorbing gas.

8.3 Experiments with mixed gases

8.3.1 Prediction of the mixture gas experiments

In the pure gas experiments all the model parameters are obtained. Therefore, it is possible to predict now the dynamic response of experiments with mixed gases. In the simulations of mixed gases, the initial mole fraction of each gas at equilibrium is used to initialise the system.

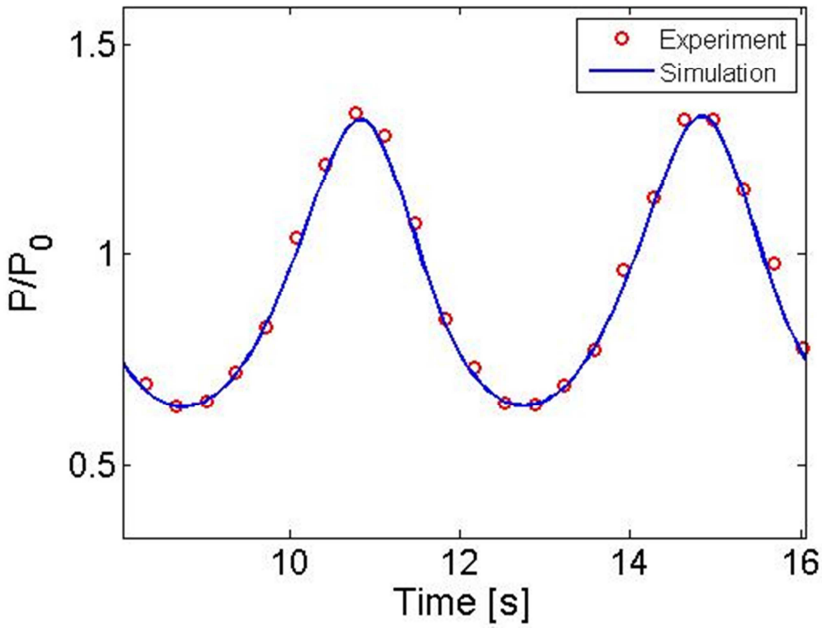

Figure 8.19 The pressure response of an experiment with a mixture gas, CO_2:N_2=1:1 (T_0=30˚C; Phase angle=1.5π; T_c=4s; Stroke1=0~25mm； Stroke2=0~100mm; P_0=0.54bar)

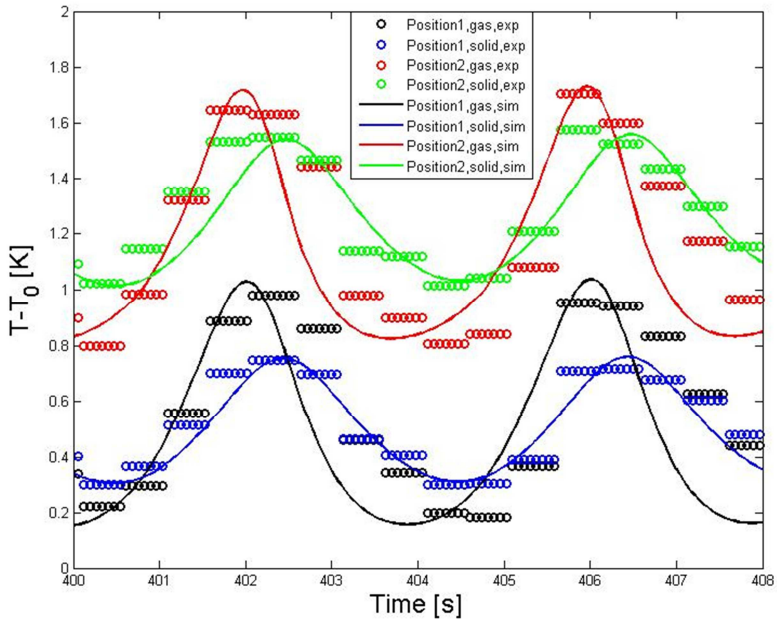

Figure 8.20 The temperature response of an experiment with a mixture gas, CO_2:N_2=1:1 (T_0=30˚C; Phase angle=1.5π; T_c=4s; Stroke1=0~25mm； Stroke2=0~100mm; P_0=0.54bar)

The experimental and the simulation results are compared for model validation. A representative pressure prediction is shown in Figure 8.19. It is clearly seen from the figure that the simulated pressure agrees well with the experimental pressure. The corresponding temperature response of this experiment can be found in Figure 8.20. In the figure, the gas temperature swing amplitude is higher than the solid, which is different to the pure CO_2 case. This is a clear evidence of mass transfer resistance in the fast cycle runs. This is to be expected since in mixed gas experiments molecular diffusion is now an important contribution in the effective macropore diffusivity.

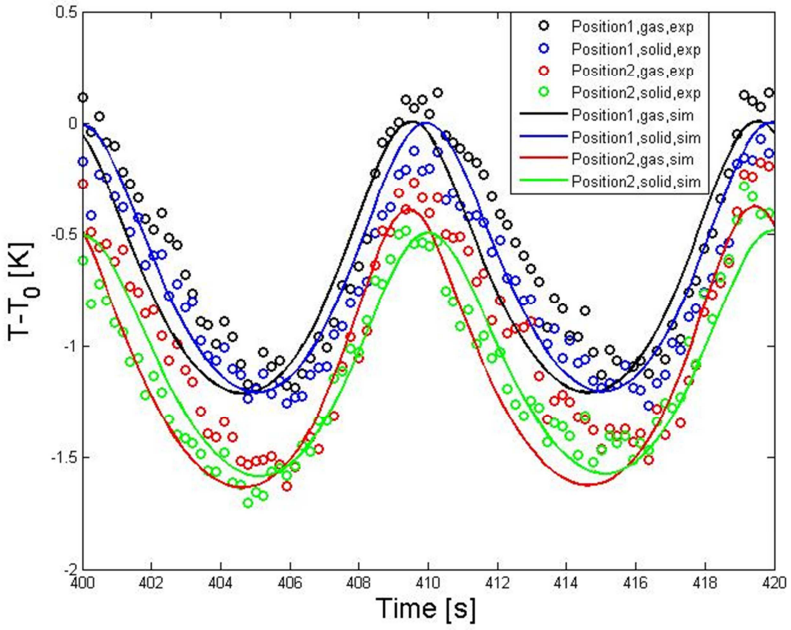

Figure 8.21 Temperature response of an experiment with a mixture gas, CO_2:N_2=1:4 (T_0=30˚C; Phase angle=1.5π; T_c=4s; Stroke1=0~50mm； Stroke2=0~100mm; P_0=1.41bar)

To further confirm the prediction, some experiments with different compositions were carried out. A representative temperature prediction is shown in Figure 8.21. In both Figure 8.20 and Figure 8.21, the predicted temperature swing amplitudes agree with the experimental results. The average temperatures at two positions are different in both Figure 8.20 and Figure 8.21. The reason here is not only due to the work done by the pistons. In the mixture gas experiment, the gas concentration along the column varies depending on the configuration of the pistons. Different concentrations along the column will correspond to a difference in the extent of adsorption and desorption and result in a temperature gradient.

8.3.2 Separation process in the mixed gas experiments

In the mixed gas experiments, there is a concentration difference of each gas along the column. As the system approaches cyclic steady state the difference tends to its maximum resulting in a separation of the binary mixture. The separation effect depends mainly on the phase angle and the stroke length ratio between the two pistons. Here, consider the cases of Ph=0.5π and Ph=1.5π as examples. To understand this process better, the flow rate and the pressure for the two experiments are simulated and shown in Figure 8.22 (Ph=1.5π) and Figure 8.23 (Ph=0.5π).

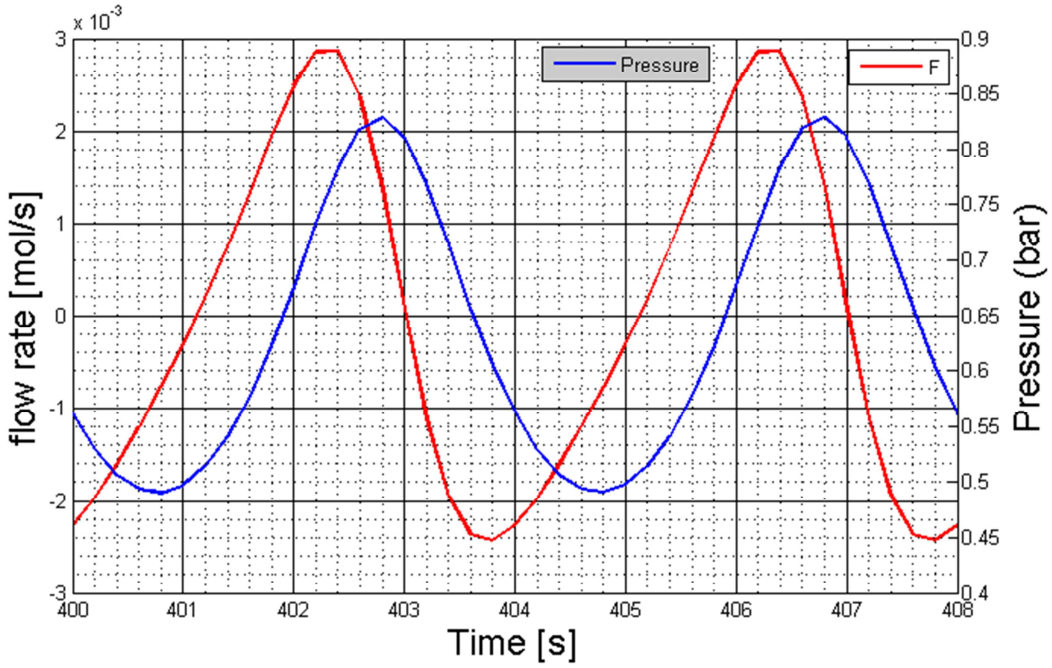

Figure 8.22 Flow rate and pressure in the column simulation, Phase angle=1.5π (CO_2:N_2=1:1, T_0=30˚C; T_c=4s; Stroke1=0~25mm; Stroke2=0~100mm; P_0=0.54bar)

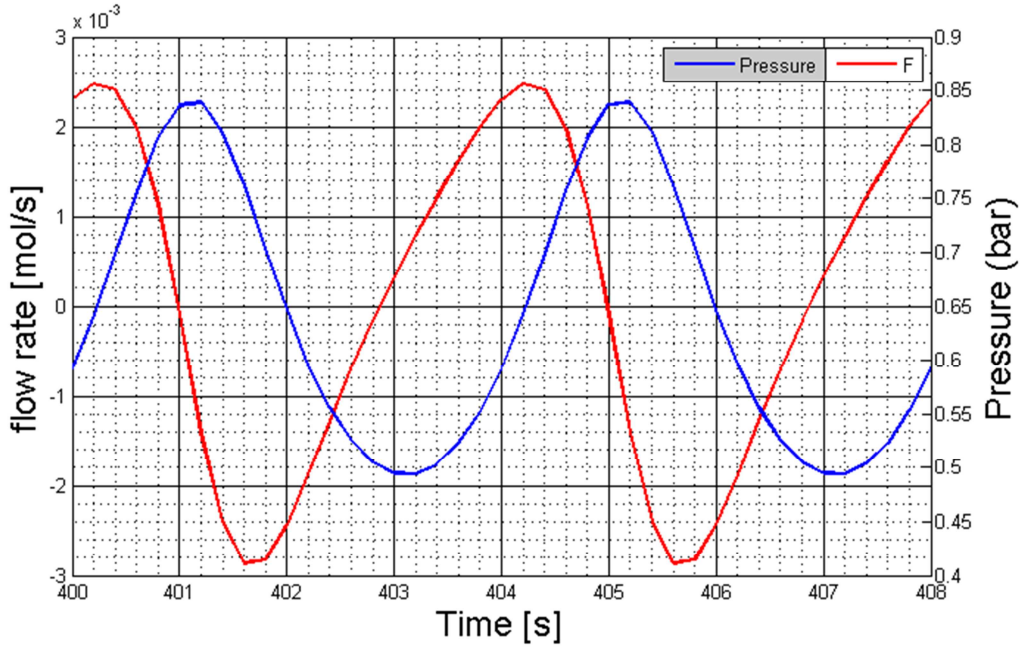

Figure 8.23 Flow rate and pressure in the column simulation, Phase angle=0.5π (CO2:N2=1:1, T_0=30˚C; T_c=4s; Stroke1=0~25mm; Stroke2=0~100mm; P0=0.54bar)

In the run with Ph=0.5π, the piston with longer stroke length (piston1) leads by 0.5π, so if the cycle time is 4s, the lead time is 1s. Oppositely, the piston with shorter stroke length (piston2)

leads by 0.5π in the case of Ph=1.5π. The positive flow direction is defined as the gas moving from piston 1 (longer stroke length) to piston 2 (shorter stroke length). In the case of Ph=1.5π (Figure 8.22), it is clearly seen that the maximum pressure, where the maximum CO_2 is adsorbed, occurs during the positive flow with a flow rate 1.2×10^{-3} mol/s. The gas rich in N_2 flows into piston 2. At the minimum pressure, where the maximum amount of CO_2 is released, the gas rich in CO_2 flows from piston 2 to piston 1 with a flow rate -0.9×10^{-3} mol/s. Thus, more CO_2 is collected in piston 1. By repeating this cycle, the concentration difference along the column is increased up to cyclic steady state. CO_2 is accumulated towards piston 1 and most of N_2 moves towards piston 2. Figure 8.24 shows a simulated CO_2 mole fraction profile along the column during 17 cycle runs. After 17 cycles, it is clearly seen there is a mole fraction difference of CO_2 at the ends of the column.

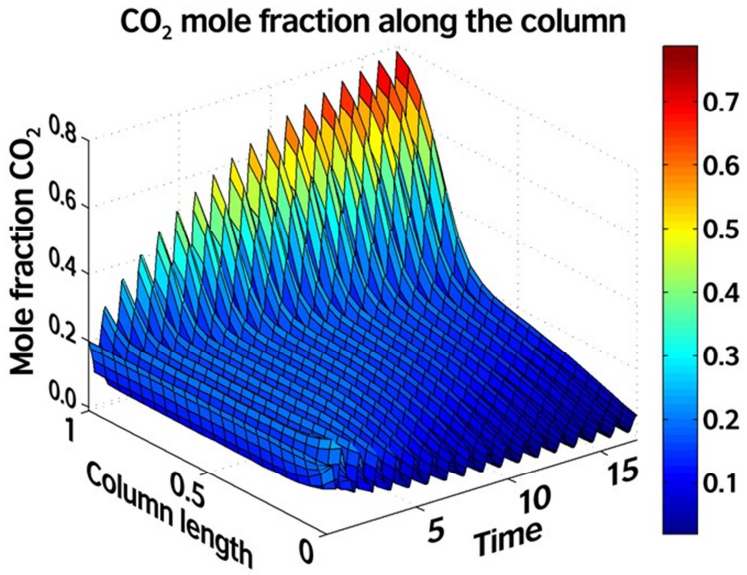

Figure 8.24 Simulation of a test case starting with a uniform CO_2/N_2 mixture and inducing a concentration gradient along the column length

In the case of Ph=0.5π (Figure 8.23), the maximum pressure occurs at -0.3×10^{-3} mol/s and the minimum pressure occurs at 0.4×10^{-3} mol/s. These two flow rates are lower than in the case of Ph=1.5π (Figure 8.22), which means that for Ph=0.5π there would be a lower concentration difference across the column. In addition, the flow direction of the case of Ph=0.5π at the time of peak pressures are opposite to the case with Ph=1.5π.Thus, the CO_2 and N_2 are concentrated in the opposite side of the column. In this case study, it is obvious that the phase angle between the two pistons is a variable that determines the separation result.

Since the stroke-length ratio is another factor to determine the flow rate, its influence to the separation process can be explained in a similar way. Therefore, more experiments with different configurations of the pistons can be run and their separation efficiency can be compared.

8.4 Conclusions

In this chapter, the adsorbing column of the dual-piston pressure swing system is fully packed with zeolite 13X. Different gases were run in this closed system with various configurations. The pressure and temperature inside the system are monitored. The LDF coefficient of the model is a combination of the viscous flow, Knudsen diffusivity and molecular diffusivity. The heat transfer coefficient, the axial dispersion coefficient and the axial thermal coefficient are also predicted. Their correlations were validated by simulating the experimental data for both pure component and mixture experiments. The pressure and temperature performance are compared by only changing one running condition. This allows to predict the binary experiments and to observe the following:

1. Due to adsorption, the pressure swing amplitude of pure CO_2 is lower than N_2 and He and the peak pressure of CO_2 occurs ahead of N_2 and He.

2. Variation of the cycle time allows to move from equilibrium control to kinetic control and characterise mass and heat transfer. In the fast cycle runs, i.e. T_c=2s, the temperature of the gas and the solid may swing in a very different amplitude because the heat has not enough time to be transferred. The solid and the gas temperature swing amplitudes tend to converge as the cycle time increases.

3. For the strong adsorbing experiments, the pressure swings in a lower amplitude in the slow cycle runs than in the fast cycle runs, because there is more time to approach equilibrium in the slow cycle runs.

4. In the pure He experiment, the solid temperature swings much less than the gas temperature. Longer cycle time results in less difference between gas and solid temperature.

5. With different configurations of the phase angle between the two pistons, the temperature along the column is different. The asymmetric configuration leads to a temperature gradient.

6. The pressure drop is well predicted by the Ergun equation.

7. If the initial temperature is changed, the change of the pressure and temperature performance is a combination result of the isotherm and heat transfer.

8. In the mixture experiment, the separation process is explained by the relationship between the pressure and the flow rate of the gas. The stroke length ratio and the phase angle between two pistons affect the separation efficiency.

9. Single Pellet Experiments by DP-PSA

9.1 Introduction

After the modification of the DP-PSA system to include temperature measurements, it became apparent that a further new experiment could be performed. This was achieved by removing all the pellets from the column except for the two pellets attached to the thermocouples. Since the pellet is very small compared to the bed, the void fraction of the bed is almost 99.9%. Both single component and binary experiments can be performed. Here adsorption will have a negligible effect on the total pressure and gas composition. The moving pistons ensure that even for the binary experiments, external mass transfer resistances are minimised. Therefore when using pure components one can test the heat transfer model to an individual particle and in the low pressure region the effect of Knudsen diffusion on the mass transfer resistance. For the binary systems it is possible to test the effect of combined Knudsen and macropore diffusion as well as the heat transfer rates in the mixture. In this configuration the system is similar to a thermal frequency response system (Grenier et al. 1999; Sun et al. 1993) operated under non-linear conditions. The advantage of the dual piston configuration is that it allows a high gas flow over the particles, which would not be possible with a single piston configuration.

In this chapter, the results of the first experiments with single pellets in the DP-PSA are shown. The gases used are CO_2, N_2, He and mixtures of CO_2 and N_2.

9.2 Experiment

9.2.1 Parameters for the model

To predict the temperature of the gas, the heat transfer mechanism must be considered, i.e. exchange of heat between the gas and the column wall, as well as the heat transfer in the pipes connecting the piston cylinder and the column.

A few experiments with different gases under different conditions were carried out. To simplify the analysis, the temperatures in the He experiments were studied since this case does not involve any adsorption. The gas temperature can be represented correctly if a heat transfer coefficient between the gas and the thermocouple is taken into account. Thus, the Reynolds numbers and the Nusselt numbers are finally expressed as below

For the pellet: $$\mathrm{Re}_p = \frac{MW_i \times F \times 2 \times R_p}{\varepsilon \times \pi \times R_c^{\,2} \times \mu} \qquad \text{Eq.9.1}$$

For the column: $$\mathrm{Re}_c = \frac{MW_i \times F \times 2 \times R_c}{\varepsilon \times \pi \times R_c^{\,2} \times \mu} \qquad \text{Eq.9.2}$$

For the pipes: $$\mathrm{Re}_p = \frac{MW_i \times F \times 2 \times R_{pipe}}{\varepsilon \times \pi \times R_{pipe}^{\,2} \times \mu} \qquad \text{Eq.9.3}$$

For the pellet: $$Nu_p = 2 + \left(0.4 \times \mathrm{Re}_p^{\,1/2} + 0.06 \times \mathrm{Re}_p^{\,2/3}\right) \times \mathrm{Pr}^{0.4} \qquad \text{Eq.9.4}$$

For the column: $$Nu_c = 1.86 + \left(Re_c \times Pr \times \frac{2 \times R_c}{L} \right)^{1/3} \qquad \text{Eq.9.5}$$

For the pipes: $$Nu_{pipe} = 1.86 + \left(\mathrm{Re}_{pipe} \times \mathrm{Pr} \times \frac{2 \times R_{pipe}}{L_{pipe}} \right)^{1/3} \qquad \text{Eq.9.6}$$

The heat transfer coefficient is then

$$h_i = \frac{k \times Nu_i}{2 \times R_i} \qquad \text{Eq.9.7}$$

The isotherm and kinetic parameters are the same as in Chapter 8. The other parameters used in the simulation are also presented in Chapter 2 and Chapter 7.

After the pure gas experiments, mixtures of CO_2 and N_2 were run to confirm the validation of the parameters.

9.2.2 Experiment with different gases

When the system contains only two pellets the system pressure practically depends only on the piston position, i.e. system volume, and gas temperature. A few experiments with different gases are carried out. The model can predict the pressure very well. Figure 9.1 shows a representative prediction.

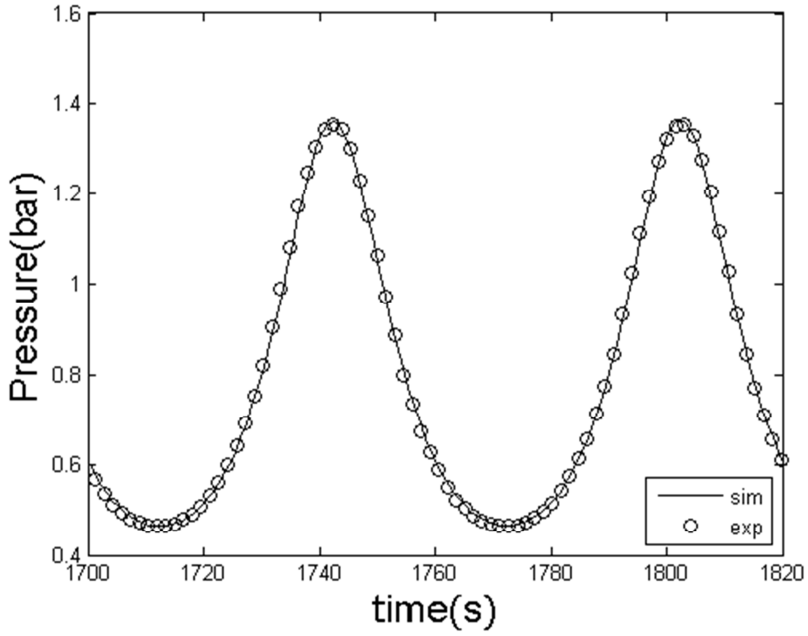

Figure 9.1 Simulated pressure and experimental pressure in single pellet experiment (CO_2; T_0=30˚C; T_c=60s; Phase angle=0; Stroke1=Stroke2=0~75mm; P_0=0.76bar)

The gas and solid temperature responses are compared for different pure gases in Figure 9.2.

a)

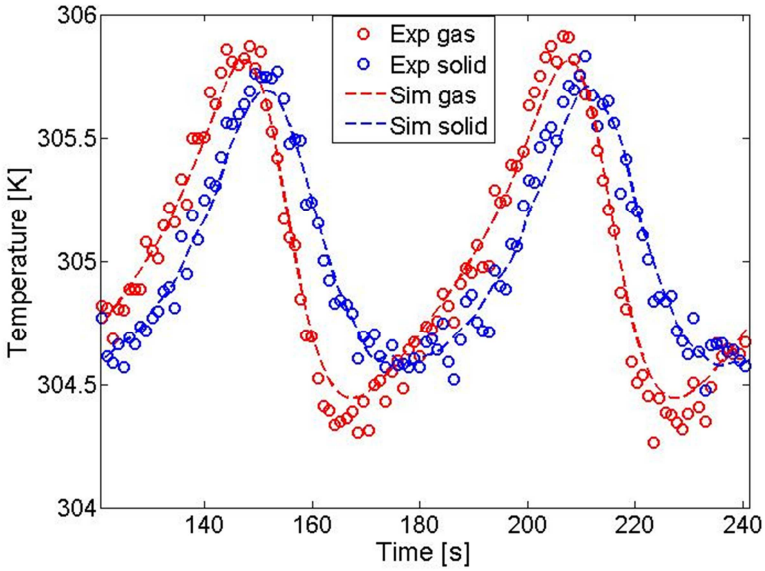
Exp gas
Exp solid
Sim gas
Sim solid
Temperature [K]
Time [s]
306
305.5
305
304.5
304
140
160
180
200
220
240

b)

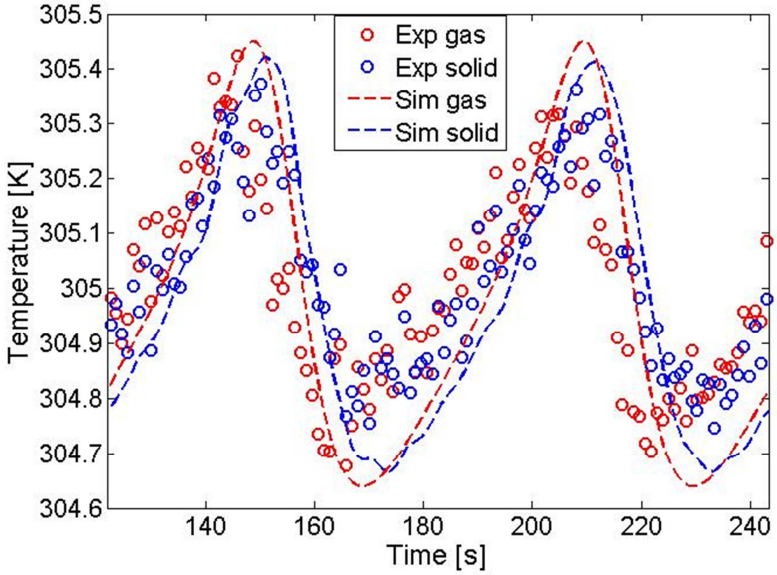
Exp gas
Exp solid
Sim gas
Sim solid
Temperature [K]
Time [s]
305.5
305.4
305.3
305.2
305.1
305
304.9
304.8
304.7
304.6
140
160
180
200
220
240

c)

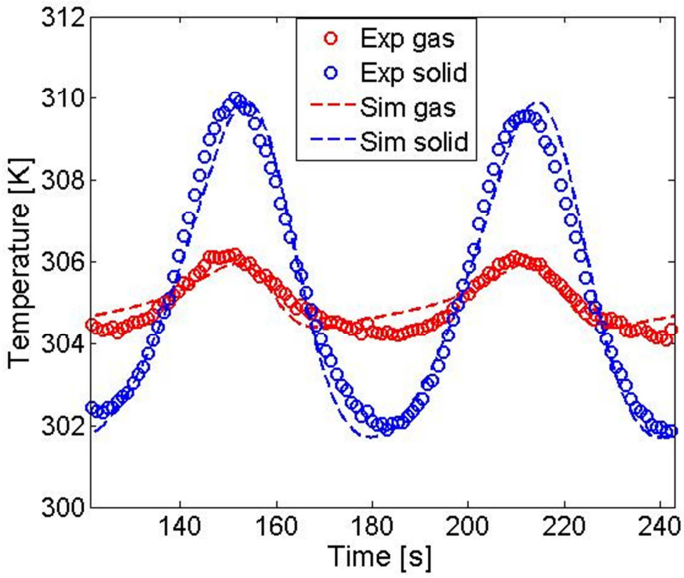

Figure 9.2 Gas and adsorbent solid temperature profiles in single pellet experiments for N_2 (a) (N_2; T_0=30˚C; T_c=60s; Phase angle=0; Stroke1=Stroke2=0~75mm; P_0=0.78bar), He (b) (He; T_0=30˚C; T_c=60s; Phase angle=0; Stroke1=Stroke2=0~75mm; P_0=0.71bar) and CO_2 (c) (CO_2; T_0=30˚C; T_c=60s; Phase angle=0; Stroke1=Stroke2=0~75mm; P_0=0.76bar)

For the helium case Figure 9.2 (b), both solid and gas temperatures swing with a very small amplitude. These temperature changes are mainly due to compression and expansion of the gas. In the experiment of nitrogen with similar pressure conditions, the gas is not strongly adsorbed. Part of the heat generated in the system comes from the compression and expansion, but in this case there is also an additional contribution from the heat of adsorption. Thus, the amplitude of the temperature change in the nitrogen experiment (Figure 9.2 (a)) is higher than that in the helium experiment. If the adsorption is stronger, the heat effect on the solid temperature is more obvious. This is clearly shown in the CO_2 experiment (Figure 9.2 (c)). Here the solid temperature is higher than that of the gas, because most of the heat is generated in the adsorption/desorption process. One important point to consider when running the single pellet experiments is that in this case the results will be very sensitive to any leakage of water into the system. This may explain the over-prediction of the temperature swing of the model. To confirm this point, the same experiment was repeated while the gas was left in the system for three days. The result is shown in Figure 9.3. It is found the solid temperature swing amplitude is even lower. After repeated test, it is suggested the single pellet experiments for CO_2 should be completed within one day and regeneration of the sample between tests is very important.

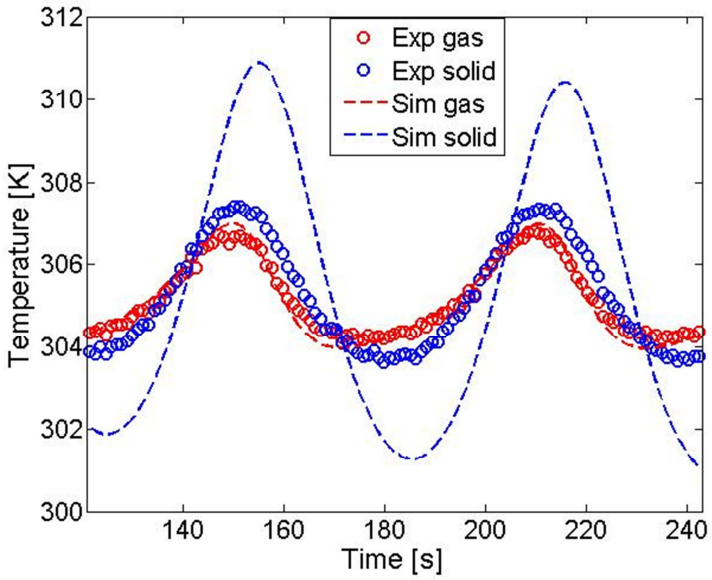

Figure 9.3 The experiment was run after three days of dosing (CO_2; T_0=30˚C; T_c=60s; Phase angle=0; Stroke1=Stroke2=0~75mm; P_0=0.81bar)

Figure 9.4 shows an experiment with a binary gas mixture (CO_2:N_2=1:1). As expected the temperature swing amplitude for the mixture gas is between the results of the experiments with the pure gases. But it is interesting to note that there is a clear time-shift, i.e. the gas temperature leads that of the solid by about 6.8 s. This is due to macropore diffusion since in the case of a mixture we now have a larger mass transfer resistance. This time shift is well predicted by the model.

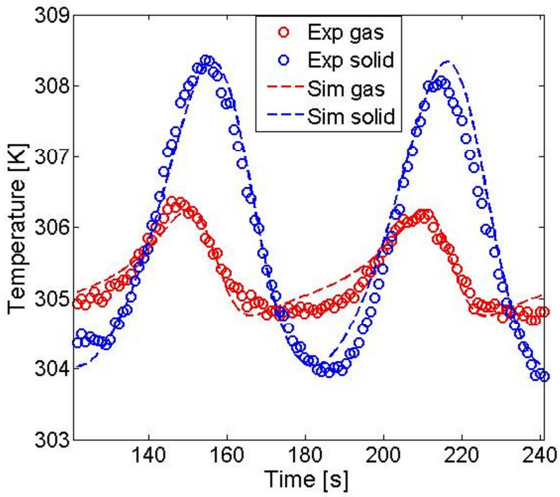

Figure 9.4 Gas and adsorbent solid temperature profiles for a mixture of carbon dioxide and nitrogen (CO_2:N_2=1:1; T_0=30˚C; T_c=60s; Phase angle=0; Stroke1=Stroke2=0~75mm; P_0=0.78bar)

9.2.3 Experiments with different initial temperatures

a)

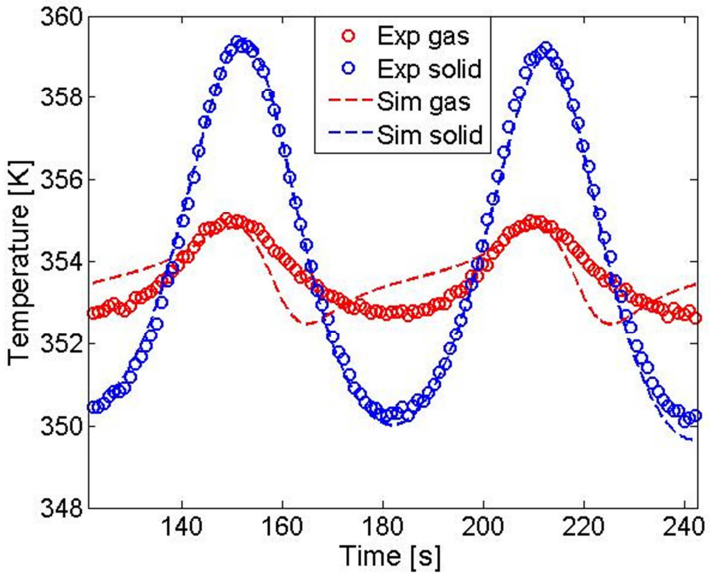

b)

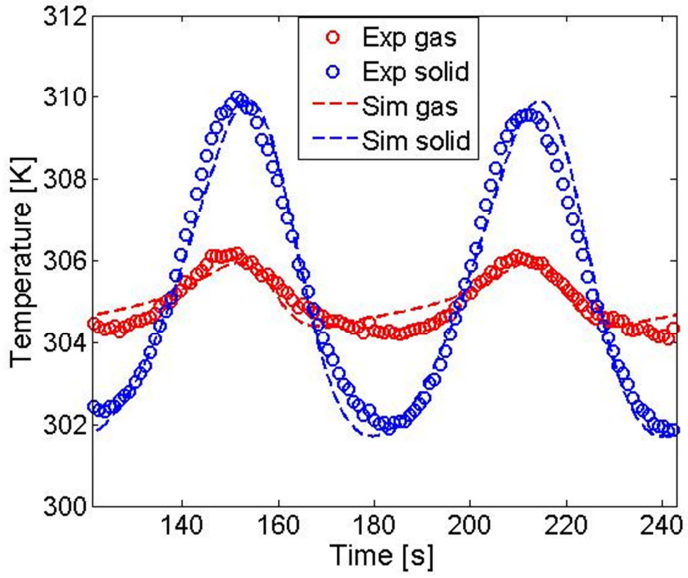

Figure 9.5 Gas and adsorbent solid temperature profiles for CO_2 experiments run at T_0=100˚C (a) (CO_2; T_0=100˚C; T_c=60s; Phase angle=0; Stroke1=Stroke2=0~75mm; P_0=1.01bar) and T_0=30˚C (b) (CO_2; T_0=30˚C; T_c=60s; Phase angle=0; Stroke1=Stroke2=0~75mm; P_0=0.76bar)

According to the adsorption isotherms of CO_2 on zeolite 13X, the adsorption capacity will be reduced as the system temperature increases. Since the large solid temperature swing amplitude in the CO_2 experiments is mainly due to adsorption, once the adsorption is reduced at higher temperature, the amplitude of the solid temperature swing amplitude should also be

decreased. We have run the CO_2 experiment both at T_0=100˚C (Figure 9.5 (a)) and T_0=30˚C (Figure 9.5 (b)).

When the initial temperature was increased from T_0=30˚C to T_0=100˚C, the solid temperature swing amplitude decreased from AT=11.7K/bar to AT=9K/bar. Because there are only two pellets, it does not affect the gas temperature much. But the heat transfer between piston shafts and the outside of the oven do contribute, as discussed in chapter 8.

9.2.4 Experiment run with different cycle times

The effect of the cycle time is significant. In Figure 9.2 (c) and Figure 9.6, it shows a representative comparison of the temperature performance with different cycle times, T_c=60s, T_c=30s, T_c=10s,.

a)

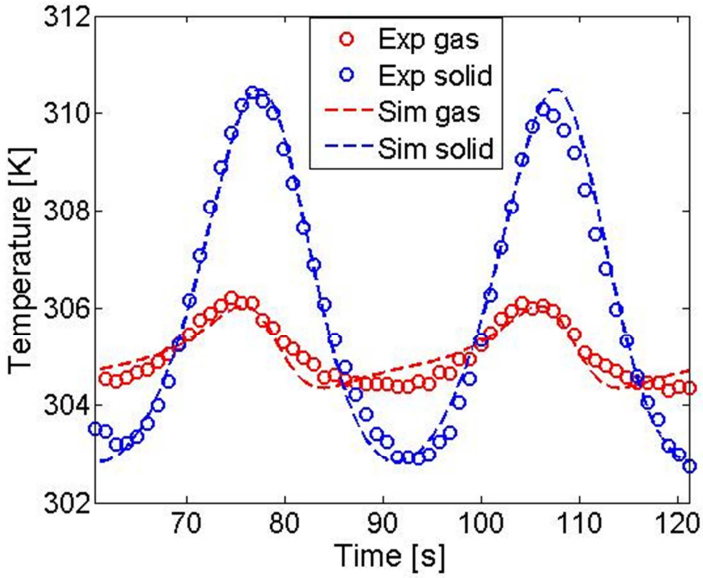

b)

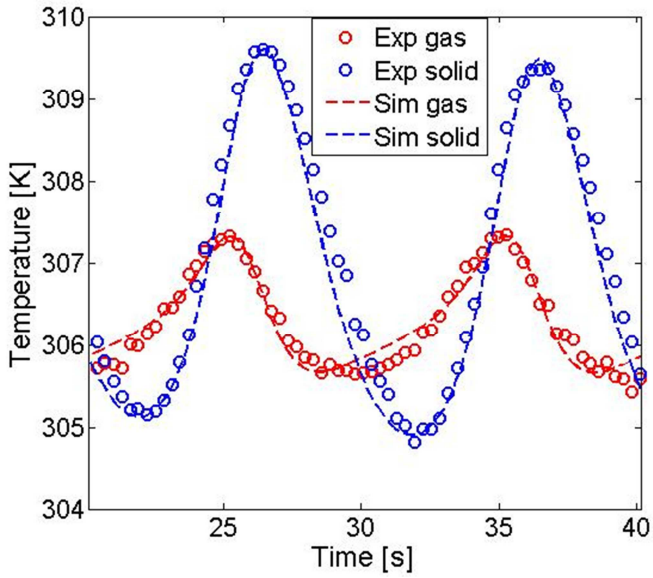

Figure 9.6 Gas and adsorbent solid temperature profiles for T_c =30s (a) (CO_2; T_0=30˚C; T_c=30s; Phase angle=0; Stroke1=Stroke2=0~75mm; P_0=0.72bar) T_c =10s (b) (CO_2; T_0=30˚C; T_c=10s; Phase angle=0; Stroke1=Stroke2=0~75mm; P_0=0.81bar)

As the cycle time decreases from T_c =60s to T_c =30s, we found that the temperature responses are similar. Thus, the experiment with T_c =60s can be assumed to be close to equilibrium with respect to mass transfer. For the fast cycle experiments, since there is not enough time to reach equilibrium, the amplitudes of the solid temperatures are reduced when the cycle time decreases. The gas temperature remains un-affected due to the small sample size.

Figure 9.7 (a) shows the temperature amplitudes for the He experiments as function of cycle time. Since there is no adsorption, the temperature changes are controlled by gas compression /expansion and heat exchange with the column wall and the pistons. Here the gas temperature swing increases because over a cycle the energy to compress and expand the gas remains the same, but the power increases with the inverse of the cycle time. The amplitude of the solid temperature does not change significantly with cycle time and this is due to the fact that the half cycle time is not long enough for the complete heat transfer between gas and solid.

a)

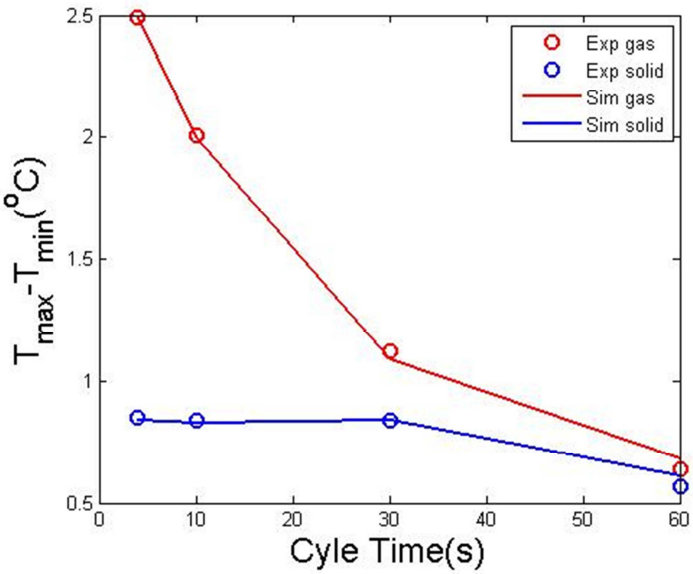
Exp gas
Exp solid
Sim gas
Sim solid
T_{max}-T_{min}(^{o}C)
Cyle Time(s)
2.5
2
1.5
1
0.5
0
10
20
30
40
50
60

b)

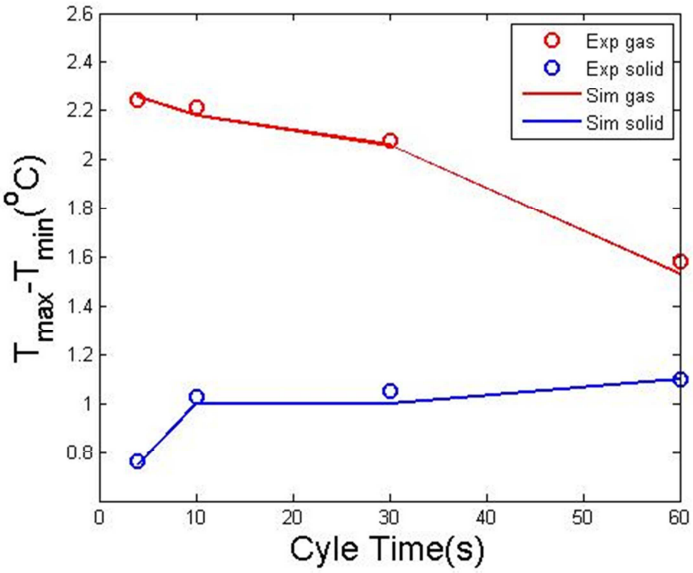
Exp gas
Exp solid
Sim gas
Sim solid
T_{max}-T_{min}(^{o}C)
Cyle Time(s)
2.6
2.4
2.2
2
1.8
1.6
1.4
1.2
1
0.8
0
10
20
30
40
50
60

c)

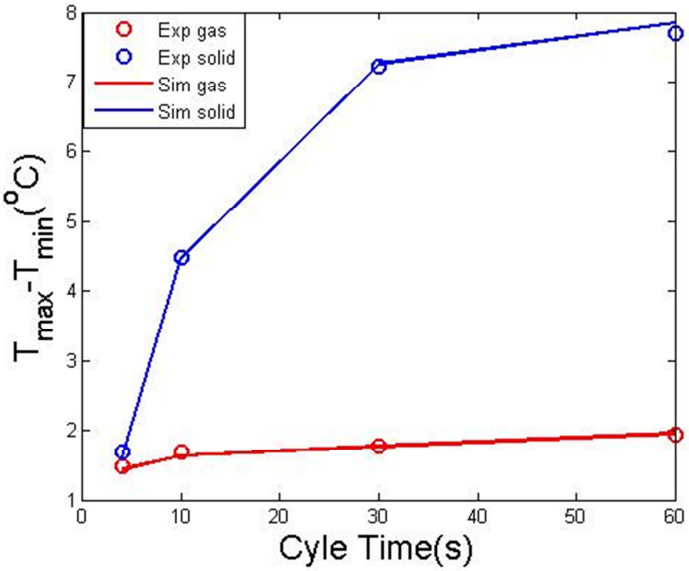

d)

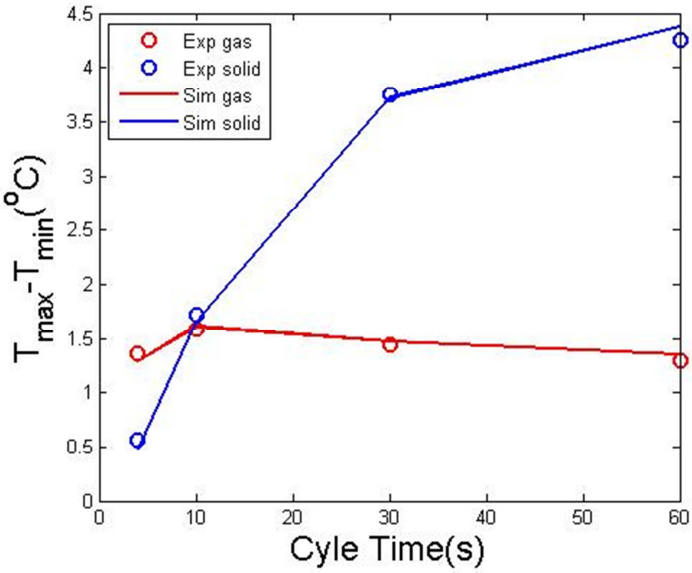

Figure 9.7 Gas and adsorbent solid temperature swing amplitudes for He (a) (He; T_0=30˚C; Phase angle=0; Stroke1=Stroke2=0~75mm; P_{0_4s}=0.63bar; P_{0_10s}=0.72bar; P_{0_30s}=0.66bar; P_{0_60s}=0.71bar); N_2 (b) (N_2; T_0=30˚C; Phase angle=0; Stroke1=Stroke2=0~75mm; P_{0_4s}=0.66bar; P_{0_10s}=0.68bar; P_{0_30s}=0.74bar; P_{0_60s}=0.78bar); CO_2 (c) (CO_2; T_0=30˚C; Phase angle=0; Stroke1=Stroke2=0~75mm; P_{0_4s}=0.73bar; P_{0_10s}=0.81bar; P_{0_30s}=0.72bar; P_{0_60s}=0.76bar); mixture of CO_2 and N_2 (d) (CO_2:N_2=1:1; T_0=30˚C; Phase angle=0; Stroke1=Stroke2=0~75mm; P_{0_4s}=0.67bar; P_{0_10s}=0.74bar; P_{0_30s}=0.69bar; P_{0_60s}=0.78bar)

The same experiments were repeated with N_2 and the temperature swing amplitudes are shown in Figure 9.7 (b). In the N_2 experiments, it is found the amplitude of the solid temperature is higher than in the helium experiment, which is a result of adsorption.

In the experiments of CO_2, there is an obvious contrast to the He and N_2 experiments. The solid and gas temperature swings diverge from each other. In addition to the compression and expansion of the gas, the heat caused by adsorption and desorption has a small effect also on the gas phase temperature and this may be the result of some radiative heat transfer from the pellet to the thermocouple in the gas.

The mixture gas experiments are shown in Figure 9.7 (d), the gas and solid temperature swing amplitudes responses are similar to the CO_2 curves in slow cycle runs, i.e. T_c=30s, T_c=60s. It is interesting to note that the solid amplitude is lower than the gas amplitude in the fast cycle runs, i.e. T_c=4s. This is a result of the mass transfer resistance.

9.2.5 Experiments run with different piston stroke lengths

a)

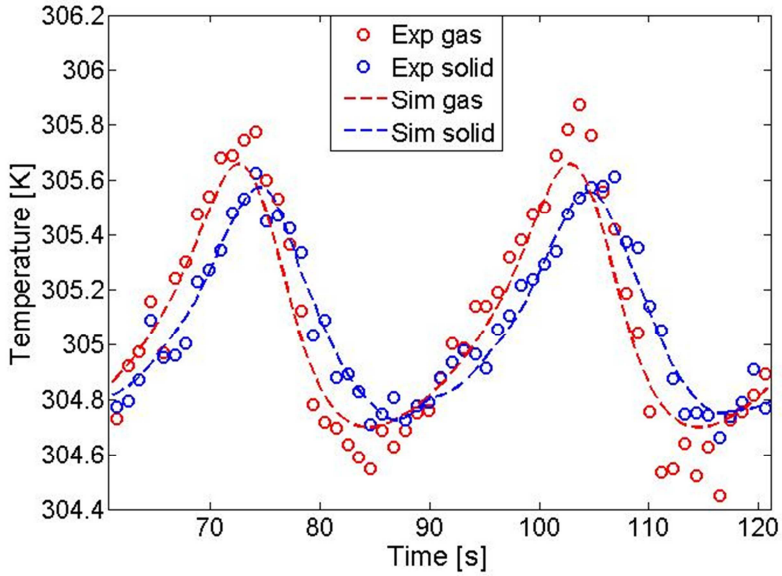

b)

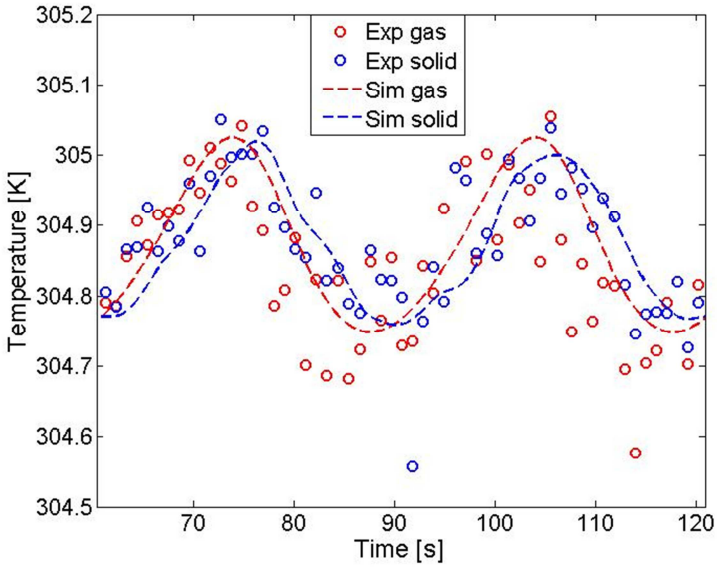

c)

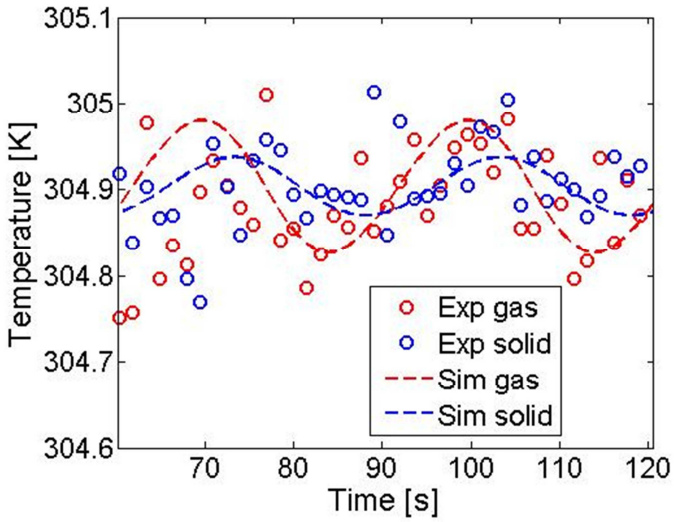

Figure 9.8 The He experiment with different stroke lengths: 75 mm (a) (He; T_0=30˚C; T_c=30s; Phase angle=0; Stroke1=Stroke2=0~75mm; P_0=0.66bar); 40mm (b) (He; T_0=30˚C; T_c=30s; Phase angle=0; Stroke1=Stroke2=0~40mm; P_0=0.78bar); 10 mm (c) (He; T_0=30˚C; T_c=30s; Phase angle=0; Stroke1=Stroke2=0~10mm; P_0=0.79bar)

In the single pellet experiments the stroke length determines the volume of the system and thus the pressure swing. The helium experiments of stroke length 10 mm, 40 mm and 75 mm were run and shown in Figure 9.8.

In the experiment of stroke length 10mm, the pressure variation is so small that the temperature response cannot be identified clearly by the thermocouples (Figure 9.8 (c)). In

Figure 9.8 (a) and (b), the gas temperatures are all higher than the solid temperatures as expected.

The gas and solid temperatures for CO_2 with the same conditions of the helium runs are shown below.

a)

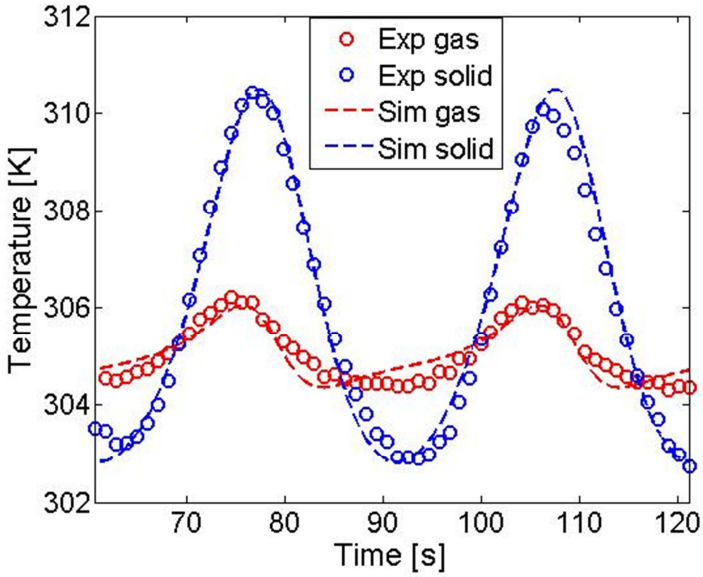

b)

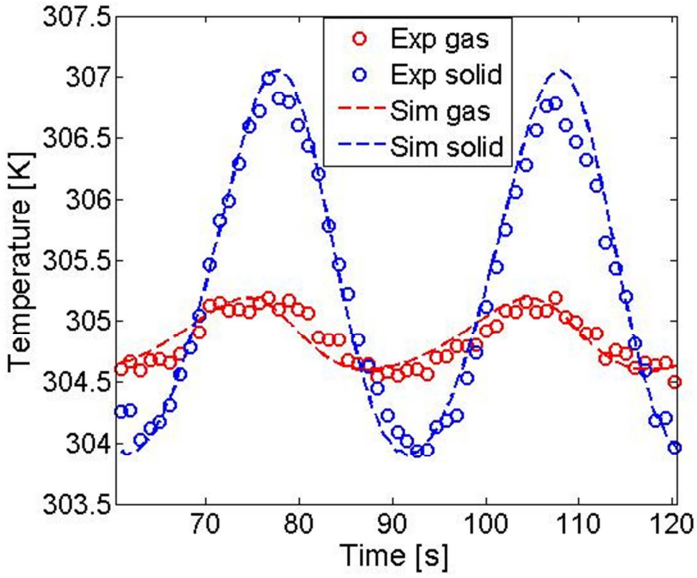

c)

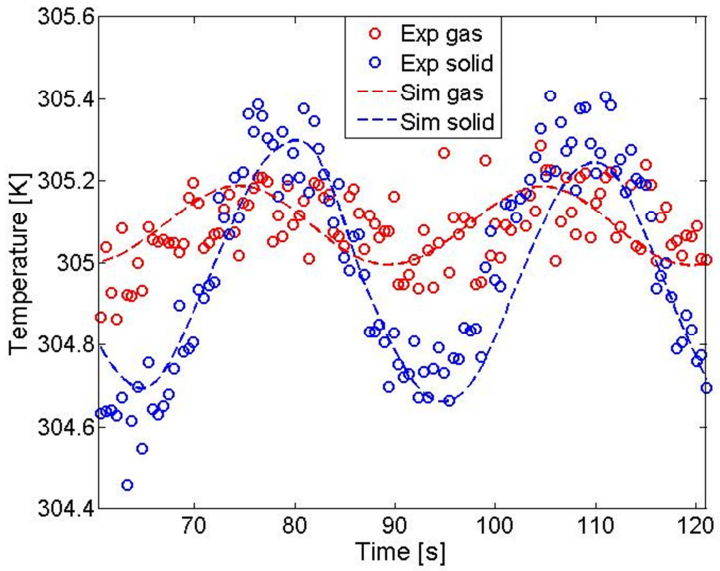

Figure 9.9 The CO_2 experiment with different stroke lengths: 75mm (a) (CO_2; T_0=30˚C; T_c=30s; Phase angle=0; Stroke1=Stroke2=0~75mm; P_0=0.72bar); 40mm (b) (CO_2; T_0=30˚C; T_c=30s; Phase angle=0; Stroke1=Stroke2=0~40mm; P_0=0.78bar); 10mm (c) (CO_2; T_0=30˚C; T_c=30s; Phase angle=0; Stroke1=Stroke2=0~10mm; P_0=0.76bar)

As the stroke length decreases, the pressure and temperature swing amplitudes are decreased correspondingly. For the short stroke length experiments, the adsorbed amount is proportional to the pressure swings (i.e. there is linearity) and the solid temperatures are directly related to the pressure variation.

9.3 Conclusions

In this chapter the experiments were run with DP-PSA system with only two pellets in the column to study the single pellet heat and mass transfer kinetics. Since the pellet is very small compared to the bed, the void fraction of the bed is large. In the simulation, only the heat transfer coefficient is redefined here, while the other parameters for the model were kept the same as Chapter 8. The experimental procedure was the same as described in Chapter 8. First, the pure gas experiments were run then the mixture gas experiments. The predictions of the model are in excellent agreement with the experimental results providing further validation of the approach. Their pressure and temperature performance are compared by only changing one experimental condition. It is found that the temperature swing amplitude is very sensitive to the adsorption. For different gases and different piston conditions, the gas and the solid temperature swing amplitude were compared. The relationship between the gas and the solid

temperature is quite different and gives different trends for a series of experiments with different cycle times. The detailed implications of this phenomenon should be considered in future work.

Chapter 10 Conclusions and recommendations for further work

The work presented in this thesis focuses on the development of a novel apparatus, named DP-PSA, which is aimed at the characterisation of adsorbents. Compared to classic PSA devices, the DP-PSA is a closed system where pistons moving in cylinders at each end of the adsorbent column induce the cycling of fluid flows and pressure variations in the fixed bed. The DP-PSA system can perform a large number experiments with different cycle conditions, e.g. cycle time, mean pressure, temperature and stroke length. This allows the testing of adsorbent materials under a wide range of different experimental conditions. Therefore, this system is particularly suitable to measure kinetic and equilibrium properties of novel adsorbent materials for the use adsorption separation processes. The specific parameters which can be determined from DP-PSA experiments are given in Table 4.2, marked by △.

To achieve rapid and efficient adsorbent characterisation, accurate control and system automation are very important. The pistons in this system are driven and controlled by a real-time computer. This allows not only the semi-automatic running of many experiments with different cycle conditions but also increases the accuracy and reliability of the experiments. The control code, implemented in LabVIEW, achieves fast cycles and high frequency data logging by using advanced features, such as DMA FIFO and the FPGA of the Compact RIO. With this control setup the DP-PSA system can run smooth sinusoidal piston cycles with cycle times less than 1s.

In comparison to a conventional PSA system, the advantages of the DP-PSA apparatus can be summarized as follows.

- It is a closed system, therefore only small amounts of adsorbent and gas allow to run dozens of experiments.
- Only one adsorbing column is needed.
- The DP-PSA can run very fast cycles up to 1.5Hz with piston stroke lengths of 100mm. Thus, rapid testing of novel adsorbent materials can be undertaken.

- The results of the DP-PSA experiments allow to estimate the materials' characteristics by monitoring the system volume; absolute pressure; pressure drop across the adsorbing column; and temperatures in different positions of the bed in both gas and solid phase in real time.
- A wide range of operating conditions is allowed for a set mean pressure and temperature:
  - ✓ cycle speed
  - ✓ cycle duration
  - ✓ phase angle
  - ✓ piston stroke positions
- Most of the control is automated to increase the accuracy and reliability.

To validate the novel system this study includes the initial results with commercial pellets of 13X and various combinations of He, N_2 and CO_2 pure gases and gas mixtures. The experiments were compared with a detailed dynamic model and physical parameters for heat and mass transfer were obtained which showed the contribution macropore diffusion and heat transfer in the individual beads and in the packed bed. All the parameters are consistent with an equilibrium driven separation, which is what is physically valid for zeolite 13X and the binary mixture of CO_2 and N_2.

The main aim of the project has been achieved. This first thesis has highlighted a number of possible directions for future research:

1) Probably the most important improvement in the system would be the inclusion of a concentration measurement (or more accurately of the concentration difference between the pistons) as this would allow the direct measurement of the separation efficiency of novel materials, without the need of a detailed model.
2) The analysis of the results clearly enables the determination of the physical parameters of an adsorption column model. It would be useful to develop an automated analysis tool by linking the simulator to a least squares fitting algorithm. An important question which could then be answered would be what is the minimum set of independent measurements needed (if any at all) in order to have a set of parameters with sufficient accuracy.

3) The DP-PSA has been tested and validated on an equilibrium separation with traditional pelletised materials. It would be useful to investigate the response for a kinetically controlled system, possibly zeolite 4A for the same mixture, as well as study the response of monolithic adsorbents which become important especially in fast cycle applications.
4) While the system is currently designed for both vacuum and high pressure applications (up to 25 bar), with a second system being completed to achieve 60 bar, it would be very interesting to study a high pressure separation and possibly use a mixture of He, N_2 and CO_2 to mimic the high pressure separation and purification of hydrogen in H_2, CO and CO_2 mixtures.
5) The gas dosing system is designed to produce accurate mixtures containing water. It would be very interesting to study the performance of the DP-PSA in the presence of water for both hydrophilic and hydrophobic materials.
6) Full automation of the system would require also the control of the oven temperature, which is controlled manually at the moment.
7) As mentioned in the main chapters, fast movement of the pistons generates a large amount of heat, which requires a large set of additional experiments to predict accurately the temperature in the system. To improve the design of the DP-PSA system, frictional heat should be kept as possible and more effort could be spent on testing a range of materials for the piston seals.

Notation

A_c	Internal column surface area, m^2
A_p	Pellet surface area, m^2
$A_{\sin}$	The area of a sine, m^2
A_{tra}	The area of a trapezoid, m^2
α_{wl}	Surface area to volume ratio of the column wall
b_i^j	Adsorption equilibrium constant of site j for comp. i, bar^{-1}
$b_{i,0}^l$	Pre-exponential factor in $b_i^l = b_{i,0}^l \exp\left(\frac{-\Delta\widetilde{H}_i^l}{RT}\right)$
c	The concentration, mol m^{-3}
c_e	The mean concentration, mol m^{-3}
c_i	Concentration of comp. i in the gas phase, mol m^{-3}
c_i^m	Concentration of comp. i in the macropore, mol m^{-3}
$\hat{c}_{P,w}$	Specific heat capacity of the column wall, J kg^{-1} K^{-1}
c_T	Total concentration in the uid phase, mol m^{-3}
D	Diameter of the column
$D_{e,i}$	Effective diffusivity, m^2 s^{-1}
$D_{k,i}$	Knudsen diffusivity, m^2 s^{-1}
$D_{m,i}$	Molecular diffusivity, m^2 s^{-1}
D_p	Pore diffusivity, m^2 s^{-1}
D_o	Overall diffusivity, m^2 s^{-1}
D_v	The equivalent diffusivity for the viscous resistance, m^2 s^{-1}
$D_{Z,i}$	Axial diffusion coefficient, m^2 s^{-1}
d_p	The diameter of the equivalent-volume sphere, m

δ_{in}	An overall in-phase characteristic function
δ_{out}	An overall out of phase characteristic function
ε	Bed void fraction
ε_{cry}	Crystal void fraction
ε_p	Pellet void fraction
ε_t	Total void fraction
f	Darcy friction factor
f_1, f_2, f_3	Friction parameters
F	Molar flow rate, mol s^{-1}
φ , χ	The phase lags, degree
ϕ_B	The phase lag in the absence of adsorbents, degree
ϕ_Z	The phase lag in the presence of adsorbents, degree
γ	The relative amplitude of the concentration variation, mol m^{-3}
$\breve{H}_f$	Enthalpy in the fluid phase per unit volume,
$\widetilde{H}_i$	Partial molar enthalpy in the fluid phase of comp. i, J mol^{-1}
h_i	Heat transfer coefficient for comp. i, W m^{-2} K^{-1}
h_p	Heat transfer coefficient between pellet and bed, W m^{-2} K^{-1}
h_w	Heat transfer coefficient at the column wall, W m^{-2} K^{-1}
i	Imaginary number
J_i	Diffusive flux of component i, mol m^{-2} s^{-1}
J_T	Thermal diffusive flux, W m^{-2}
k	Thermal conductivity of bulk gas, J m^{-1} K^{-1}
$\widetilde{k}$	The leak rate of the system, s^{-1}
k_i^{cr}	LDF mass transfer coefficient of comp. i in the adsorbent crystal, m s^{-1}
k_i^p	LDF mass transfer coefficient of comp. i in the pellet, m s^{-1}
κ	The resistance constant of the flow rate at the piston outlet

K	Dimensionless Henry's law adsorption equilibrium constant
K_f	A constant related to the gradient of the adsorption isotherm at the equilibrium pressure
λ_z	Heat axial dispersion coefficient, J m^{-1} K^{-1}
L	Bed length, m
L_{pipe}	Pipe length, m
m	The dry mass of the adsorbent
MW_i	Molecule weight, kg mol^{-1}
μ	Viscosity, bar s
n_{total_i}	Total amount of comp. i
N_c	Number of components
Nu_c	Nusselt number for the column
Nu_i	Nusselt number for comp. i
Nu_p	Nusselt number for the pellet
Nu_{pipe}	Nusselt number for the pipe
Ω	Temperature-dependent collision integral
p	The relative amplitude of the pressure variation, bar
P	Pressure, bar
P_a	The pressure after feeding, bar
P_b	The pressure before feeding, bar
P_B	The pressures response to the volume perturbation in the absence of adsorbents, bar
P_z	The pressures response to the volume perturbation in the presence of adsorbents, bar
P_{cp}	Pressure of the adsorbing column, bar
P_e	The mean pressure, bar
P_i	Partial pressure of component i, bar
$P_{i,\infty}$	Partial pressure of component i in the atmosphere, bar

P_b	Pressure of the dosing system from valve V3 to V8 before feeding, bar
P_a	Pressure of the dosing system from valve V3 to V8 after feeding, bar
P_{col}	Pressure of the column, bar
Pr	Prandtl number
$\overline{Q_i}$	Concentration of comp. i averaged over the adsorbent pellet, mol m^{-3}
q_i	Sorbate concentration of comp. i, mol m^{-3}
$\overline{q}_i$	Sorbate concentration of comp. i averaged over the adsorbent crystal, mol m^{-3}
q_i^*	Sorbate concentration of comp. i at equilibrium, mol m^{-3}
$q_{i,s}^j$	Saturation capacity of site j for comp. i, mol m^{-3}
R	Gas constant
R_c	Radius of the column
R_i	Radius of the comp. i
Re	Reynolds number
Re_c	Reynolds number for the column
Re_p	Reynolds number for the pellet
Re_{pipe}	Reynolds number for the pipe
R_P	Pellet radius, m
R_{pipe}	Radius of the pipe
R_{pore}	Radius of the pore, m
r_p	Crystallite radius, m
ρ	The density of the adsorbent
ρ_f	Fluid density, kg m^{-3}
ρ_w	Column wall density, kg m^{-3}
σ	The average collision diameter, m
S	A constant that represents a rapid adsorption or desorption process

S_0	Start position of the piston, m
S_1	End position of the piston, m
Sc	Schmidt number
τ_p	Tortuosity of the particle
t	Time, s
T_g	Fluid temperature, K
T_p	Pellet temperature, K
T_w	Wall temperature, K
T_∞	Oven temperature, K
U	External heat transfer coefficient, J m^{-2} s^{-1} K^{-1}
U_f	Internal energy in the fluid phase, J
$\breve{U}_f$	Internal energy in the fluid phase per unit volume, J m^{-3}
U_g	Internal energy in the macropore, J
$\breve{U}_g$	Internal energy in the macropore per unit volume, J m^{-3}
U_p	Internal energy in the pellet, J
$\breve{U}_P$	Internal energy in the pellet per unit volume, J m^{-3}
U_S	Internal energy in the solid, J
$\breve{U}_S$	Internal energy in the solid per unit volume, J m^{-3}
v	Interstitial flow velocity, m s^{-1}
v_a	The relative amplitude of the volume variation, m^3
v_{max}	The maximum flow velocity in the column, m s^{-1}
V	The system volume, m^3
V_e	The mean volume, m^3
$V_{\delta-p}$	Dead volume plus the column volume, m^3
V_{ch}	The volume of the heads of the two piston cylinders, m^3
V_{column}	The column volume, m^3

V_{cp}	Dead volume of the packed column and pistons, m^3
V_{dead}	Dead volume of the packed column, m^3
V_{GAS}	The gas volume, m^3
V_{line1} , V_{line2}	The volume of the lines
V_p	Pellet volume, m^3
V_{sol}	The solid volume, m^3
V_{system}	The instant system volumn, m^3
V_w	Column/cylinder wall volume, m^3
ω	The angular velocity, degrees/s
x_i	Partial pressure of comp. i , m
z	Axial discretisation domain, m

References

Aaron, D., Tsouris, C.: Separation of CO 2 from Flue Gas: A Review. Sep. Sci. Technol. 40, 321–348 (2005).

ABB Oy: Firmware Manual ACSM1 Motion Control Program. Program. (2008).

Ackley, M.: Application of natural zeolites in the purification and separation of gases. Microporous Mesoporous Mater. 61, 25–42 (2003).

Ahn, H.: Effects of Feed Composition of Coke Oven Gas on a Layered Bed H 2 PSA Process. Adsorption. 339–356 (2002).

ASM Aerospace Specification Metals Inc.: AISI Type 316 Stainless Steel, annealed sheet. (2014).

Barrer, R.: Hydrothermal chemistry of zeolites. (1982).

Beck, J., Friedrich, D., Brandani, S., Guillas, S., Fraga, E.: Surrogate based Optimisation for Design of Pressure Swing Adsorption Systems. (2012).

Bell, R.G.: What are Zeolites. (2001).

Bonenfant, D., Kharoune, M., Niquette, P., Mimeault, M., Hausler, R.: Advances in principal factors influencing carbon dioxide adsorption on zeolites. Sci. Technol. Adv. Mater. 9, 013007 (2008).

Boniface, H., Ruthven, D.M.: Chromatographic adsorption with sinusoidal input. Chem. Eng. Sci. 40, 2053–2061 (1985).

Bragg, W.L.: The Atomic Structure of Minerals, (1937).

Breck, D.W.: Zeolite molecular sieves. John Wiley & sons，New York. (1974).

Cen, P., Chen, W.: Ternary Gas Mixture Separation by Pressure Swing Adsorption: A Combined Hydrogen-Methane Separation and Acid Gas Removal Process. Glass. 1201–1208 (1985).

Chai, S.W., Kothare, M. V., Sircar, S.: Rapid Pressure Swing Adsorption for Reduction of Bed Size Factor of a Medical Oxygen Concentrator. Ind. Eng. Chem. Res. 50, 8703–8710 (2011).

Chazournes, L. de: Kyoto Protocol to the United Nations Framework Convention on Climate Change. UN's Audiov. Libr. Int. Law. (1998).

Chen, L., Mowat, J.P.S., Fairen-jimenez, D., Morrison, C.A., Thompson, S.P., Wright, P.A., Du, T.: Elucidating the Breathing of the Metal − Organic Framework MIL- 53 (Sc) with ab Initio Molecular Dynamics Simulations and in Situ X-ray Powder Diff raction. J. Am. Chem. Soc. 53, (2013).

Choi, S., Drese, J.H., Jones, C.W.: Adsorbent materials for carbon dioxide capture from large anthropogenic point sources. ChemSusChem. 2, 796–854 (2009).

Alessandro, D.M., Smit, B., Long, J.R.: Carbon dioxide capture: prospects for new materials. Angew. Chem. Int. Ed. Engl. 49, 6058–82 (2010).

Dahowski, R.T., Li, X., Davidson, C.L., Wei, N., Dooley, J.J., Gentile, R.H.: A preliminary cost curve assessment of carbon dioxide capture and storage potential in China. Energy Procedia. 1, 2849–2856 (2009).

Daniel, D., De, M.P.G.: Process for Separating a Binary Gaseous Mixture by Adsorption. US Pat. 3,155,468. (1958).

Dechene, F.J.: Oxygen generator with two compressor stages. US4552571 A. (1985).

Diagne, D., Goto, M., Hirose, T.: New PSA Process with Intermediate Feed Inlet Position Operated with Dual Refluxes: Application to Carbon Dioxide Removal and Enrichment. J. Chem. Eng. Japan. 27, 85–89 (1994).

Diesendorf, M.: Greenhouse solutions with sustainable energy. (2007).

Do, D., Do, H., Prasetyo, I.: Constant molar flow semi-batch adsorber as a tool to study adsorption kinetics of pure gases and vapours. 55, 1717–1727 (2000).

Do, D.D.: Adsorption Analysis: Equilibria and Kinetics. Imperial College Press (1998).

Dong, J.H.: Portable PSA Oxygen Generator. US 5893944 A. 1–6 (1999).

Doong, S.J., Yang, R.T.: Bidisperse pore diffusion model for zeolite pressure swing adsorption. AIChE J. 33, 1045–1049 (1987).

Eriksson, R.: Fractionating apparatus. US Pat. 4169715. (1979).

Farooq, S., Thaeron, C., Ruthven, D.M.: Numerical simulation of a parallel-passage piston-driven PSA unit. Sep. Purif. Technol. 13, 181–193 (1998).

Friedrich, D., Ferrari, M., Brandani, S.: Efficient Simulation and Acceleration of Convergence for a Dual Piston Pressure Swing Adsorption System. Ind. Eng. Chem. Res. 52, 8897 – 8905 (2013).

GE Druck: DPI 280 Series Digital Process Indicator Serial Interface, Serial Interface Manual K152. Digit. Process. (1997).

G.E. Keller II and C.H.A. Kuo, Enhanced Gas Separation by Selective Adsorption. US Patent 4,354,859 (1982)

Glover, T.G., Wang, Y., Le Van, D.M.: Diffusion of condensable vapors in single adsorbent particles measured via concentration-swing frequency response. Langmuir. 24, 13406–13 (2008).

Grande, C. a., Blom, R.: Dual Pressure Swing Adsorption Units for Gas Separation and Purification. Ind. Eng. Chem. Res. 51, 8695–8699 (2012).

Grande, C.A., Rodrigues, A.E.: Biogas to Fuel by Vacuum Pressure Swing Adsorption I . Behavior of Equilibrium and Kinetic-Based Adsorbents. Society. 4595–4605 (2007).

Grenier, P.H., A.Malka-Edery, V.Bourdin: A Temperature Frequency Response Method for Adsorption Kinetics Measurement. Adsorption. 135–143 (1999).

Gusenius, E.M.: Beginnings of greatness in Swedish Chemistry. II. Axel Fredrick Cronstedt (1722-1765). Trans. Kans. Acad. Sci. 72, 476–85 (1969).

Harlick, P.J.E., Tezel, F.H.: An experimental adsorbent screening study for CO2 removal from N2. Microporous Mesoporous Mater. 76, 71–79 (2004).

Harvell, C.D., Mitchell, C.E., Ward, J.R., Altizer, S., Dobson, A.P., Ostfeld, R.S., Samuel, M.D.: Climate warming and disease risks for terrestrial and marine biota. Science. 296, 2158–62 (2002).

Hayashi, S.: Dynamics of high purity oxygen PSA. Gas Sep. Purif. I, 19–23 (1996).

Hernandez-Huesca R.; Daz L.; Aguilar-Armenta G.: Adsorption equilibria and kinetics of CO2, CH4 and N2 in natural zeolites. Sep. Purif. Technol. 15, 163–173 (1999).

Hu, X., Mangano, E., Friedrich, D., Ahn, H., Brandani, S.: Diffusion mechanism of CO2 in 13X zeolite beads. Adsorption. (2013).

Incropera, F., Lavine, A., DeWitt, D.: Fundamentals of heat and mass transfer. (2011).

Jacobson, M.Z.: Strong radiative heating due to the mixing state of black carbon in atmospheric aerosols. Nature. 409, 695–7 (2001).

Jiang, K., Hu, X., Zhuang, X., Liu, Q., Zhu, S.: China's Energy Demand and CO2 Emissions Scenarios in 2050. Adv. Clim. Chang. Res. (2008).

Jordi, R., Do, D.: Analysis of the frequency response method for sorption kinetics in bidispersed structured sorbents. Chem. Eng. Sci. (1993).

Jordi, R., Do, D.: Analysis of the frequency response method applied to non-isothermal sorption studies. Chem. Eng. Sci. (1994).

Kanniche, M., Gros-Bonnivard, R., Jaud, P., Valle-Marcos, J., Amann, J.-M., Bouallou, C.: Pre-combustion, post-combustion and oxy-combustion in thermal power plant for CO2 capture. Appl. Therm. Eng. 30, 53–62 (2010).

Keskes, E., Adjiman, C.S., Galindo, A.: A Physical Absorption PRocess for the Capture of CO2 from CO2 Rich Natural Gas Streams. Adsorpt. J. Int. Adsorpt. Soc. (2009).

Khatri, R.A., Chuang, S.S.C., Soong, Y., Gray, M.: Carbon Dioxide Capture by Diamine-Grafted SBA-15 : A Combined Fourier Transform Infrared and Mass Spectrometry Study. Ind. Eng. Chem. Res. 3702–3708 (2005).

Kikkinides, E., Yang, R., Cho, S.: Concentration and recovery of carbon dioxide from flue gas by pressure swing adsorption. Ind. Eng. Chem. Res. (1993).

Kikkinides, E.S., Georgiadis, M.C.: Optimization of Multibed Pressure Swing Adsorption Processes. Ind. Eng. Chem. Res. 48, 5388–5398 (2009).

De Klerk, A.: Voidage variation in packed beds at small column to particle diameter ratio. AIChE J. 49, 2022–2029 (2003).

Kowler, D.E., Kadlec, R.H.: The Optimal Control of a Periodic Adsorber:Part I. Experiment. AIChE J. 18, 1207–1212 (1972).

L.M.Sun, F.Meunier, J.Karger: On the Heat Effect in Measurements of Sorption Kinetics by the Frequency Response Method. Chem. Eng. Sci. 715–722 (1993).

Lackner, K., Butt, D., Wendt, C.: Progress on binding CO 2 in mineral substrates. Energy Convers. Manag. 38, 259–264 (1997).

Li, C., Finlayson, B.A.: Heat transfer in packed beds - A reevaluation. Chem. Eng. 32, 1055–1066 (1977).

Linga, P., Kumar, R., Englezos, P.: The clathrate hydrate process for post and pre-combustion capture of carbon dioxide. J. Hazard. Mater. 149, 625–9 (2007).

Malek, A., Farooq, S.: Study of a Six-Bed Pressure Swing Adsorption Process. AIChE J. 43, (1997).

Mangano, E.: Personal Communication. (2013).

Mangano, E., Brandani, S., Ferrari, M.C., Ahn, H., Friedrich, D., Lozinska, M.L., Wright, P. a., Kahr, J., Morris, R., Croad, M., McKeown, N., Shamsipour, H., Budd, P.: Efficient and Rapid Screening of Novel Adsorbents for Carbon Capture in the UK IGSCC Project. Energy Procedia. 37, 40–47 (2013).

Martinot, E.: Renewables 2011 global status report. (2011).

Meier, W., Olson, D.: Atlas of zeolite structure types. (1987).

Metz, B., O.Davidson, H. C. de Coninck, M. Loos, and L.A.M.: IPCC special report on Carbon dioxide capture and storage. Cambridge University Press, Cambridge, United Kingdom and New York, NY, USA (2005).

Newman, S.: Acid and sour gas treating processes. (1985).

Ng, E.-P., Mintova, S.: Nanoporous materials with enhanced hydrophilicity and high water sorption capacity. Microporous Mesoporous Mater. 114, 1–26 (2008).

NI: User guide and specifications NI USB-9213. (2009)(a).

NI: Compact RIO Developers Guide. (2009)(b).

NI: Using the NI Scan Engine, http:// http:/zone.ni.com/reference/en-XX/help/371361H-01/lvioscanhelp/scan_engine/, (08/12/2011).

NI: http://uk.ni.com/. (10/01/2013).

NIST: Temperature-Electromotive Force Reference Functions and Tables for the Letter-Designated Thermocouple Types Based on the ITS-90. (1993).

NRC: Advancing the science of climate change. The National Academies Press, Washington, DC (2010).

Park, I.S., Petkovska, M., Do, D.: Frequency response of an adsorber with modulation of the inlet molar flow-rate—II. A continuous flow adsorber. Chem. Eng. Sci. 53, 833–843 (1998)(b).

Park, I.S., Petkovska, M., Do, D.: Frequency response of an adsorber with modulation of the inlet molar flow-rate--l . 53, (1998)(a).

Parmesan, C., Yohe, G.: A globally coherent fingerprint of climate change impacts across natural systems. Nature. 421, 37–42 (2003).

Pawlesa, J., Zukal, A., Čejka, J.: Synthesis and adsorption investigations of zeolites MCM-22 and MCM-49 modified by alkali metal cations. Adsorption. 13, 257–265 (2007).

Petkovska, M., Do, D.: Nonlinear frequency response of adsorption systems: isothermal batch and continuous flow adsorbers. Chem. Eng. Sci. (1998).

Petkovska, M., Do, D.: Use of Higher-Order Frequency Response Functions for Identification of Nonlinear Adsorption Kinetics: Single Mechanisms under Isothermal Conditions. Nonlinear Dyn. (2000).

Rajendran, A., Farooq, S., Ruthven, D.M.: Analysis of a piston PSA process for air separation. Chem. Eng. Sci. 57, 419–433 (2002).

Rao, M.B., Sircar, S.: Thermodynamic Consistency for Binary Gas Adsorption Equilibria. Langmuir. 15, 7258–7267 (1999).

Reynolds, S.P., Ebner, A.D., Ritter, J.A.: Enriching PSA Cycle for the Production of Nitrogen from Air. Ind. Eng. Chem. Res. 45, 3256–3264 (2006).

Rezaei, F.: Optimization of Structured Adsorbents for Gas Separation Processes. (2011).

Rouquerol, F., Rouquerol, J., Sing, K.S.W.: Adsorption by Powders and Porous Solids; Principles, Methodology and Applications. Academic Press, San Diego (1999).

Rouse, A.J.: Fast Cycle Low Pressure Drop Systems for the Separation of CO2, Chapter 2. (2004).

Ruthven, D.M.: Principles of adsorption and adsorption processes. (1984).

Ruthven, D.M.: CO2Capture by Adsorption: General Principles. (2011).

Ruthven, D.M., S.Farooq, K.S.Knaebel: Pressure Swing Adsorption. VCH, New York (1994).

Shen, D., Rees, L.V..: Frequency response study of single-file diffusion in theta-1. J. Chem. Soc. Faraday Trans. (1994).

Shen, D., Rees, L.V.C.: Diffusivities of benzene in HZSM-5, silicalite-1 and NaX determined by frequency response techniques. Zeolites. 11, 666–671 (1991).

Shen, D., Rees, L.V.C.: Frequency response technique measurements of p-xylene diffusion in silicalite-1 and -2. J. Chem. Soc. Faraday Trans. 89, 1063 (1993).

Silva, F.A. Da, Rodrigues, A.E.: PropylenePropane Separation by Vacuum Swing Adsorption Using 13X Zeolite. AIChE J. 47, 341–357 (2001).

Singh, K., Jones, J.: Numerical simulation of air separation by piston-driven pressure swing adsorption. Chem. Eng. Sci. 52, 3133–3145 (1997).

Sircar, S., Hanley, B.: Production of oxygen enriched air by rapid pressure swing adsorption. Adsorption. 320, 313–320 (1995).

Skarstrom, C.: Method and Apparatus for Fractionating. US Pat. 2,944,627. (1960).

Smith, J. V: Biochemical evolution. I. Polymerization On internal, organophilic silica surfaces of dealuminated zeolites and feldspars. Proc. Natl. Acad. Sci. U. S. A. 95, 3370–5 (1998).

Starr, F.: Integrated Gasification Combined Cycle for Carbon Capture & Storage. (2009).

Stephanopoulos, G.: Chemical process control: an introduction to theory and practice, Chapter 3. New Jersey, USA (1984).

Suzuki, M., Suzuki, T., Sakoda, A., Izumi, J.U.N.: Piston-Driven Ultra Rapid Pressure Swing Adsorption. Adsorption. 119, 111–119 (1996).

Suzuki, T., Sakoda, A., Suzuki, M., Izumi, J.: Recovery of carbon dioxide from stack gas by piston-driven ultra-rapid PSA. J. Chem. Eng. Japan. 30, 1026–1033 (1997).

Sward, K.B., LeVan, M.D.: Frequency Response Method for Measuring Mass Transfer Rates in Adsorbents via Pressure Perturbation. Adsorption. (2003).

Sweet, W.: Winner: Restoring Coal's Sheen, (2008).

Szostak, R.: Molecular sieves: principles of synthesis and identification. (1997).

Taficzyk, M.: Multicomponent pressure swing adsorption Part I . Modelling of large-scale BSA installations. Chem. Eng. Process. 36, (1997).

Takamura, Y., Narita, S., Aoki, J., Hironaka, S., Uchida, S.: Evaluation of dual-bed pressure swing adsorption for CO 2 recovery from boiler exhaust gas. Sep. Purif. Technol. 24, 519–528 (2001).

The U.S. Department of Energy's National Energy Technology Laboratory: Carbon Sequestration Atlas of the United States and Canada, Second Edition. (2008).

Todd, R., Webley, P.: Mass transfer models for rapid pressure swing adsorption simulation. AIChE J. 52, (2006).

Tsuru, T., Hino, T., Yoshioka, T., Asaeda, M.: Permporometry characterization of microporous ceramic membranes. J. Memb. Sci. 186, 257–265 (2001).

U.S. department of Energy: Gasification Body. U.S. department of Energy (2010).

UOP: 13X-APG MOLSIV TM Adsorbent. 60017 (2003).

V.Bourdin, P.G.Gray, P.H.Grenier, M.F.Terrier: An apparatus for adsorption for dynamics studies using infrared measurement of the adsorbent temperature. Rev.Sci.Instrum. 2130–2136 (1998).

Vergunst, T., Linders, M.J.G., Kapteijn, F., Moulijn, J. a.: Carbon-Based Monolithic Structures. Catal. Rev. 43, 291–314 (2001).

Virta, R.L.: Zeolites, U.S. Geological Survey Puplication, (1998).

Wakao, N., Kaguei, S., Funazkri, T.: Effect of fluid dispersion coefficients on particle-to-fluid heat transfer coefficients in packed beds: correlation of Nusselt numbers. Chem. Eng. Sci. 34, 325–336 (1979).

Wall, T.F.: Combustion processes for carbon capture. Proc. Combust. Inst. 31, 31–47 (2007).

Wang, Y., LeVan, M.D.: Investigation of Mixture Diffusion in Nanoporous Adsorbents via the Pressure-Swing Frequency Response Method. 2. Oxygen and Nitrogen in a Carbon Molecular Sieve. Ind. Eng. Chem. Res. 44, 4745–4752 (2005)(a).

Wang, Y., LeVan, M.D.: Investigation of Mixture Diffusion in Nanoporous Adsorbents via the Pressure-Swing Frequency Response Method. 1. Theoretical Treatment. Ind. Eng. Chem. Res. 44, 3692–3701 (2005)(b).

Wang, Y., LeVan, M.D.: Mixture Diffusion in Nanoporous Adsorbents: Development of Fickian Flux Relationship and Concentration-Swing Frequency Response Method. Ind. Eng. Chem. Res. 46, 2141–2154 (2007).

Wang, Y., LeVan, M.D.: Nanopore Diffusion Rates for Adsorption Determined by Pressure-Swing and Concentration-Swing Frequency Response and Comparison with Darken's Equation. Ind. Eng. Chem. Res. 47, 3121–3128 (2008).

Wikipedia. Greenhouse effect. Retrieved from http://en.wikipedia.org/wiki/Greenhouse_effect. (10/08/2014)

Wilhelm, R., Rice, A., Rolke, R., Sweed, N.: Parametric Pumping. Dynamic Principle for Separating Fluid Mixtures. Ind.Eng.Chem.Fundaman. 7, 337–349 (1968).

Xiao, P., Wilson, S., Xiao, G., Singh, R., Webley, P.: Novel adsorption processes for carbon dioxide capture within a IGCC process. Energy Procedia. 1, 631–638 (2009).

Xiao, P., Zhang, J., Webley, P., Li, G., Singh, R., Todd, R.: Capture of CO2 from flue gas streams with zeolite 13X by vacuum-pressure swing adsorption. Adsorption. 14, 575–582 (2008).

Yasuda, Y.: Frequency response method for study of the kinetic behavior of a gas-surface system. 1. Theoretical treatment. J. Phys. Chem. 80, 1867–1869 (1976).

Yasuda, Y.: Determination of vapor diffusion coefficients in zeolite by the frequency response method. J. Phys. Chem. v, 1913–1917 (1982).

Yasuda, Y.: Frequency-response method for investigation of gas-surface dynamic phenomena. Heterog. Chem. Rev. (1994).

Yasuda, Y., Saeki, M.: Kinetic details of a gas-surface system by the frequency response method. J. Phys. Chem. (1978).

Yeh, J.T., Pennline, H.W., Resnik, K.P., Rygle, K.: Absorption and Regeneration Studies for CO2 capture by aqueous ammonia. Changes. 1–12 (2004).

Yu, C.-H.: A Review of CO2 Capture by Absorption and Adsorption. Aerosol Air Qual. Res. 745–769 (2012).

Zachos, J.: Trends , Rhythms , and Aberrations in Global Climate 65 Ma to Present. Science (80-.). 686, (2013).

Zhao, D., Cleare, K., Oliver, C., Ingram, C., Cook, D., Szostak, R., Kevan, L.: Characteristics of the synthetic heulandite-clinoptilolite family of zeolites. Microporous Mesoporous Mater. 21, 371–379 (1998).

Zhou, L., Lu, C., Bian, S., Zhou, Y.: Pure Hydrogen from the Dry Gas of Refineries via a Novel Pressure Swing Adsorption Process. Ind. Eng. Chem. Res. 5290–5297 (2002).

IPCC AR4 SYR appendix glossary. (2008)(a).

Climate Change Act 2008. The Stationery Office Limited (2008)(b).

Opportunities for CO2 Storage around Scotland. (2009).

Inventory of U.S. Greenhouse Gas Emissions and Sinks: 1990-2011. (2013).

Atlas Database, Retrieved from http://www.ch.ic.ac.uk/vchemlib/course/zeolite/structure.html. (12/05/2014).

Appendix I The conversion between the binary value read by thermocouple and the actual value

The temperature signal read by NI9213 is in binary format. The equations of converting this binary value to an actual temperature using the cold junction to minimise signal noise are given below.

The binary thermocouple and CJC values are converted to voltage by equation (1),

$$Voltage = Binary \times 78.123mV \div 8388607 \quad \text{Eq. I.1}$$

To convert CJC data from voltage to temperature, the resistance of the thermistor needs to be calculated by equation (2).

$$R_T = (10000 \times CJC \times 32) \div (2.5 - CJC \times 32) \quad \text{Eq. I.2}$$

The CJC temperature is expressed as

$$T = [1 \div [A + B(\ln(R_T)) + C(\ln(R_T))^3]] - (273.15 + OffsetConstant) \quad \text{Eq. I.3}$$

Where, T = temperature in °C

$A = 1.2873851 \times 10^{-3}$

$B = 2.3575235 \times 10^{-4}$

$C = 9.4978060 \times 10^{-8}$

R_T = thermistor resistance reading

The Offset Constant is the typical temperature gradient between the CJC sensor and the thermocouple cold junction. The equations here refer to the National Institute of Standards and Technology (NIST) Monograph 175 thermocouple reference tables (NIST 1993).

There are three steps to obtain the actual temperature.

Step 1: The CJC temperature is converted to a voltage using a reverse polynomial equation for the particular thermocouple wire.

Step 2: The CJC voltage is added to thermocouple voltage.

Step3: The total voltage is converted to the final temperature reading using thermocouple linearising equations.

Because the thermocouple output voltages are highly nonlinear, it is necessary to approximate the thermocouple voltage-versus-temperature curve using polynomials. The polynomials are in the following form where v is the thermocouple voltage in volts, T is the temperature in degrees Celsius

$$T = v\times(2.508355\times10^{-2} + v\times(7.860106\times10^{-8} + v\times(-2.503131\times10^{-10} + v\times(8.315270\times10^{-14} + v\times(-1.228034\times10^{-17} + v\times(9.804036\times10^{-22} + v\times(-4.413030\times10^{-26} + v\times(1.057734\times10^{-30}))))))) \quad \text{Eq. I.4}$$

Appendix II The ABB drive parameters which have been changed

Index	Parameters	Values
13.01	AI1 filt time	0.01s
13.02	AI1 Max	10V
13.03	AI1 Min	0V
13.04	Max Scale	0.1m
13.05	Min Scale	0m
20.01	Maximum Speed	8000rpm
20.02	Minimum Speed	−8000rpm
20.05	Maximum Current	12.16A
20.06	Maximum Torque	125%
20.07	Minimum Torque	−125%
22.05	Zero Speed Limit	30rpm
57.06	Ref 1 SRC	4.17 Pos Ref Limited
60.13	Maximum Position	0.102m
60.14	Minimum Position	−0.002m
62.07	Homing Speed Ref1	0.005u/s
62.09	Home Position	0
62.11	Present Mode	Disabled
62.13	Present Position	0.01
67.01	Sync Ref Sel	D2D Ref 1
67.03	Interpolate Mode	Interpolate
68.02	Sync Gear Mul	1
68.03	Sync Gear Div	1
68.07	Synchron Mode	Relative

Appendix III The experiment list

Index	Gas	Adsorbent	Piston1 SP(mm)	Piston2 SP(mm)	Piston1 EP(mm)	Piston2 EP(mm)	T_0 (°C)	Cycle Time (s)	Phase angle	Amount of gas(mole)	Maximum gas velocity (m/s)	Kinematic viscosity (m^2/s)	Re
1	He	13X (2pellets)	0	100	100	0	100	4	π	0.008654219	7.854	1.77E-04	6.93E+02
2	He	13X (2pellets)	100	0	100	0	100	4	X	0.008956128	7.854	1.77E-04	6.93E+02
3	He	13X (2pellets)	100	0	0	0	100	10	X	0.011684582	3.1416	1.77E-04	2.77E+02
4	He	13X (2pellets)	100	0	0	0	100	20	X	0.012546921	1.5708	1.77E-04	1.39E+02
5	He	13X (2pellets)	100	0	0	0	100	4	X	0.011684532	7.854	1.77E-04	6.93E+02
6	He	13X (2pellets)	100	0	0	0	100	40	X	0.011250881	0.7854	1.77E-04	6.93E+01
7	He	13X (2pellets)	100	0	0	0	60	4	X	0.009258423	7.854	1.46E-04	8.40E+02
8	He	13X (2pellets)	100	0	0	0	60	10	X	0.011254682	3.1416	1.46E-04	3.36E+02
9	He	13X (2pellets)	100	0	0	0	60	20	X	0.011536849	1.5708	1.46E-04	1.68E+02
10	He	13X (2pellets)	0	0	0	0	60	0	X	0.007584213	0	1.46E-04	
11	He	13X (2pellets)	100	0	50	0	60	2	X	0.010236984	7.854	1.46E-04	8.40E+02
12	He	13X (2pellets)	50	0	0	0	60	2	X	0.011325427	7.854	1.46E-04	8.40E+02
13	N2	13X (2pellets)	100	0	50	0	60	2	X	0.012548113	7.854	1.89E-05	6.49E+03
14	He	13X (2pellets)	100	0	75	0	60	1	X	0.010612542	7.854	1.46E-04	8.40E+02
15	He	13X (2pellets)	100	0	0	0	30	4	X	0.011865752	7.854	1.24E-04	9.86E+02
16	He	13X (2pellets)	100	0	75	0	30	1	X	0.012654852	7.854	1.24E-04	9.86E+02
17	He	13X (2pellets)	0	100	100	0	30	10	π	0.012456511	3.1416	1.24E-04	3.95E+02
18	He	13X (2pellets)	0	100	100	0	30	4	π	0.012784231	7.854	1.24E-04	9.86E+02
19	He	13X (2pellets)	75	100	100	75	30	1	π	0.011685423	7.854	1.24E-04	9.86E+02
20	He	13X (2pellets)	50	0	0	50	30	2	π	0.013542685	7.854	1.24E-04	9.86E+02
21	He	13X (2pellets)	0	25	25	0	30	1	π	0.011895432	7.854	1.24E-04	9.86E+02

22	He	13X (2pellets)	0	25	25	0	60	1	π	0.012644851	7.854	1.46E-04	8.40E+02
23	He	13X (2pellets)	75	100	100	75	60	1	π	0.012245879	7.854	1.46E-04	8.40E+02
24	He	13X (2pellets)	0	100	100	0	60	4	π	0.010895642	7.854	1.46E-04	8.40E+02
25	He	13X (2pellets)	0	100	100	0	60	10	π	0.012154865	3.1416	1.46E-04	3.36E+02
26	He	13X (2pellets)	0	25	25	0	100	1	π	0.012014515	7.854	1.77E-04	6.93E+02
27	He	13X (2pellets)	75	100	100	75	100	1	π	0.011023549	7.854	1.77E-04	6.93E+02
28	He	13X (2pellets)	0	100	100	0	100	10	π	0.012543521	3.1416	1.77E-04	2.77E+02
29	He	13X (2pellets)	0	100	100	0	100	10	π	0.011869755	3.1416	1.77E-04	2.77E+02
30	He	13X (2pellets)	0	100	100	0	100	20	π	0.01156852	1.5708	1.77E-04	1.39E+02
31	He	13X (2pellets)	0	100	100	0	100	4	π	0.011456852	7.854	1.77E-04	6.93E+02
32	He	13X (2pellets)	0	0	50	50	30	stopped	0	0.009856485	0	1.24E-04	
33	N2	13X (2pellets)	0	100	100	0	30	4	π	0.011532458	7.854	1.60E-05	7.66E+03
34	N2	13X (2pellets)	0	100	100	0	30	10	π	0.012564682	3.1416	1.60E-05	3.06E+03
35	N2	13X (2pellets)	0	100	100	0	30	20	π	0.012856423	1.5708	1.60E-05	1.53E+03
36	N2	13X (2pellets)	0	100	100	0	30	10	π	0.011652341	3.1416	1.60E-05	3.06E+03
37	N2	13X (2pellets)	0	100	100	0	100	10	π	0.011753255	3.1416	2.30E-05	2.13E+03
38	N2	13X (2pellets)	0	100	100	0	100	4	π	0.012023549	7.854	2.30E-05	5.32E+03
39	N2	13X (2pellets)	0	100	100	0	100	20	π	0.011562343	1.5708	2.30E-05	1.06E+03
40	CO2	13X (2pellets)	0	100	100	0	100	10	π	0.012594562	3.1416	1.28E-05	3.83E+03
41	He	13X (2pellets)	0	100	100	0	100	10	π	0.011856412	3.1416	1.77E-04	2.77E+02
42	N2	13X (2pellets)	0	100	100	0	100	10	π	0.006542512	3.1416	2.30E-05	2.13E+03
43	He	13X	0	100	100	0	100	4	π	0.012651235	7.854	1.77E-04	6.93E+02
44	He	13X	0	100	100	0	100	10	π	0.010544522	3.1416	1.77E-04	2.77E+02
45	He	13X	0	100	100	0	100	4	π	0.012053445	7.854	1.77E-04	6.93E+02
46	He	13X	0	100	100	0	100	10	π	0.011230524	3.1416	1.77E-04	2.77E+02
47	He	13X	0	100	100	0	100	10	π	0.012544435	3.1416	1.77E-04	2.77E+02
48	He	13X	0	100	100	0	100	10	π	0.015413231	3.1416	1.77E-04	2.77E+02
49	CO2	13X	0	100	100	0	100	10	π	0.015325451	3.1416	1.28E-05	3.83E+03

50	CO2	13X	0	100	100	0	100	4	π	0.016012132	7.854	1.28E-05	9.56E+03
51	CO2	13X	0	100	100	0	30	10	π	0.015632132	3.1416	8.61E-06	5.69E+03
52	CO2	13X	0	100	100	0	30	4	π	0.016225423	7.854	8.61E-06	1.42E+04
53	CO2	13X	100	100	0	0	30	20	0	0.014322541	1.5708	8.61E-06	2.85E+03
54	CO2	13X	100	100	0	0	30	10	0	0.013222541	3.1416	8.61E-06	5.69E+03
55	CO2	13X	100	100	0	0	30	4	0	0.012325122	7.854	8.61E-06	1.42E+04
56	CO2	13X	100	100	0	0	100	20	0	0.013201254	1.5708	1.28E-05	1.91E+03
57	CO2	13X	100	100	0	0	100	10	0	0.012121356	3.1416	1.28E-05	3.83E+03
58	CO2	13X	100	100	0	0	100	4	0	0.014514265	7.854	1.28E-05	9.56E+03
59	CO2	13X	100	100	75	75	100	5	0	0.013066205	1.5708	1.28E-05	1.91E+03
60	CO2	13X	100	100	75	75	100	1	0	0.013066205	7.854	1.28E-05	9.56E+03
61	CO2	13X	100	100	75	75	30	5	0	0.013066205	1.5708	8.61E-06	2.85E+03
62	CO2	13X	100	100	75	75	30	1	0	0.013066205	7.854	8.61E-06	1.42E+04
63	CO2	13X	100	100	0	0	30	20	0.5π	0.013245815	1.5708	1.28E-05	1.91E+03
64	CO2	13X	100	100	0	0	30	10	0.5π	0.004602541	3.1416	8.61E-06	5.69E+03
65	CO2	13X	100	100	0	0	30	10	0.5π	0.013245123	3.1416	8.61E-06	5.69E+03
66	CO2	13X	100	100	0	0	30	4	1.5π	0.015539421	7.854	8.61E-06	1.42E+04
67	CO2	13X	100	100	0	0	100	10	0.5π	0.013064162	3.1416	1.28E-05	3.83E+03
68	CO2	13X	100	100	0	0	100	4	0.5π	0.013064162	7.854	1.28E-05	9.56E+03
69	CO2	13X	100	100	0	0	30	4	0.5π	0.013064162	7.854	8.61E-06	1.42E+04
70	N2	13X	100	100	0	0	100	10	1.5π	0.013125451	3.1416	2.30E-05	2.13E+03
71	N2	13X	100	100	0	0	100	4	0.5π	0.010134356	7.854	2.30E-05	5.32E+03
72	CO2	13X	100	100	75	75	100	2.5	0.5π	0.017276049	3.1416	1.28E-05	3.83E+03
73	CO2N2	13X	0	100	0	100	100	10	1.5π	0.011857196	3.1416	1.79E-05	2.74E+03
74	CO2N2	13X	0	100	0	100	30	4	1.5π	0.008530396	7.854	1.79E-05	6.84E+03
75	He	13X	0	100	0	100	30	10	0.5π	0.012568113	3.1416	1.24E-04	3.95E+02
76	He	13X	0	100	0	100	30	4	0.5π	0.010134356	7.854	1.24E-04	9.86E+02
77	He	13X	0	100	0	100	30	2	0.5π	0.014581765	15.708	1.24E-04	1.97E+03
78	N2	13X	0	100	0	100	30	10	0.5π	0.013665185	3.1416	1.60E-05	3.06E+03
79	N2	13X	0	100	0	100	30	4	0.5π	0.011589472	7.854	1.60E-05	7.66E+03
80	He	13X	0	100	0	100	30	10	0.5π	0.002926842	3.1416	1.24E-04	3.95E+02
81	He	13X	0	100	0	100	30	10	0.5π	0.009829961	3.1416	1.24E-04	3.95E+02
82	He	13X	0	100	0	100	30	4	0.5π	0.011215612	7.854	1.24E-04	9.86E+02
83	He	13X	0	0	100	25	30	4	π	0.005878251	7.854	1.24E-04	9.86E+02
84	CO2N2	13X	0	0	100	25	30	4	1.5π	0.013632736	7.854	1.23E-05	9.96E+03
85	CO2N2	13X	0	0	100	25	30	10	1.5π	0.01664264	3.1416	1.23E-05	3.98E+03
86	CO2N2	13X	0	0	100	50	30	4	1.5π	0.009483801	7.854	1.23E-05	9.96E+03
87	CO2N2	13X	0	0	100	50	30	10	1.5π	0.011541004	3.1416	1.23E-05	3.98E+03
88	CO2N2	13X	0	50	100	100	30	4	1.5π	0.008988865	7.854	1.23E-05	9.96E+03
89	CO2N2	13X	0	0	100	25	100	4	1.5π	0.011214512	7.854	1.79E-05	6.84E+03
90	CO2N2	13X	0	0	100	50	100	10	1.5π	0.011214512	3.1416	1.79E-05	2.74E+03
91	CO2N2	13X	0	0	100	25	100	10	1.5π	0.009759384	3.1416	1.79E-05	2.74E+03
92	CO2N2	13X	0	0	100	25	100	4	0.5π	0.007543408	7.854	1.79E-05	6.84E+03

93	CO2N2	13X	0	0	100	25	30	10	0.5π	0.01759119	3.1416	1.23E-05	3.98E+03
94	CO2N2	13X	0	0	100	50	30	4	0.5π	0.010872137	7.854	1.23E-05	9.96E+03
95	CO2N2	13X	0	0	100	50	30	10	0.5π	0.009019577	3.1416	1.23E-05	3.98E+03
96	CO2N2	13X	0	0	100	25	100	10	0.5π	0.012081481	3.1416	1.79E-05	2.74E+03
97	CO2N2	13X	0	0	100	50	100	4	0.5π	0.009483801	7.854	1.79E-05	6.84E+03
98	CO2N2	13X	0	0	100	50	100	10	0.5π	0.007977259	3.1416	1.79E-05	2.74E+03
99	CO2N2	13X	0	75	100	100	100	4	0.5π	0.011214512	7.854	1.79E-05	6.84E+03
100	CO2N2	13X	0	75	100	100	100	10	0.5π	0.008202945	3.1416	1.79E-05	2.74E+03
101	He	13X	0	0	100	25	100	10	0.5π	0.007254213	3.1416	1.77E-04	2.77E+02
102	CO2N2	13X	0	0	100	25	30	4	0.5π	0.013632736	7.854	1.23E-05	9.96E+03
103	CO2	13X	100	100	0	0	30	40	0	0.011350479	0.7854	8.61E-06	1.42E+03
104	CO2N2	13X	0	0	100	50	30	4	1.5π	0.009483801	7.854	1.23E-05	9.96E+03
105	CO2N2	13X	0	0	100	50	30	10	1.5π	0.008431784	3.1416	1.23E-05	3.98E+03
106	CO2N2	13X	0	0	100	50	100	10	1.5π	0.007112851	3.1416	1.79E-05	2.74E+03
107	CO2N2	13X	0	0	100	50	30	4	0.5π	0.010134356	7.854	1.23E-05	9.96E+03
108	CO2N2	13X	0	0	100	50	30	10	0.5π	0.009242533	3.1416	1.23E-05	3.98E+03
109	CO2N2	13X	0	0	100	50	100	4	0.5π	0.007296736	7.854	1.79E-05	6.84E+03
110	CO2N2	13X	0	0	100	50	100	10	0.5π	0.006454253	3.1416	1.79E-05	2.74E+03
111	CO2N2_2080	13X	0	50	100	100	30	10	1.5π	0.016046696	3.1416	1.45E-05	3.38E+03
112	CO2N2_2080	13X	0	50	100	100	30	4	1.5π	0.009728982	7.854	1.45E-05	8.44E+03
113	CO2N2_2080	13X	0	50	100	100	30	10	0.5π	0.008107485	3.1416	1.45E-05	3.38E+03
114	CO2N2_2080	13X	0	50	100	100	30	4	0.5π	0.008918233	7.854	1.45E-05	8.44E+03
115	CO2N2_2080	13X	0	50	100	100	100	10	0.5π	0.006585973	3.1416	2.10E-05	2.34E+03
116	CO2N2_2080	13X	0	50	100	100	100	4	0.5π	0.009878959	7.854	2.10E-05	5.84E+03
117	CO2N2_2080	13X	0	50	100	100	100	10	1.5π	0.009878959	3.1416	2.10E-05	2.34E+03
118	CO2N2_2080	13X	0	50	100	100	100	4	1.5π	0.009295122	7.854	2.10E-05	5.84E+03
119	CO2N2	13X	0	0	100	12	30	4	1.5π	0.011350479	7.854	1.23E-05	9.96E+03
120	CO2N2	13X	0	0	100	6	30	4	1.5π	0.010470617	7.854	1.23E-05	9.96E+03
121	CO2N2	13X	0	0	100	23	30	4	1.5π	0.009665185	7.854	1.23E-05	9.96E+03
122	CO2	13X (2pellets)	0	0	100	100	30	4	1.5π	0.014204644	7.854	8.61E-06	1.42E+04
123	CO2	13X (2pellets)	0	0	100	100	30	10	1.5π	0.009665185	3.1416	8.61E-06	5.69E+03
124	CO2	13X (2pellets)	0	0	100	25	30	10	1.5π	0.009064162	3.1416	8.61E-06	5.69E+03
125	CO2	13X (2pellets)	0	0	100	100	30	10	0	0.008859753	3.1416	8.61E-06	5.69E+03
126	N2	13X (2pellets)	0	0	100	100	30	10	1.5π	0.011276049	3.1416	1.60E-05	3.06E+03

127	N2	13X (2pellets)	0	0	75	75	30	10	0	0.008054321	2.3562	1.60E-05	2.30E+03
128	N2	13X (2pellets)	0	0	100	100	30	4	1.5π	0.008859753	7.854	1.60E-05	7.66E+03
129	N2	13X (2pellets)	0	0	75	75	30	60	0	0.009665185	0.3927	1.60E-05	3.83E+02
130	N2	13X (2pellets)	0	0	75	75	30	30	0	0.009665185	0.7854	1.60E-05	7.66E+02
131	N2	13X (2pellets)	0	0	75	75	30	4	0	0.009665185	5.8905	1.60E-05	5.75E+03
132	N2	13X (2pellets)	0	0	40	40	30	60	0	0.009665185	0.20944	1.60E-05	2.04E+02
133	N2	13X (2pellets)	0	0	40	40	30	30	0	0.009665185	0.41888	1.60E-05	4.09E+02
134	N2	13X (2pellets)	0	0	40	40	30	10	0	0.009665185	1.25664	1.60E-05	1.23E+03
135	N2	13X (2pellets)	0	0	40	40	30	4	0	0.009665185	3.1416	1.60E-05	3.06E+03
136	N2	13X (2pellets)	0	0	10	10	30	60	0	0.009665185	0.05236	1.60E-05	5.11E+01
137	N2	13X (2pellets)	0	0	10	10	30	30	0	0.009665185	0.10472	1.60E-05	1.02E+02
138	N2	13X (2pellets)	0	0	10	10	30	10	0	0.009665185	0.31416	1.60E-05	3.06E+02
139	N2	13X (2pellets)	0	0	10	10	30	4	0	0.009665185	0.7854	1.60E-05	7.66E+02
140	N2	13X (2pellets)	0	0	75	75	30	2	0	0.009665185	11.781	1.60E-05	1.15E+04
141	N2	13X (2pellets)	0	0	40	40	30	2	0	0.009665185	6.2832	1.60E-05	6.13E+03
142	N2	13X (2pellets)	0	0	10	10	30	2	0	0.009665185	1.5708	1.60E-05	1.53E+03
143	N2	13X (2pellets)	0	0	75	75	100	60	0	0.008631184	0.3927	2.30E-05	2.66E+02
144	N2	13X (2pellets)	0	0	75	75	100	30	0	0.008631184	0.7854	2.30E-05	5.32E+02
145	N2	13X (2pellets)	0	0	75	75	100	4	0	0.008631184	5.8905	2.30E-05	3.99E+03
146	N2	13X (2pellets)	0	0	40	40	100	60	0	0.008631184	0.20944	2.30E-05	1.42E+02
147	N2	13X (2pellets)	0	0	40	40	100	30	0	0.008631184	0.41888	2.30E-05	2.84E+02
148	N2	13X (2pellets)	0	0	40	40	100	10	0	0.008631184	1.25664	2.30E-05	8.52E+02
149	N2	13X (2pellets)	0	0	40	40	100	4	0	0.008631184	3.1416	2.30E-05	2.13E+03
150	N2	13X (2pellets)	0	0	10	10	100	60	0	0.008631184	0.05236	2.30E-05	3.55E+01
151	N2	13X (2pellets)	0	0	10	10	100	30	0	0.008631184	0.10472	2.30E-05	7.10E+01
152	N2	13X	0	0	10	10	100	10	0	0.008631184	0.31416	2.30E-05	2.13E+02

		(2pellets)											
153	N2	13X (2pellets)	0	0	10	10	100	4	0	0.008631184	0.7854	2.30E-05	5.32E+02
154	N2	13X (2pellets)	0	0	75	75	100	2	0	0.008631184	11.781	2.30E-05	7.99E+03
155	N2	13X (2pellets)	0	0	40	40	100	2	0	0.008631184	6.2832	2.30E-05	4.26E+03
156	N2	13X (2pellets)	0	0	10	10	100	2	0	0.008631184	1.5708	2.30E-05	1.06E+03
157	N2	13X (2pellets)	0	0	75	75	100	10	0	0.008631184	2.3562	2.30E-05	1.60E+03
158	N2	13X (2pellets)	0	0	75	75	60	60	0	0.009959059	0.3927	1.89E-05	3.24E+02
159	N2	13X (2pellets)	0	0	75	75	60	30	0	0.009959059	0.7854	1.89E-05	6.49E+02
160	N2	13X (2pellets)	0	0	75	75	60	4	0	0.009959059	5.8905	1.89E-05	4.87E+03
161	N2	13X (2pellets)	0	0	40	40	60	60	0	0.009959059	0.20944	1.89E-05	1.73E+02
162	N2	13X (2pellets)	0	0	40	40	60	30	0	0.009959059	0.41888	1.89E-05	3.46E+02
163	N2	13X (2pellets)	0	0	40	40	60	10	0	0.009959059	1.25664	1.89E-05	1.04E+03
164	N2	13X (2pellets)	0	0	40	40	60	4	0	0.009959059	3.1416	1.89E-05	2.60E+03
165	N2	13X (2pellets)	0	0	10	10	60	60	0	0.009959059	0.05236	1.89E-05	4.33E+01
166	N2	13X (2pellets)	0	0	10	10	60	30	0	0.009959059	0.10472	1.89E-05	8.65E+01
167	N2	13X (2pellets)	0	0	10	10	60	10	0	0.009959059	0.31416	1.89E-05	2.60E+02
168	N2	13X (2pellets)	0	0	10	10	60	4	0	0.009959059	0.7854	1.89E-05	6.49E+02
169	N2	13X (2pellets)	0	0	75	75	60	2	0	0.009959059	11.781	1.89E-05	9.73E+03
170	N2	13X (2pellets)	0	0	40	40	60	2	0	0.009959059	6.2832	1.89E-05	5.19E+03
171	N2	13X (2pellets)	0	0	10	10	60	2	0	0.009959059	1.5708	1.89E-05	1.30E+03
172	N2	13X (2pellets)	0	0	75	75	60	10	0	0.009959059	2.3562	1.89E-05	1.95E+03
173	CO2	13X (2pellets)	0	0	10	10	30	60	0	0.012081481	0.05236	8.61E-06	9.49E+01
174	CO2	13X (2pellets)	0	0	40	40	30	60	0	0.012081481	0.20944	8.61E-06	3.80E+02
175	CO2	13X (2pellets)	0	0	75	75	30	60	0	0.012081481	0.3927	8.61E-06	7.12E+02
176	CO2	13X (2pellets)	0	0	10	10	30	30	0	0.012081481	0.10472	8.61E-06	1.90E+02
177	CO2	13X (2pellets)	0	0	40	40	30	30	0	0.012081481	0.41888	8.61E-06	7.59E+02

178	CO2	13X (2pellets)	0	0	75	75	30	30	0	0.012081481	0.7854	8.61E-06	1.42E+03
179	CO2	13X (2pellets)	0	0	10	10	30	10	0	0.012081481	0.31416	8.61E-06	5.69E+02
180	CO2	13X (2pellets)	0	0	40	40	30	10	0	0.012081481	1.25664	8.61E-06	2.28E+03
181	CO2	13X (2pellets)	0	0	75	75	30	10	0	0.012081481	2.3562	8.61E-06	4.27E+03
182	CO2	13X (2pellets)	0	0	10	10	30	4	0	0.012081481	0.7854	8.61E-06	1.42E+03
183	CO2	13X (2pellets)	0	0	40	40	30	4	0	0.012081481	3.1416	8.61E-06	5.69E+03
184	CO2	13X (2pellets)	0	0	75	75	30	4	0	0.012081481	5.8905	8.61E-06	1.07E+04
185	CO2	13X (2pellets)	0	0	10	10	30	2	0	0.012081481	1.5708	8.61E-06	2.85E+03
186	CO2	13X (2pellets)	0	0	40	40	30	2	0	0.012081481	6.2832	8.61E-06	1.14E+04
187	CO2	13X (2pellets)	0	0	75	75	30	2	0	0.012081481	11.781	8.61E-06	2.14E+04
188	CO2	13X (2pellets)	0	0	10	10	60	60	0	0.010390317	0.05236	1.03E-05	7.94E+01
189	CO2	13X (2pellets)	0	0	40	40	60	60	0	0.010390317	0.20944	1.03E-05	3.18E+02
190	CO2	13X (2pellets)	0	0	75	75	60	60	0	0.010390317	0.3927	1.03E-05	5.95E+02
191	CO2	13X (2pellets)	0	0	10	10	60	30	0	0.010390317	0.10472	1.03E-05	1.59E+02
192	CO2	13X (2pellets)	0	0	40	40	60	30	0	0.010390317	0.41888	1.03E-05	6.35E+02
193	CO2	13X (2pellets)	0	0	75	75	60	30	0	0.010390317	0.7854	1.03E-05	1.19E+03
194	CO2	13X (2pellets)	0	0	10	10	60	10	0	0.010390317	0.31416	1.03E-05	4.76E+02
195	CO2	13X (2pellets)	0	0	40	40	60	10	0	0.010390317	1.25664	1.03E-05	1.91E+03
196	CO2	13X (2pellets)	0	0	75	75	60	10	0	0.010390317	2.3562	1.03E-05	3.57E+03
197	CO2	13X (2pellets)	0	0	10	10	60	4	0	0.010390317	0.7854	1.03E-05	1.19E+03
198	CO2	13X (2pellets)	0	0	40	40	60	4	0	0.010390317	3.1416	1.03E-05	4.76E+03
199	CO2	13X (2pellets)	0	0	75	75	60	4	0	0.010390317	5.8905	1.03E-05	8.93E+03
200	CO2	13X (2pellets)	0	0	10	10	60	2	0	0.010390317	1.5708	1.03E-05	2.38E+03
201	CO2	13X (2pellets)	0	0	40	40	60	2	0	0.010390317	6.2832	1.03E-05	9.53E+03
202	CO2	13X (2pellets)	0	0	75	75	60	2	0	0.010390317	11.781	1.03E-05	1.79E+04
203	CO2	13X	0	0	10	10	100	60	0	0.009959059	0.05236	1.28E-05	6.38E+01

		(2pellets)											
204	CO2	13X (2pellets)	0	0	40	40	100	60	0	0.009959059	0.20944	1.28E-05	2.55E+02
205	CO2	13X (2pellets)	0	0	75	75	100	60	0	0.009959059	0.3927	1.28E-05	4.78E+02
206	CO2	13X (2pellets)	0	0	10	10	100	30	0	0.009959059	0.10472	1.28E-05	1.28E+02
207	CO2	13X (2pellets)	0	0	40	40	100	30	0	0.009959059	0.41888	1.28E-05	5.10E+02
208	CO2	13X (2pellets)	0	0	75	75	100	30	0	0.009959059	0.7854	1.28E-05	9.56E+02
209	CO2	13X (2pellets)	0	0	10	10	100	10	0	0.009959059	0.31416	1.28E-05	3.83E+02
210	CO2	13X (2pellets)	0	0	40	40	100	10	0	0.009959059	1.25664	1.28E-05	1.53E+03
211	CO2	13X (2pellets)	0	0	75	75	100	10	0	0.009959059	2.3562	1.28E-05	2.87E+03
212	CO2	13X (2pellets)	0	0	10	10	100	4	0	0.009959059	0.7854	1.28E-05	9.56E+02
213	CO2	13X (2pellets)	0	0	40	40	100	4	0	0.009959059	3.1416	1.28E-05	3.83E+03
214	CO2	13X (2pellets)	0	0	75	75	100	4	0	0.009959059	5.8905	1.28E-05	7.17E+03
215	CO2	13X (2pellets)	0	0	10	10	100	2	0	0.009959059	1.5708	1.28E-05	1.91E+03
216	CO2	13X (2pellets)	0	0	40	40	100	2	0	0.009959059	6.2832	1.28E-05	7.65E+03
217	CO2	13X (2pellets)	0	0	75	75	100	2	0	0.009959059	11.781	1.28E-05	1.43E+04
218	He	13X (2pellets)	0	0	10	10	30	60	0	0.011276049	0.05236	1.24E-04	6.58E+00
219	He	13X (2pellets)	0	0	40	40	30	60	0	0.011276049	0.20944	1.24E-04	2.63E+01
220	He	13X (2pellets)	0	0	75	75	30	60	0	0.011276049	0.3927	1.24E-04	4.93E+01
221	He	13X (2pellets)	0	0	10	10	30	30	0	0.011276049	0.10472	1.24E-04	1.32E+01
222	He	13X (2pellets)	0	0	40	40	30	30	0	0.011276049	0.41888	1.24E-04	5.26E+01
223	He	13X (2pellets)	0	0	75	75	30	30	0	0.011276049	0.7854	1.24E-04	9.86E+01
224	He	13X (2pellets)	0	0	10	10	30	10	0	0.011276049	0.31416	1.24E-04	3.95E+01
225	He	13X (2pellets)	0	0	40	40	30	10	0	0.011276049	1.25664	1.24E-04	1.58E+02
226	He	13X (2pellets)	0	0	75	75	30	10	0	0.011276049	2.3562	1.24E-04	2.96E+02
227	He	13X (2pellets)	0	0	10	10	30	4	0	0.011276049	0.7854	1.24E-04	9.86E+01
228	He	13X (2pellets)	0	0	40	40	30	4	0	0.011276049	3.1416	1.24E-04	3.95E+02

229	He	13X (2pellets)	0	0	75	75	30	4	0	0.011276049	5.8905	1.24E-04	7.40E+02
230	He	13X (2pellets)	0	0	10	10	30	2	0	0.011276049	1.5708	1.24E-04	1.97E+02
231	He	13X (2pellets)	0	0	40	40	30	2	0	0.011276049	6.2832	1.24E-04	7.89E+02
232	He	13X (2pellets)	0	0	75	75	30	2	0	0.011276049	11.781	1.24E-04	1.48E+03
233	He	13X (2pellets)	0	0	10	10	60	60	0	0.010327913	0.05236	1.46E-04	5.60E+00
234	He	13X (2pellets)	0	0	40	40	60	60	0	0.010327913	0.20944	1.46E-04	2.24E+01
235	He	13X (2pellets)	0	0	75	75	60	60	0	0.010327913	0.3927	1.46E-04	4.20E+01
236	He	13X (2pellets)	0	0	10	10	60	30	0	0.010327913	0.10472	1.46E-04	1.12E+01
237	He	13X (2pellets)	0	0	40	40	60	30	0	0.010327913	0.41888	1.46E-04	4.48E+01
238	He	13X (2pellets)	0	0	75	75	60	30	0	0.010327913	0.7854	1.46E-04	8.40E+01
239	He	13X (2pellets)	0	0	10	10	60	10	0	0.010327913	0.31416	1.46E-04	3.36E+01
240	He	13X (2pellets)	0	0	40	40	60	10	0	0.010327913	1.25664	1.46E-04	1.34E+02
241	He	13X (2pellets)	0	0	75	75	60	10	0	0.010327913	2.3562	1.46E-04	2.52E+02
242	He	13X (2pellets)	0	0	10	10	60	4	0	0.010327913	0.7854	1.46E-04	8.40E+01
243	He	13X (2pellets)	0	0	40	40	60	4	0	0.010327913	3.1416	1.46E-04	3.36E+02
244	He	13X (2pellets)	0	0	75	75	60	4	0	0.010327913	5.8905	1.46E-04	6.30E+02
245	He	13X (2pellets)	0	0	10	10	60	2	0	0.010327913	1.5708	1.46E-04	1.68E+02
246	He	13X (2pellets)	0	0	40	40	60	2	0	0.010327913	6.2832	1.46E-04	6.72E+02
247	He	13X (2pellets)	0	0	75	75	60	2	0	0.010327913	11.781	1.46E-04	1.26E+03
248	He	13X (2pellets)	0	0	10	10	100	60	0	0.010622996	0.05236	1.77E-04	4.62E+00
249	He	13X (2pellets)	0	0	40	40	100	60	0	0.010622996	0.20944	1.77E-04	1.85E+01
250	He	13X (2pellets)	0	0	75	75	100	60	0	0.010622996	0.3927	1.77E-04	3.47E+01
251	He	13X (2pellets)	0	0	10	10	100	30	0	0.010622996	0.10472	1.77E-04	9.24E+00
252	He	13X (2pellets)	0	0	40	40	100	30	0	0.010622996	0.41888	1.77E-04	3.70E+01
253	He	13X (2pellets)	0	0	75	75	100	30	0	0.010622996	0.7854	1.77E-04	6.93E+01
254	He	13X	0	0	10	10	100	10	0	0.010622996	0.31416	1.77E-04	2.77E+01

		(2pellets)											
255	He	13X (2pellets)	0	0	40	40	100	10	0	0.010622996	1.25664	1.77E-04	1.11E+02
256	He	13X (2pellets)	0	0	75	75	100	10	0	0.010622996	2.3562	1.77E-04	2.08E+02
257	He	13X (2pellets)	0	0	10	10	100	4	0	0.010622996	0.7854	1.77E-04	6.93E+01
258	He	13X (2pellets)	0	0	40	40	100	4	0	0.009295122	3.1416	1.77E-04	2.77E+02
259	He	13X (2pellets)	0	0	75	75	100	4	0	0.009295122	5.8905	1.77E-04	5.20E+02
260	He	13X (2pellets)	0	0	10	10	100	2	0	0.009295122	1.5708	1.77E-04	1.39E+02
261	He	13X (2pellets)	0	0	40	40	100	2	0	0.009295122	6.2832	1.77E-04	5.54E+02
262	He	13X (2pellets)	0	0	75	75	100	2	0	0.009295122	11.781	1.77E-04	1.04E+03
263	CO2	13X (2pellets)	0	0	10	10	30	60	0	0.009826271	0.05236	8.61E-06	9.49E+01
264	CO2	13X (2pellets)	0	0	40	40	30	60	0	0.009826271	0.20944	8.61E-06	3.80E+02
265	CO2	13X (2pellets)	0	0	75	75	30	60	0	0.009826271	0.3927	8.61E-06	7.12E+02
266	CO2	13X (2pellets)	0	0	10	10	30	30	0	0.009826271	0.10472	8.61E-06	1.90E+02
267	CO2	13X (2pellets)	0	0	40	40	30	30	0	0.009826271	0.41888	8.61E-06	7.59E+02
268	CO2	13X (2pellets)	0	0	75	75	30	30	0	0.009826271	0.7854	8.61E-06	1.42E+03
269	CO2	13X (2pellets)	0	0	10	10	30	10	0	0.009826271	0.31416	8.61E-06	5.69E+02
270	CO2	13X (2pellets)	0	0	40	40	30	10	0	0.009826271	1.25664	8.61E-06	2.28E+03
271	CO2	13X (2pellets)	0	0	75	75	30	10	0	0.009826271	2.3562	8.61E-06	4.27E+03
272	CO2	13X (2pellets)	0	0	10	10	30	4	0	0.009826271	0.7854	8.61E-06	1.42E+03
273	CO2	13X (2pellets)	0	0	40	40	30	4	0	0.008932974	3.1416	8.61E-06	5.69E+03
274	CO2	13X (2pellets)	0	0	75	75	30	4	0	0.008932974	5.8905	8.61E-06	1.07E+04
275	CO2	13X (2pellets)	0	0	10	10	30	2	0	0.008932974	1.5708	8.61E-06	2.85E+03
276	CO2	13X (2pellets)	0	0	40	40	30	2	0	0.008932974	6.2832	8.61E-06	1.14E+04
277	CO2	13X (2pellets)	0	0	75	75	30	2	0	0.008932974	11.781	8.61E-06	2.14E+04
278	CO2	13X (2pellets)	0	0	10	10	100	60	0	0.008932974	0.05236	1.28E-05	6.38E+01
279	CO2	13X (2pellets)	0	0	40	40	100	60	0	0.008932974	0.20944	1.28E-05	2.55E+02

280	CO2	13X (2pellets)	0	0	75	75	100	60	0	0.008932974	0.3927	1.28E-05	4.78E+02
281	CO2	13X (2pellets)	0	0	10	10	100	30	0	0.008932974	0.10472	1.28E-05	1.28E+02
282	CO2	13X (2pellets)	0	0	40	40	100	30	0	0.008932974	0.41888	1.28E-05	5.10E+02
283	CO2	13X (2pellets)	0	0	75	75	100	30	0	0.008932974	0.7854	1.28E-05	9.56E+02
284	CO2	13X (2pellets)	0	0	10	10	100	10	0	0.008932974	0.31416	1.28E-05	3.83E+02
285	CO2	13X (2pellets)	0	0	40	40	100	10	0	0.008932974	1.25664	1.28E-05	1.53E+03
286	CO2	13X (2pellets)	0	0	75	75	100	10	0	0.008932974	2.3562	1.28E-05	2.87E+03
287	CO2	13X (2pellets)	0	0	10	10	100	4	0	0.008932974	0.7854	1.28E-05	9.56E+02
288	CO2	13X (2pellets)	0	0	40	40	100	4	0	0.008932974	3.1416	1.28E-05	3.83E+03
289	CO2	13X (2pellets)	0	0	75	75	100	4	0	0.008932974	5.8905	1.28E-05	7.17E+03
290	CO2	13X (2pellets)	0	0	10	10	100	2	0	0.008932974	1.5708	1.28E-05	1.91E+03
291	CO2	13X (2pellets)	0	0	40	40	100	2	0	0.007967247	6.2832	1.28E-05	7.65E+03
292	CO2	13X (2pellets)	0	0	75	75	100	2	0	0.007967247	11.781	1.28E-05	1.43E+04
293	He	13X (2pellets)	0	0	10	10	30	60	0	0.008859753	0.05236	1.24E-04	6.58E+00
294	He	13X (2pellets)	0	0	40	40	30	60	0	0.008859753	0.20944	1.24E-04	2.63E+01
295	He	13X (2pellets)	0	0	75	75	30	60	0	0.008859753	0.3927	1.24E-04	4.93E+01
296	He	13X (2pellets)	0	0	10	10	30	30	0	0.008859753	0.10472	1.24E-04	1.32E+01
297	He	13X (2pellets)	0	0	40	40	30	30	0	0.008859753	0.41888	1.24E-04	5.26E+01
298	He	13X (2pellets)	0	0	75	75	30	30	0	0.008859753	0.7854	1.24E-04	9.86E+01
299	He	13X (2pellets)	0	0	10	10	30	10	0	0.008859753	0.31416	1.24E-04	3.95E+01
300	He	13X (2pellets)	0	0	40	40	30	10	0	0.008859753	1.25664	1.24E-04	1.58E+02
301	He	13X (2pellets)	0	0	75	75	30	10	0	0.008859753	2.3562	1.24E-04	2.96E+02
302	He	13X (2pellets)	0	0	10	10	30	4	0	0.008859753	0.7854	1.24E-04	9.86E+01
303	He	13X (2pellets)	0	0	40	40	30	4	0	0.008859753	3.1416	1.24E-04	3.95E+02
304	He	13X (2pellets)	0	0	75	75	30	4	0	0.008859753	5.8905	1.24E-04	7.40E+02
305	He	13X	0	0	10	10	30	2	0	0.008859753	1.5708	1.24E-04	1.97E+02

		(2pellets)											
306	He	13X (2pellets)	0	0	40	40	30	2	0	0.008859753	6.2832	1.24E-04	7.89E+02
307	He	13X (2pellets)	0	0	75	75	30	2	0	0.008859753	11.781	1.24E-04	1.48E+03
308	He	13X (2pellets)	0	0	10	10	100	60	0	0.007967247	0.05236	1.77E-04	4.62E+00
309	He	13X (2pellets)	0	0	40	40	100	60	0	0.007967247	0.20944	1.77E-04	1.85E+01
310	He	13X (2pellets)	0	0	75	75	100	60	0	0.007967247	0.3927	1.77E-04	3.47E+01
311	He	13X (2pellets)	0	0	10	10	100	30	0	0.007967247	0.10472	1.77E-04	9.24E+00
312	He	13X (2pellets)	0	0	40	40	100	30	0	0.007967247	0.41888	1.77E-04	3.70E+01
313	He	13X (2pellets)	0	0	75	75	100	30	0	0.007967247	0.7854	1.77E-04	6.93E+01
314	He	13X (2pellets)	0	0	10	10	100	10	0	0.007967247	0.31416	1.77E-04	2.77E+01
315	He	13X (2pellets)	0	0	40	40	100	10	0	0.007967247	1.25664	1.77E-04	1.11E+02
316	He	13X (2pellets)	0	0	75	75	100	10	0	0.007967247	2.3562	1.77E-04	2.08E+02
317	He	13X (2pellets)	0	0	10	10	100	4	0	0.007967247	0.7854	1.77E-04	6.93E+01
318	He	13X (2pellets)	0	0	40	40	100	4	0	0.007967247	3.1416	1.77E-04	2.77E+02
319	He	13X (2pellets)	0	0	75	75	100	4	0	0.007967247	5.8905	1.77E-04	5.20E+02
320	He	13X (2pellets)	0	0	10	10	100	2	0	0.007967247	1.5708	1.77E-04	1.39E+02
321	He	13X (2pellets)	0	0	40	40	100	2	0	0.007967247	6.2832	1.77E-04	5.54E+02
322	He	13X (2pellets)	0	0	75	75	100	2	0	0.007967247	11.781	1.77E-04	1.04E+03
323	N2	13X (2pellets)	0	0	10	10	30	60	0	0.008054321	0.05236	1.60E-05	5.11E+01
324	N2	13X (2pellets)	0	0	40	40	30	60	0	0.008054321	0.20944	1.60E-05	2.04E+02
325	N2	13X (2pellets)	0	0	75	75	30	60	0	0.008054321	0.3927	1.60E-05	3.83E+02
326	N2	13X (2pellets)	0	0	10	10	30	30	0	0.008054321	0.10472	1.60E-05	1.02E+02
327	N2	13X (2pellets)	0	0	40	40	30	30	0	0.008054321	0.41888	1.60E-05	4.09E+02
328	N2	13X (2pellets)	0	0	75	75	30	30	0	0.008054321	0.7854	1.60E-05	7.66E+02
329	N2	13X (2pellets)	0	0	10	10	30	10	0	0.008054321	0.31416	1.60E-05	3.06E+02
330	N2	13X (2pellets)	0	0	40	40	30	10	0	0.008054321	1.25664	1.60E-05	1.23E+03

331	N2	13X (2pellets)	0	0	75	75	30	10	0	0.008054321	2.3562	1.60E-05	2.30E+03
332	N2	13X (2pellets)	0	0	10	10	30	4	0	0.008054321	0.7854	1.60E-05	7.66E+02
333	N2	13X (2pellets)	0	0	40	40	30	4	0	0.008054321	3.1416	1.60E-05	3.06E+03
334	N2	13X (2pellets)	0	0	75	75	30	4	0	0.008054321	5.8905	1.60E-05	5.75E+03
335	N2	13X (2pellets)	0	0	10	10	30	2	0	0.008054321	1.5708	1.60E-05	1.53E+03
336	N2	13X (2pellets)	0	0	40	40	30	2	0	0.008859753	6.2832	1.60E-05	6.13E+03
337	N2	13X (2pellets)	0	0	75	75	30	2	0	0.008859753	11.781	1.60E-05	1.15E+04
338	N2	13X (2pellets)	0	0	75	75	100	60	0	0.00730331	0.3927	2.30E-05	2.66E+02
339	N2	13X (2pellets)	0	0	75	75	100	30	0	0.00730331	0.7854	2.30E-05	5.32E+02
340	N2	13X (2pellets)	0	0	75	75	100	4	0	0.00730331	5.8905	2.30E-05	3.99E+03
341	N2	13X (2pellets)	0	0	40	40	100	60	0	0.00730331	0.20944	2.30E-05	1.42E+02
342	N2	13X (2pellets)	0	0	40	40	100	30	0	0.00730331	0.41888	2.30E-05	2.84E+02
343	N2	13X (2pellets)	0	0	40	40	100	10	0	0.00730331	1.25664	2.30E-05	8.52E+02
344	N2	13X (2pellets)	0	0	40	40	100	4	0	0.00730331	3.1416	2.30E-05	2.13E+03
345	N2	13X (2pellets)	0	0	10	10	100	60	0	0.00730331	0.05236	2.30E-05	3.55E+01
346	N2	13X (2pellets)	0	0	10	10	100	30	0	0.00730331	0.10472	2.30E-05	7.10E+01
347	N2	13X (2pellets)	0	0	10	10	100	10	0	0.00730331	0.31416	2.30E-05	2.13E+02
348	N2	13X (2pellets)	0	0	10	10	100	4	0	0.00730331	0.7854	2.30E-05	5.32E+02
349	N2	13X (2pellets)	0	0	75	75	100	2	0	0.00730331	11.781	2.30E-05	7.99E+03
350	N2	13X (2pellets)	0	0	40	40	100	2	0	0.00730331	6.2832	2.30E-05	4.26E+03
351	N2	13X (2pellets)	0	0	10	10	100	2	0	0.00730331	1.5708	2.30E-05	1.06E+03
352	N2	13X (2pellets)	0	0	75	75	100	10	0	0.00730331	2.3562	2.30E-05	1.60E+03
353	CO2N2	13X (2pellets)	0	0	75	75	100	60	0	0.00730331	0.3927	1.79E-05	3.42E+02
354	CO2N2	13X (2pellets)	0	0	75	75	100	30	0	0.00730331	0.7854	1.79E-05	6.84E+02
355	CO2N2	13X (2pellets)	0	0	75	75	100	4	0	0.00730331	5.8905	1.79E-05	5.13E+03
356	CO2N2	13X	0	0	40	40	100	60	0	0.00730331	0.20944	1.79E-05	1.82E+02

		(2pellets)											
357	CO2N2	13X (2pellets)	0	0	40	40	100	30	0	0.00730331	0.41888	1.79E-05	3.65E+02
358	CO2N2	13X (2pellets)	0	0	40	40	100	10	0	0.00730331	1.25664	1.79E-05	1.09E+03
359	CO2N2	13X (2pellets)	0	0	40	40	100	4	0	0.00730331	3.1416	1.79E-05	2.74E+03
360	CO2N2	13X (2pellets)	0	0	10	10	100	60	0	0.00730331	0.05236	1.79E-05	4.56E+01
361	CO2N2	13X (2pellets)	0	0	10	10	100	30	0	0.00730331	0.10472	1.79E-05	9.12E+01
362	CO2N2	13X (2pellets)	0	0	10	10	100	10	0	0.00730331	0.31416	1.79E-05	2.74E+02
363	CO2N2	13X (2pellets)	0	0	10	10	100	4	0	0.00730331	0.7854	1.79E-05	6.84E+02
364	CO2N2	13X (2pellets)	0	0	75	75	100	2	0	0.00730331	11.781	1.79E-05	1.03E+04
365	CO2N2	13X (2pellets)	0	0	40	40	100	2	0	0.00730331	6.2832	1.79E-05	5.47E+03
366	CO2N2	13X (2pellets)	0	0	10	10	100	2	0	0.00730331	1.5708	1.79E-05	1.37E+03
367	CO2N2	13X (2pellets)	0	0	75	75	100	10	0	0.00730331	2.3562	1.79E-05	2.05E+03
368	CO2N2	13X (2pellets)	0	0	75	75	30	60	0	0.008859753	0.3927	1.23E-05	4.98E+02
369	CO2N2	13X (2pellets)	0	0	75	75	30	30	0	0.008859753	0.7854	1.23E-05	9.96E+02
370	CO2N2	13X (2pellets)	0	0	75	75	30	4	0	0.008859753	5.8905	1.23E-05	7.47E+03
371	CO2N2	13X (2pellets)	0	0	40	40	30	60	0	0.008859753	0.20944	1.23E-05	2.66E+02
372	CO2N2	13X (2pellets)	0	0	40	40	30	30	0	0.008859753	0.41888	1.23E-05	5.31E+02
373	CO2N2	13X (2pellets)	0	0	40	40	30	10	0	0.008859753	1.25664	1.23E-05	1.59E+03
374	CO2N2	13X (2pellets)	0	0	40	40	30	4	0	0.008859753	3.1416	1.23E-05	3.98E+03
375	CO2N2	13X (2pellets)	0	0	10	10	30	60	0	0.008859753	0.05236	1.23E-05	6.64E+01
376	CO2N2	13X (2pellets)	0	0	10	10	30	30	0	0.008859753	0.10472	1.23E-05	1.33E+02
377	CO2N2	13X (2pellets)	0	0	10	10	30	10	0	0.008859753	0.31416	1.23E-05	3.98E+02
378	CO2N2	13X (2pellets)	0	0	10	10	30	4	0	0.008859753	0.7854	1.23E-05	9.96E+02
379	CO2N2	13X (2pellets)	0	0	75	75	30	2	0	0.008859753	11.781	1.23E-05	1.49E+04
380	CO2N2	13X (2pellets)	0	0	40	40	30	2	0	0.008859753	6.2832	1.23E-05	7.97E+03
381	CO2N2	13X (2pellets)	0	0	10	10	30	2	0	0.008859753	1.5708	1.23E-05	1.99E+03

382	CO2N2	13X (2pellets)	0	0	75	75	30	10	0	0.008859753	2.3562	1.23E-05	2.99E+03
383	CO2	13X (2pellets)	0	0	40	40	30	60	0	0.008859753	0.20944	8.61E-06	3.80E+02
384	CO2	13X (2pellets)	0	0	75	75	30	60	0	0.008859753	0.3927	8.61E-06	7.12E+02
385	CO2	13X (2pellets)	0	0	10	10	30	30	0	0.008859753	0.10472	8.61E-06	1.90E+02
386	CO2	13X (2pellets)	0	0	40	40	30	30	0	0.008859753	0.41888	8.61E-06	7.59E+02
387	CO2	13X (2pellets)	0	0	75	75	30	30	0	0.008859753	0.7854	8.61E-06	1.42E+03
388	CO2	13X (2pellets)	0	0	10	10	30	10	0	0.008859753	0.31416	8.61E-06	5.69E+02
389	CO2	13X (2pellets)	0	0	40	40	30	10	0	0.008859753	1.25664	8.61E-06	2.28E+03
390	CO2	13X (2pellets)	0	0	75	75	30	10	0	0.008859753	2.3562	8.61E-06	4.27E+03
391	CO2	13X (2pellets)	0	0	10	10	30	4	0	0.008859753	0.7854	8.61E-06	1.42E+03
392	CO2	13X (2pellets)	0	0	40	40	30	4	0	0.008859753	3.1416	8.61E-06	5.69E+03
393	CO2	13X (2pellets)	0	0	75	75	30	4	0	0.008859753	5.8905	8.61E-06	1.07E+04
394	CO2	13X (2pellets)	0	0	10	10	30	2	0	0.008859753	1.5708	8.61E-06	2.85E+03
395	CO2	13X (2pellets)	0	0	40	40	30	2	0	0.008859753	6.2832	8.61E-06	1.14E+04
396	CO2	13X (2pellets)	0	0	75	75	30	2	0	0.008859753	11.781	8.61E-06	2.14E+04
397	CO2	13X (2pellets)	0	0	75	75	30	60	0.5π	0.010470617	0.3927	8.61E-06	7.12E+02
398	CO2	13X (2pellets)	0	0	75	75	30	60	1.5π	0.010470617	0.3927	8.61E-06	7.12E+02
399	CO2	13X (2pellets)	0	0	75	75	30	4	0.5π	0.010470617	5.8905	8.61E-06	1.07E+04
400	CO2	13X (2pellets)	0	0	75	75	30	4	1.5π	0.010470617	5.8905	8.61E-06	1.07E+04
401	He	13X (2pellets)	0	0	75	75	30	60	0.5π	0.009665185	0.3927	1.24E-04	4.93E+01
402	He	13X (2pellets)	0	0	75	75	30	60	1.5π	0.009665185	0.3927	1.24E-04	4.93E+01
403	He	13X (2pellets)	0	0	75	75	30	4	0.5π	0.008859753	5.8905	1.24E-04	7.40E+02
404	He	13X (2pellets)	0	0	75	75	30	4	1.5π	0.008859753	5.8905	1.24E-04	7.40E+02
405	He	13X (2pellets)	0	0	75	75	30	4	0	0.008859753	5.8905	1.24E-04	7.40E+02
406	CO2	13X (2pellets)	0	0	75	75	30	4	0	0.008859753	5.8905	8.61E-06	1.07E+04
407	CO2	13X	0	0	75	75	30	4	0	0.008859753	5.8905	8.61E-06	1.07E+04

		(2pellets)											

Appendix Ⅳ Temperature swing amplitudes in the Single Pellet experiment

Table 1 The temperature swing amplitudes in the helium experiments. Note: in the helium experiment of T=100˚C, the pellet at position 1 dropped. Thus T2 shows the gas temperature.

GAS	T_0 (˚C)	T_c (s)	SL (mm)	Amplitude T1 (˚C)	Amplitude T2 (˚C)	Amplitude T3 (˚C)	Amplitude T4 (˚C)
Helium	30	60	10	0.1	0.09	0.09	0.1
			40	0.13	0.11	0.2	0.18
			75	0.37	0.31	0.64	0.57
		30	10	0.11	0.1	0.1	0.1
			40	0.2	0.23	0.34	0.22
			75	0.65	0.63	1.12	0.84
		10	10	0.11	0.1	0.16	0.12
			40	0.35	0.23	0.61	0.28
			75	1.24	0.7	2.01	0.84
		4	10	0.14	0.11	0.16	0.14
			40	0.45	0.24	0.77	0.29
			75	1.47	0.71	2.49	0.85
	100	60	10	0.08	0.08	0.14	0.14
			40	0.08	0.08	0.15	0.13
			75	0.31	0.3	0.55	0.42
		30	10	0.04	0.04	0.06	0.06
			40	0.15	0.12	0.26	0.17
			75	0.58	0.64	0.77	0.46
		10	10	0.08	0.1	0.1	0.05
			40	0.38	0.42	0.49	0.11
			75	1.36	1.6	1.73	0.37
		4	10	0.11	0.11	0.11	0.06
			40	0.98	1.04	1.28	0.09
			75	1.79	2.15	2.26	0.17

Table 2 The temperature swing amplitudes in the N_2 experiments. Note: the pellet at position 1 dropped. T2 is reading a gas temperature.

GAS	T (˚C)	T_c (s)	SL (mm)	Amplitude T1 (˚C)	Amplitude T2 (˚C)	Amplitude T3 (˚C)	Amplitude T4 (˚C)
N_2	30	60	10	0.06	0.07	0.09	0.07
			40	0.28	0.32	0.38	0.33
			75	1.14	1.35	1.58	1.10
		30	10	0.08	0.1	0.11	0.06
			40	0.43	0.53	0.59	0.34
			75	1.64	1.97	2.08	1.05
		10	10	0.13	0.15	0.15	0.09
			40	0.62	0.75	0.77	0.34
			75	2.19	2.59	2.21	1.03
		4	10	0.16	0.18	0.18	0.05
			40	0.82	0.99	0.85	0.28
			75	2.5	3.2	2.24	0.76
	100	60	10	0.06	0.07	0.08	0.08
			40	0.24	0.29	0.34	0.24
			75	0.94	1.13	1.32	0.72
		30	10	0.08	0.1	0.11	0.09
			40	0.36	0.44	0.49	0.23
			75	1.4	1.66	1.84	0.7
		10	10	0.1	0.13	0.13	0.08
			40	0.53	0.64	0.66	0.18
			75	1.89	2.29	2.03	0.6
		4	10	0.15	0.2	0.16	0.08
			40	0.66	0.81	0.75	0.12
			75	2.26	2.77	2.01	0.39

Table 3 The temperature swing amplitudes in the CO2 experiments.

GAS	T (˚C)	T_c (s)	SL (mm)	Amplitude T1 (˚C)	Amplitude T2 (˚C)	Amplitude T3 (˚C)	Amplitude T4 (˚C)
CO_2	30	60	10	0.15	0.52	0.21	0.73
			40	0.52	2.3	0.7	3.12
			75	1.28	5.79	1.94	7.7
		30	10	0.15	0.43	0.19	0.64
			40	0.44	1.97	0.61	2.85
			75	1.15	5.01	1.78	7.22
		10	10	0.14	0.34	0.15	0.35
			40	0.44	1.35	0.65	1.64
			75	1.39	3.55	1.69	4.48
		4	10	0.14	0.29	0.23	0.28
			40	0.47	1.07	0.59	0.61
			75	1.44	2.78	1.48	1.69
	100	60	10	0.2	0.56	0.23	0.73
			40	0.51	2.44	0.77	3.35
			75	1.5	6.65	2.19	8.93
		30	10	0.06	0.35	0.11	0.55
			40	0.39	1.88	0.66	2.8
			75	1.22	5.29	1.98	7.76
		10	10	0.09	0.25	0.15	0.28
			40	0.46	1.3	0.7	1.53
			75	1.53	3.77	1.88	4.49
		4	10	0.11	0.2	0.19	0.22
			40	0.55	0.9	0.71	1.15
			75	1.72	2.45	1.78	2.59

Table 4 The temperature swing amplitudes in the mixture gas experiments. Note: the pellet at position 1 dropped. T2 is reading a gas temperature.

GAS	T (˚C)	T_c (s)	SL (mm)	Amplitude T1 (˚C)	Amplitude T2 (˚C)	Amplitude T3 (˚C)	Amplitude T4 (˚C)
CO2+N2	30	60	10	0.05	0.06	0.09	0.33
			40	0.24	0.29	0.49	1.93
			75	0.9	1.07	1.3	4.25
		30	10	0.06	0.08	0.08	0.29
			40	0.35	0.41	0.48	1.4
			75	1.28	1.52	1.44	3.75
		10	10	0.1	0.11	0.11	0.16
			40	0.47	0.56	0.55	0.63
			75	1.68	1.99	1.59	1.72
		4	10	0.11	0.12	0.14	0.07
			40	0.57	0.66	0.62	0.24
			75	1.56	2.15	1.36	0.56
	100	60	10	0.12	0.14	0.2	0.46
			40	0.28	0.34	0.57	2.1
			75	1.01	1.2	1.56	5.87
		30	10	0.08	0.09	0.1	0.33
			40	0.39	0.46	0.54	1.6
			75	1.45	1.72	1.69	4.59
		10	10	0.12	0.12	0.14	0.16
			40	0.54	0.63	0.66	0.74
			75	1.82	2.18	1.81	2.14
		4	10	0.14	0.15	0.13	0.06
			40	0.65	0.77	0.69	0.21
			75	2.1	2.52	1.62	0.57

Appendix Ⅳ Publications and presentations

Dang W., Friedrich D. and Brandani S. Chracterisation of an automated Dual Piston Pressure Swing Adsorption (DP-PSA) system. Energy Procedia, 1(1), 527-534. Elsevier. doi:10.1016. (2012)

Dang W., Friedrich D., Ferrari M.C. and Brandani S. Total Reflux Dual Piston-PSA: a Novel Apparatus for Testing Adsorbent Materials. 2010 AIChE Annual Meeting, Salt Lake City, UT, USA, 7-12 Nov. (2010)

Dang W., Friedrich D., Ferrari M.C. and Brandani S. Development and automation of a novel apparatus: Total Reflux Dual Piston-PSA. 2012 AIChE Annual Meeting, Pittsburgh,PA, USA, 28Oct-2 Nov. (2012)

Dang W., Friedrich D. and Brandani S. Single Pellet DP-PSA Experiments for the Characterisation of Heat and Mass Transfer Parameters. 2013 11th International Conference on the Fundamentals of Adsorption, Baltimore, MD, USA, 19-24 May. (2013)